Doctoral Program in Neuroscience

Curriculum in Neuroscience and Neurotechnology

XXXVI cycle

Lighting-up neurons: characterization of new membrane-targeted photoswitches for geneless neural stimulation

AUTHOR: MARLENE E. PFEFFER

SUPERVISOR: FABIO BENFENATI

TUTOR: MATTIA L. DIFRANCESCO

Summary

In the last decades, light-sensitive nanotools have emerged as a powerful approach for modulating neural circuits' activity with exquisite precision. Among the light-sensitive approaches, membrane-targeted photoswitches hold particular promise in enabling light-induced control of neuronal activity without directly interfering with physiological mechanisms and avoiding genetic manipulation. This doctoral thesis aims to unravel the intricate dynamics driven by light in the context of four distinct newly-synthetized membrane-targeted photochromic molecules. The foundation of this research lies in the characterization of Ziapin2, a newly synthetized photoswitch that demonstrated remarkable success in inducing firing activity in response to light, both *in vitro* and *in vivo*. Ziapin2 showed a distinct affinity for lipid rafts, membrane domains characterized by high concentrations of diverse proteins, including ion channels and receptors. Building upon this knowledge, our investigation focused on the light-dependent modulation of synaptic neurotransmission in primary neurons mediated by Ziapin2, recognizing the pivotal role of lipid rafts in neurotransmitter release. This exploration involved distinguishing between excitatory and inhibitory neuronal subpopulations, considering their inherent physiological differences in protein expression and synaptic machinery. The results revealed an opposite modulation pattern in light-triggered modulation of synaptic transmission, providing insights on its potential applications in controlling neural networks.

Moreover, we conducted a comprehensive characterization of 2Pyr-2Pyr, a photoswitch closely related to Ziapin2 but featuring a structural distinction that could potentially enhance its functionality. Our findings indicate that 2Pyr-2Pyr shares similar properties in modulating neuronal activity, offering the prospect of exploiting its structural difference for further engineering. Specifically, it could enable prolonged cellular membrane permanence, addressing a crucial challenge faced by Ziapin2, which is internalization through membrane recycling mechanisms over time.

In addition, this thesis studies newly synthetized Push-Pull molecules, employing a distinct donor-acceptor mechanism for membrane voltage modulation, unlike Ziapin2's capacitance modulation. The characterization of these molecules not only offered insights into alternative strategies for light-induced neuronal stimulation but also enhanced our understanding of the essential patterns of membrane voltage modulation required to initiate light-dependent firing activity.

Lastly, we present BV-1, a donor-acceptor photoswitch without the azobenzene core, in contrast to the previously studied photoswitches. BV-1 not only demonstrated efficient membrane voltage modulation

but also exhibited the unique ability to induce light-triggered membrane poration, expanding the potential repertoire of light-sensitive tools for neuroscience research.

In conclusion, this Ph.D. thesis characterizes four membrane-targeted photoswitches with a focus on their potential applications in modulating membrane voltage, neuronal activity, and cell viability, while exploring the underlying mechanisms. The findings highlight the diverse functional properties of these photoswitches and their potential applications in neuroscience. This research contributes to the growing body of knowledge in the field of optostimulation and paves the way for the development of more efficient and precise tools for neuroscience experimentation.

Contents

1 Introduction

1.1 Light as a tool

In recent decades, light has emerged as a powerful tool in neuroscience research, providing unprecedented spatiotemporal resolution, non-invasiveness, and versatility. This focus has given rise to a proliferation of innovative approaches that take advantage of the unique properties of light, making neurons directly or indirectly light-sensitive. The diverse applications of light can be categorized based on its wavelength into three distinct regions, each offering specific advantages for interacting with biological systems.

Ultraviolet (UV) light, spanning 10 nm to 400 nm, provides high spatial resolution, making it ideal for precise stimulation. However, its use demands careful handling due to the potential to damage biological tissues, including DNA. Visible light, ranging from 400 nm to 700 nm, presents itself in various colors depending on the specific wavelength. It seamlessly integrates with biological samples, allowing targeted effects without disrupting physiological processes. Finally, Near-Infrared (NIR) light, spanning 700 nm to 2500 nm, though invisible to the human eye, penetrates tissues deeply, enabling non-invasive stimulation of deeper brain regions. This categorization sets the stage for exploring the various ways in which light, with its distinct properties, has become an indispensable tool for neuronal stimulation.

1.2 Mechanisms of optostimulation

Neurons, encased within a lipid bilayer, function as dynamic entities, maintaining a stable resting membrane potential of approximately -70 mV via the selective permeation of ions and molecules facilitated by ion pumps and channels present on the cell membrane (Gadsby, 2009; Nicolson, 2014). This precisely regulated interplay undergoes physiological modulation, resulting in transient hyperpolarization and depolarization—fundamental elements of neuronal excitability. Notably, a robust depolarization event can trigger an action potential, ultimately enabling neuronal signaling.

Neurons exhibit resistance to most light stimulation, excluding specialized photoreceptors in the retina. This characteristic resistance positions light as a valuable stimulus, particularly when introduced through photosensitive nanotools. These tools facilitate the transduction of light into neurotransmission, opening innovative avenues in neuroscience.

Various strategies have emerged to confer light sensitivity to neurons. These strategies include the modulation of membrane permeability, the utilization of thermally mediated effects for the alteration of cell membrane parameters, the implementation of capacitive coupling involving electronic charges on the surface of an active material, and the manipulation of electrical current flow through the lipid bilayer (Figure 1). These ingenious methodologies collectively serve to modulate membrane potential, presenting a nuanced approach for influencing neuronal excitability in response to light stimuli (Yang et al., 2021).

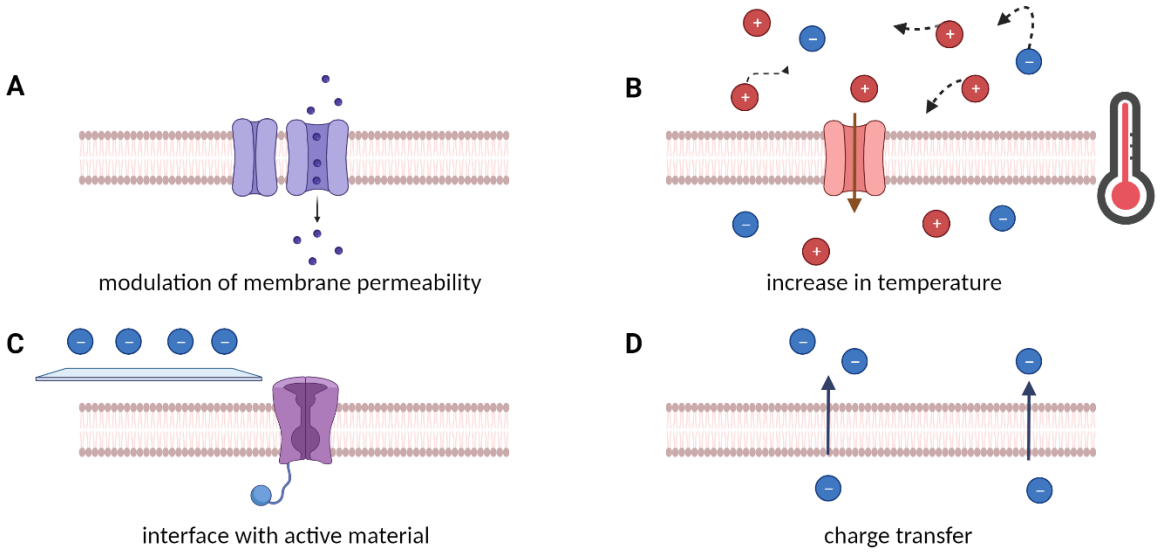

Figure 1 Strategies to trigger membrane depolarization using light
A. Fine-tune of the ion permeability of the cell membrane by incorporating exogenous light-sensitive channels. **B.** Inducing a localized increase in temperature, amplifying molecular motion and ion channel activity. This heightened thermal energy facilitates enhanced ionic flux, contributing to the promotion of neuronal firing. **C.** Interface with actively light-sensitive materials capable of electron charge accumulation, enabling external modulation of the membrane potential. **D.** Initiating a light-triggered charge transfer through the lipid bilayer using light-sensitive molecules leads to the redistribution of electron charges within the cell membrane, resulting in alterations in the membrane potential.

Figure created with Biorender.com

Furthermore, the application of light-driven nanotechnology extends beyond neurotransmission modulation, finding utility in inducing precise and minimally invasive membrane poration. This breakthrough opens possibilities for a spectrum of applications, ranging from drug and gene delivery to targeted cell death (García-López et al., 2017; Schneckenburger, 2019; Xiong et al., 2016).

1.3 Optogenetics

The ability to modulate neuronal activity of specific neurons through external stimuli has always been very valuable in neuroscience as it allows to establish causal relationships between neuronal activity and behavioral outcomes, providing insights into the underlying mechanisms of brain function. Optogenetics was the pioneering stimulation tool in neuroscience using light as stimulation source, introducing the revolutionary concept of using genetically-encoded light-sensitive proteins to control and manipulate the activity of specific neurons (Fenno et al., 2011). These light sensitive proteins, microbial opsins, such as channelrhodopsin, halorhodopsin, and archaerhodopsin, as well as other light-sensitive ion channels and transporters are expressed in target neurons through viral vectors or transgenic approaches (Emiliani et al., 2022). When activated by light of specific wavelengths, they allow inflow or outflow of ions, bringing the neuronal membrane potential closer or further away from the threshold for Action Potential (AP) firing. This finally results in a light-dependent stimulation or inhibition of neuronal activity, allowing to precisely modulate neural circuits and investigate their functional roles (Boyden et al., 2005; Chow et al., 2010; F. Zhang et al., 2007). The great advantage of these optogenetic tools is first, their versatility as, depending on the light-sensitive molecule used, a different wavelength can be used to stimulate, and second their ability to be expressed in specifically targeted neuronal populations (Dugué et al., 2012; Fenno et al., 2011; Yizhar et al., 2011).

Optogenetics has been used, not only for fundamental research, but also studied for therapeutic approaches in various neurological and psychiatric conditions (Ordaz et al., 2017). In Parkinson's disease, researchers have targeted and modulated specific neuronal populations involved in motor control, aiming to restore normal motor function (Bordia et al., 2016). In epilepsy, optogenetics has been used to inhibit or disrupt abnormal electrical discharges in seizure-prone brain regions, potentially providing a novel approach for managing seizures (Walker & Kullmann, 2020; L. Zhang & Wang, 2021). Studies in depression have focused on modulating brain regions involved in mood regulation, exploring the potential for optogenetics to develop new treatments for mood disorders (Hare & Duman, 2020). In addiction research, optogenetics has been employed to investigate reward processing and addiction-related behaviors, identifying potential targets for intervention (Z. F. H. Cao et al., 2011). Additionally, optogenetics holds promise for vision restoration in retinal degenerative diseases by introducing light-sensitive proteins into remaining retinal cells to restore light sensitivity (Gauvain et al., 2021). These examples highlight the diverse therapeutic applications of optogenetics and light-dependent approaches in general, offering hope for novel interventions in a range of neurological and psychiatric disorders.

Despite its promising advantages, the clinical transition of optogenetics faces persistent safety concerns. Challenges include finding suitable viral vectors, addressing issues like diffusion, inflammation, and the potential incorporation of genes into the genome. Moreover, the expression of heterologous proteins from distant species introduces risks of undesirable immune responses and potential impairment of physiological cellular mechanisms (Diester et al., 2011). However, a significant milestone was reached in 2021 with the report of the first case demonstrating partial functional recovery after optogenetic therapy in a patient affected by a neurodegenerative disease (Sahel et al., 2021). This groundbreaking study paves the way for the potential use of optogenetics as a therapeutic strategy in humans.

1.4 Non-genetic optostimulation

In the quest for achieving spatiotemporal resolution comparable to that obtained with optogenetics, innovative nanotools are emerging as promising alternatives. These novel nanostructures offer the potential to create light-sensitive interfaces with target neurons, eliminating the necessity for genetic modifications. Diverse inorganic and organic bio-interfaces, spanning from planar interfaces to chromophores and nanoparticles, constitute advanced systems for neuronal modulation (Carvalho-de-Souza et al., 2015; Di Maria et al., 2018; Francia et al., 2022; Ghezzi et al., 2011; Maya-Vetencourt et al., 2020; Tochitsky et al., 2018). Activated at specific wavelengths, these state-of-the-art systems can deliver precise electrical or thermal stimuli to cells.

1.4.1 Inorganic interfaces

In the context of non-genetic strategies, inorganic interfaces for light stimulation stand out as pivotal instruments in the modulation of neuronal activity. These interfaces typically involve non-biological materials, often synthetic in nature, strategically designed to interact with neurons. Metal is generally used for its light-absorbing capabilities and the subsequent conversion of energy into heat, inducing a localized temperature increase, with typical lifetimes in the micro to millisecond range depending on dissipation paths (Nozik, 2001). An increase in temperature amplifies the kinetic energy of ions, enhancing the likelihood of their flow through the cell membrane. Consequently, this temperature-induced modulation of membrane voltage leads to neural excitation. This is particularly efficient in nanoparticles, due to the very large oscillator strength of the surface plasmons (Lanzani, 2012). Notably, they leverage their unique optical and physical properties, with the ability to exist in colloidal or water-soluble forms that facilitate their diffusion within tissues. Once within the tissue milieu, nanoparticles, such as gold nanoparticles, establish close interactions with neurons, showing remarkable abilities to convert near-

infrared (NIR) or visible light into photothermal energy and induce electrical polarization. These intricate interactions ultimately culminate in the excitation of neurons (Carvalho-de-Souza et al., 2015). Despite their potential for neural excitation, the use of these inorganic semiconductors in a biological context faces limitations due to potential cell toxicity. Significant temperature increases, a byproduct of these interactions, can be harmful to cells and tissues.

Another light-dependent inorganic approach involves stimulating neurons using photovoltaic pixels made of silicon photodiodes. These photodiodes consist of both positive and negative semiconductor materials that are connected together. When light is absorbed in the depletion region of the diode, it creates electron-hole pairs, resulting in the photovoltaic effect and the production of an electric current. Recent clinical studies have utilized this technique by either enhancing the electric currents through closely located electrodes (Stingl et al., 2017) or directly triggering neuronal firing through light stimulation (Palanker et al., 2020), allowing blind patients to experience visual perception. However, these methods can target only small areas due to the invasiveness of the physical structure of the photodiodes and the resolution is limited due to the electrode size and spacing.

1.4.2 Organic interfaces

A compelling solution to address biocompatibility concerns lies in the realm of organic interfaces, characterized by a molecular backbone consisting of carbon-carbon covalent bonds. This composition ensures high biocompatibility and seamless interaction with living tissues as they have a high degree of mechanical conformability due to weak supramolecular interactions. Among these, materials based on thiophene gained significant attention, being organic semiconductors extensively employed in photovoltaics, photodetection, and photonics.

Polythiophene derivatives, notably poly-3-hexylthiophene (P3HT) polymers and nanoparticles, emerge as key players in successful optostimulation applications. Used as extensive flat polymer layers, research indicates that primary neurons can grow in direct contact with them without compromising the optoelectronic properties of the active material or the biological functionality of the neuronal network. Upon exposure to light pulses, these materials transform light into localized currents, generating sufficiently strong signals to induce neuronal firing both *in vitro* (Feyen et al., 2016; Ghezzi et al., 2011; Martino et al., 2015; Rand et al., 2018) and *in vivo* (Maya-Vetencourt et al., 2017).

However, it's crucial to note that under high-intensity light conditions, this mechanism can still generate thermal energy. To mitigate this thermal effect, enhance diffusion, and bolster translational potential, P3HT nanoparticles have been successfully utilized and characterized (Benfenati & Lanzani, 2020; Francia et al., 2022; Maya-Vetencourt et al., 2020).

Despite the promise held by these non-genetic organic approaches, challenges persist. Light-dependent methods employing organic surfaces necessitate invasive procedures for application, and while nanoparticles exhibit significant potential, critical considerations regarding safety—such as long-term biocompatibility and clearance from the body—must be thoroughly addressed before clinical translation.

1.5 Photoswitches

In the array of non-genetic alternatives to optogenetics, chemical photoswitches emerge as valuable light-sensitive tools for neuroscience research. These small molecules possess the ability to undergo changes upon absorbing light, involving dipole alterations, charge separation, and solubility changes, among other mechanisms. Notably, a substantial portion of the approaches using photoswitches employed in biological contexts are based on their ability to undergo changes in molecular conformation upon illumination (Bandara & Burdette, 2012). These photoswitches have demonstrated efficacy in photostimulation, as their biological effects can be modulated in a reversible manner based on their spatial arrangement (Uchida, 2004; Russew & Hecht, 2010).

1.5.1 Photoswitch dynamics: light-electron interactions

The light sensitivity of photoswitches is grounded in the fundamental principles of light-electron interactions. Light, consisting of photons—quantized packets of energy within the electromagnetic spectrum—interacts with atoms in photoswitches. These atoms, surrounded by electrons distributed across distinct energy orbitals within their respective shells, can absorb the energy carried by photons. The energy of these photons is directly linked to the frequency of the incident light. When the energy of photons aligns with the energy difference between two electron levels within an orbital, electronic excitation occurs, allowing electrons to transition to higher energy states within the same shell. In the context of photoswitches, this excitation triggers a series of events, resulting in specific outcomes, such as isomerization or alterations in the molecule's dipole moment. Isomerization involves a structural reconfiguration of the molecule, often entailing the rotation of specific chemical bonds. Whereas changes in the dipole moment arise from the influence of absorbed energy on the distribution of the electron cloud, leading to an overall shift in charge distribution. These molecular changes are contingent on

frequency matching between the stimulating light and the atoms forming the photoswitch, underscoring the pivotal role of incident light frequency in photoswitch functionality. Importantly, these changes can be reversible, as electrons can revert to their initial states upon the release of absorbed energy. The specific outcome is intricately tied to the molecular design and nature of the photoswitch, allowing for tailored functionalization in response to light stimulation.

1.5.2 Biological applications of photoswitches

For these chemical photoswitches to be suitable for biological applications, certain desirable properties must be achieved. Firstly, they should exhibit biocompatibility to ensure minimal interference with biological systems. Additionally, water solubility is advantageous for efficient diffusion in cellular environments. Furthermore, stability against hydrolysis is crucial to maintain sustained and reliable functionality. Moreover, synthetic tractability plays a pivotal role, enabling not only facile synthesis of these compounds but also the ability to customize their properties, such as light absorption within specific spectra suitable for biological purposes (Merino, 2011). Once these properties are achieved, they open the door to diverse biological applications.

In November 2023, the pharmaceutical company Kiora announced the success of the first-ever clinical trial on humans using a photoswitch compound, KIO-301 (Kiora pharmaceuticals, 2023). The compound was delivered intravitreally to blind patients with degenerated photoreceptors, resulting in reported visual perception.

While these approaches achieve high temporal and spatial precision in stimulation, it is crucial to consider that these photoswitches may compete with physiological mechanisms. Additionally, the need for chronic injections to sustain their effects raises practical challenges and may pose limitations in long-term applications.

1.5.3 Photoswitches and membrane dynamics

The fundamental concept behind using photoswitches is to intricately interact with the cell membrane and its constituents avoiding genetic manipulation, thereby altering cellular activity in a light-dependent manner. Over time, diverse strategies employing photoswitches targeting various aspects of the cell membrane have been developed and extensively investigated.

One prominent strategy involves the modulation of neurotransmitter receptors and ion channels, with distinct approaches operating through the extracellular and intracellular spaces.

In one approach, neurotransmitter receptors and ion channels are modulated through the extracellular space. This was accomplished by constructing caged neurotransmitters, where neurotransmitters were bound to a photoswitch, rendering them inactive. Upon light stimulation of a specific wavelength, the photoswitch undergoes a conformational change, releasing the neurotransmitter and making it biologically active, allowing it to bind to its receptors. By injecting caged neurotransmitters and delivering light to specific brain regions, researchers can manipulate neuronal activity with high temporal and spatial resolution (Kramer et al., 2013). However, a drawback of this technique is its irreversibility; once the neurotransmitter is uncaged, rebinding to the photoswitch is not possible. An alternative approach exploits the reversibility of light-induced effects on chemical photoswitches by covalently linking the photoswitches to a channel ligand to allow direct interaction with endogenous ion channels. These compounds can be administered externally or systemically and selectively interact with specific neuronal receptors or ion channels, providing precise control over their activity. The conformational changes induced by light alter the affinity of these switches for their targets, resulting in either the activation or inhibition of neuronal activity in a light-dependent manner (Fuchter, 2020; Gorostiza & Isacoff, 2007). A new generation of photoswitches with high affinity labels have been engineered without the need to link them to further ligands, proving the possibility to induce a light-reversible blockade of voltage- or ligand-gated ion channels, therefore triggering neuronal activation or silencing (Mourot et al., 2013, 2018).

In a different approach, ion channels are modulated through the intracellular medium. This technique employs photoswitches that traverse the plasma membrane of specific neurons to block endogenous voltage-gated ion channels from the cytoplasmic side. Using a mouse model with degeneration-dependent heightened gene expression of purinergic P2X receptors, which have a cation-selective pore large enough for the photoswitch to permeate, this approach effectively blocks voltage-gated K^+ channels, hyperpolarization, and cyclic nucleotide-activated cation channels (HCN channels). This results in the suppression of firing in darkness and the facilitation of firing in a light-dependent manner (K. J. Cao et al., 2021; Tochitsky et al., 2017).

Finally, an alternative approach available, which inherently mitigates interference with physiological ion conductance processes, involves engineering photoswitches to enable their integration into the cellular bilayer. This allows them to modulate passive properties such as membrane capacitance or area in

response to light (Fujiwara & Yonezawa, 1991; Yonezawa et al., 1992) and lead to light-dependent firing activity (DiFrancesco et al., 2020).

1.5.4 Membrane-targeted photoswitches

Given the amphiphilic nature of these photoswitches, they spontaneously insert themselves into the cell membrane. Their unique characteristic of spanning from one side to the other of the leaflet, while being shorter than the physiological membrane thickness, is what ultimately leads to membrane thinning. This, in turn, results in the modulation of membrane capacitance or area. When exposed to light stimulation, the photoswitches undergo transient and fast conformational changes, triggering a reshaping of the cell membrane (Hinks et al., 2014; Höglsperger et al., 2023).

1.5.5 Azobenzene

Many of the aforementioned strategies rely on photoswitches with azobenzene at their core, an organic compound characterized by a unique structure with two nitrogen atoms connected by a double bond within a benzene ring (Figure 2). The stability of this structure is notably attributed to resonance and electron delocalization within the ring. This structural characteristic allows azobenzenes to undergo reversible isomerization between *cis*- and *trans*-configurations when exposed to specific light wavelengths (Bandara & Burdette, 2012; Hartley, 1937; Rau, 1973). The *trans* conformation of azobenzene is notably more thermodynamically stable than its *cis* counterpart, which establishes the *trans* isomer as the predominant configuration in the absence of light stimulation (Dias et al., 1992). In its *trans* state, the molecule exhibits near-planarity and a nearly negligible dipole moment. However, exposure to UV light induces an isomerization process, transforming azobenzene into the *cis* isomer characterized by a bent conformation and a dipole moment of approximately 3 Debye. This change also results in an approximate 3.5 Å change in length, a crucial property for various photostimulation applications. Reverting to the *trans* conformation requires either darkness or irradiation with 450 nm light

(Figure 2). Furthermore, the rapidity of isomerization, occurring on the picosecond timescale, makes azobenzenes particularly suitable for applications involving neuronal activation (Gagliardi et al., 2004).

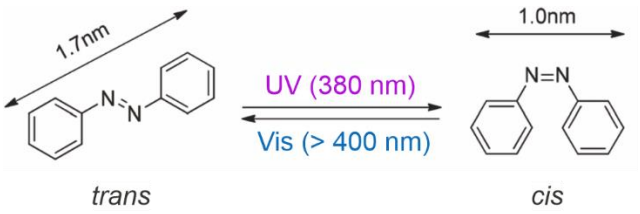

Figure 2 Light-Dependent Isomerization of Azobenzene
Illustration depicting the photochemical transformation of azobenzene molecules from the *trans* to the *cis* conformation in response to light exposure. The reversible isomerization of azobenzene serves as a dynamic molecular switch with potential applications in light-responsive materials and biological systems.

This structural adaptability is further amplified by the ease with which azobenzenes can be functionalized, allowing responsiveness to substituents on the benzene rings. Such responsiveness directly influences key isomerization properties, including the absorption wavelength for isomerization and the half-life of the *cis* isomer. Considering the potential phototoxicity associated with continuous UV light exposure to biological tissues, strategic engineering of photoswitches with substituents on the benzene ring becomes crucial. This strategic engineering not only addresses phototoxicity concerns but also enables the manipulation of azobenzene absorption bands, a critical aspect explored in various studies (Marturano et al., 2019).

Because of these features and the fact that photoisomerization process exhibits remarkable stability with minimal photobleaching, azobenzenes are well-suited for optimizing membrane internalization, ensuring thermal stability, and adjusting the spectral absorption range. This versatility makes them valuable for a range of biological applications (Bandara & Burdette, 2012; Crecca & Roitberg, 2006; Tavassoli et al., 2011).

1.5.6 Donor-acceptor molecules

As previously emphasized, the inherent attribute defining photoswitches is their reactivity to light. While the focus of examination has predominantly centered on the pivotal role of isomerization in photoswitch functionality, it is essential to consider a broader spectrum of their capabilities. Photoswitches exhibit the capacity for light-induced transformations by modulating their molecular dipole moments, introducing an additional layer of intricacy and significance to their functional repertoire. Within this context, donor-

acceptor photoswitches, characterized by a molecular structure comprising two components—a "donor" and an "acceptor" interconnected by a molecular bridge—represent a distinctive subclass of these light-responsive molecules. When exposed to light of a specific wavelength, the donor transfers an electron to the acceptor, leading to a modification in the molecule's dipole moment. In some cases this electron transfer can be reversible, enabling the molecule to transition between two distinct states in response to light. Molecules exhibiting such dipole changes upon light stimulation are also termed "Push-pull" molecules, as the electron is "pushed" by the donor and "pulled" by the acceptor. Therefore, the term "Push-Pull" serves as a descriptive means to underscore the electronic dynamics and electron movement within these molecules upon exposure to light.

In the case of membrane-targeted donor-acceptor photoswitches, their light-induced dipole changes can influence the local electric field across the membrane, resulting in a modification of the membrane voltage. If this change is substantial, it can either activate or inhibit voltage-gated ion channels, depending on whether it induces hyperpolarization or depolarization. Consequently, this leads to either neuronal activation or silencing in response to light. These molecules offer the advantage of acting on the passive properties of the cellular membrane without subjecting the cell to any mechanical stress.

1.6 Ziapin2

In the context of optostimulation, particularly in the realm of membrane-targeted azobenzene-based photoswitches, our laboratory has reported the characterization of Ziapin2 (DiFrancesco et al., 2020). Ziapin2 features a hydrophobic core incorporating the photoactive azobenzene, an azepane group, and two alkyl chains, terminating in a pyridine moiety (Figure 3A). This amphiphilic nature enables Ziapin2 to spontaneously insert itself into the cellular membrane, particularly within membrane rafts (Figure 3B). Integration into the lipid layer leads to the formation of localized trans-dimers, inducing membrane thinning.

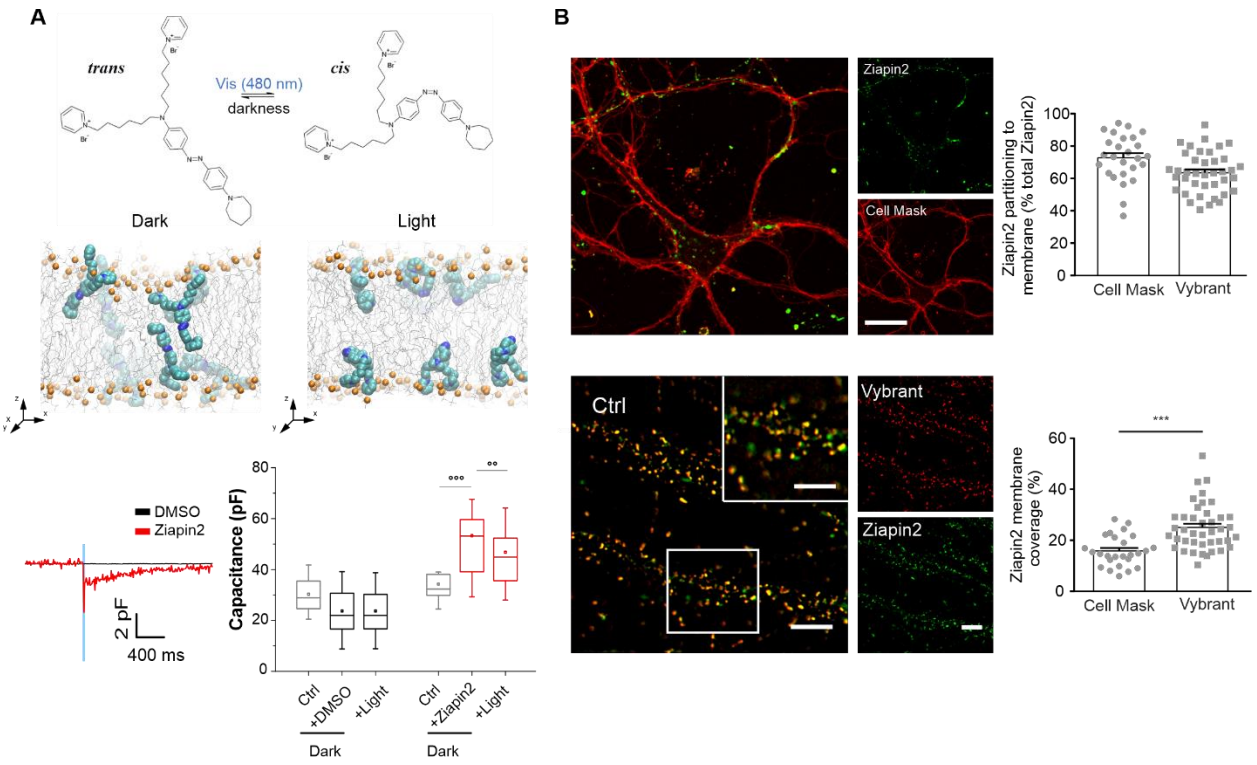

Figure 3 Ziapin2 insertion and modulation of the neuronal cell membrane

A. Molecular light-dependent conformation of Ziapin2: Molecular Dynamics simulations reveal the spontaneous insertion of Ziapin2 into the lipid bilayer, inducing local membrane depressions through dimer formation. Light-triggered isomerization transiently disrupts dimers, causing the membrane to relax, leading to a sudden decrease in membrane capacitance recorded in neurons**. B.** Live confocal imaging of primary neurons incubated with Ziapin2: Upper graph illustrates Ziapin2 (green) partitioning into the membrane, colocalizing with a cell membrane marker (CellMask, red). Lower graph shows Ziapin2 (green) specifically colocalizing with a marker of lipid rafts (Vybrant, red). Right panels quantify Ziapin2 colocalization with the markers and coverage of compound in these areas, providing insights into its interaction with lipid rafts.

Figure modified from DiFrancesco et al.,2020.

Specific engineering of azobenzene substituents shifts Ziapin2's absorption spectrum into the visible range making the needed light stimulation non-toxic to organic tissues. Millisecond pulses of visible light (470 nm) induce a transient *trans* → *cis* conformational change which leads to a transient disruption of the dimers and the relaxation of the membrane. In neurons, this translates to a light-dependent increase in firing activity through two cooperating mechanisms:

(1) Fast light-induced membrane capacitance drop: this generates hyperpolarization, followed by a slower increase at light offset as Ziapin2 reverts to its *trans* conformation and forms back dimers, inducing membrane capacitance increase.

(2) Anode break excitation: Membrane hyperpolarization may cause an 'anode break excitation' at light offset. The hyperpolarization results in a lowered threshold for action potential initiation by deactivating more Na^+ voltage-gated channels, enabling a larger pool of channels to be available for reopening when subjected to a new depolarization stimulus. As the hyperpolarizing stimulus ends at light offset, the cell's potential rises, initiating the opening of Na^+ channels. This sequence sets in motion a chain reaction, ultimately leading to the induction of an action potential (Figure 4). Synaptic transmission amplifies this depolarization, contributing to light-evoked firing through positive feedback within the network mediated by excitatory synaptic transmission.

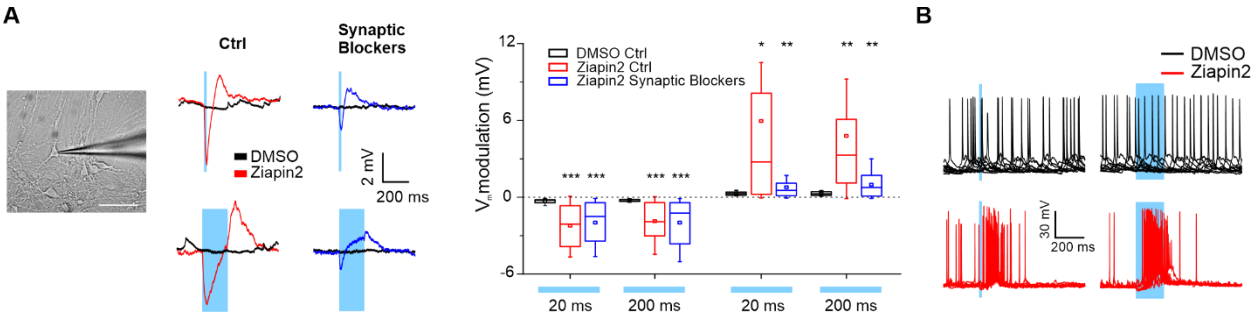

Figure 4 Ziapin2-mediated light-triggered modulation of membrane potential and neuronal firing
A. Primary neurons incubated with Ziapin2 exhibit a light-dependent hyperpolarization followed by a delayed depolarization. The right panel quantifies the membrane potential in vehicle-treated neurons (black), Ziapin2-treated neurons (red), and Ziapin2-treated neurons in the presence of blockers for excitatory and inhibitory transmission in the extracellular medium. The depolarization is significantly enhanced in the presence of synaptic transmission. **B.** Light-dependent increase in firing activity in neurons treated with Ziapin2 is illustrated in red traces, demonstrating the impact of Ziapin2 on neuronal excitability.

Figure modified from DiFrancesco et al.,2020.

Ziapin2 showed biocompatibility and efficacy in vivo as well. Specifically, it achieved light-dependent neuronal excitation without any inflammatory response when injected into the somatosensory cortex of mice. These results strongly support its potential in neuroscience research. However, the presence of Ziapin2 on the plasma membrane of primary neurons decreased over time due to membrane turnover, which finally led to a lowered efficacy in inducing light-triggered neuronal activation (DiFrancesco et al., 2020). This represents a significant challenge for translational studies involving this molecule.

2 Aims

Motivated by the promising outcomes observed with Ziapin2 in both *in vitro* and *in vivo* settings, this thesis aims to expand and enrich the field of membrane-targeted photoswitches with the following specific aims:

Aim 1: Investigate Ziapin2 light-dependent effects on synaptic transmission

To enable the potential application of Ziapin2 in complex neuronal networks, this thesis will explore the specific light-dependent effects of the photoswitch on excitatory and inhibitory neurons. Given that Ziapin2 concentrates in lipid rafts, which are present at the synaptic terminal level and that the two neuronal population differ in cell dimension, protein expression and synaptic mechanisms, we aim to specifically test possible effects on synaptic transmission in both neuronal subpopulations. It will be tested through patch-clamp experiments in primary hippocampal neurons.

Aim2: Characterize engineered compound 2Pyr-2Pyr

In pursuit of broader insights, this thesis will undertake a comprehensive characterization of an engineered variant of Ziapin2, designated as 2Pyr-2Pyr. This compound exhibits a structural deviation, featuring alkyl chains end-capped with Pyridine groups on both sides. Our objective is to elucidate the influence of this structural modification on membrane localization and permanence, light-triggered neuronal activity modulation and ascertain whether it enhances the compound's performance relative to the original molecule. This characterization will consist in molecular dynamics simulations, confocal live imaging, and patch-clamp recordings in primary hippocampal neurons.

Aim 3: Explore light-dependent membrane voltage modulation with azobenzene-based Push-Pulls photoswitches

Recognizing the potential advantages of alternative functional strategies in optostimulation, this thesis additionally aims to investigate the feasibility of inducing light-dependent membrane voltage modulation through the utilization of newly synthetized membrane-targeted photoswitches known as Push-Pulls that primarily rely on a donor-acceptor light-triggered response. The compounds will be tested on biocompatibility, membrane localization, and light-triggered membrane voltage modulation. This will be achieved through live imaging techniques and patch-clamp recordings in primary hippocampal neurons.

Aim 4: Investigate a unique azobenzene-free photoswitch

Lastly, this thesis will explore a distinct photoswitch, named BV-1 that sets itself apart from the previous ones by omitting the azobenzene core. Instead, it relies on intrinsic charge movements within its

molecular structure upon exposure to light for its photoactive properties. Given the distinct nature of this molecule, the aim is to conduct a comprehensive characterization. The characterization will involve assessing the compound's capacity for spontaneous integration into the lipid bilayer, its specific localization on the neuronal surface, the impact on membrane properties upon light exposure, the associated mechanisms, the assessment of cytotoxicity in both dark and light-stimulated conditions, and exploring potential applications. This comprehensive characterization will be approached through a multifaceted approach, employing molecular dynamics simulations, atomic force microscopy on lipid bilayers, live imaging, and patch-clamp recordings on primary hippocampal neurons. In the event of favorable outcomes, the prospective applications may extend to ex-vivo and in-vivo scenarios, envisioning the application of BV-1.

By accomplishing these objectives, this thesis aims to provide valuable scientific insights, thereby contributing to the advancement of non-genetic optostimulation approaches for the light-dependent modulation of neuronal activity, membrane voltage, and cell viability.

3 Materials and Methods

3.1 Ethical approval and animal handling

C57BL/6, rd10 mice, and GAD67-GFP knock-in mice were bred under standardized conditions, with free access to food and water, and maintained on a 12/12-hour light/dark cycle. GAD67-GFP knock-in mice were generated by inserting the cDNA encoding enhanced GFP into the GAD67 locus in TT2 embryonic stem cells, as described in (Tamamaki et al., 2003). Heterozygous GAD67-GFP males were mated with wild-type C57BL6/J females, and GFP-positive pups were identified at birth through a Dual Fluorescent Protein Flashlight (DFP-1, NIGHTSEA, Lexington, MA USA) and confirmed by genotyping, performed by PCR with the following primers: TR-1b:GGCACAGCTCTCCCTTCTGTTTGC; TR3:GCTCTCCTTTCGCGTTCCGACAG; TRGFP8:CTGCTTGTCGGCCATGATATAGACG. All animal manipulations and procedures adhered to the guidelines outlined by the European Community Council (Directive 2014/26/EU of 4 March 2014) and received approval from the Italian Ministry of Health (Authorization # 357/2019-PR).

3.2 Molecular dynamics simulations and quantal-mechanical calculations

All-atom MD simulations were performed in presence of a model membrane bilayer of 1-palmitoyl-2-oleoyl-phosphatidylcholine (POPC) made of 112 lipid molecules (56 per leaflet) and water. We simulated separately the spontaneous insertion of a single molecule in the membrane, and several molecules embedded in the membrane in dark and light configuration, where indicated. Starting coordinates for the systems were generated with the CHARMM-GUI web server (Jo et al., 2008), using pre-equilibrated lipid structures. All simulations were run with NAMD v2.12 code (Phillips et al., 2005) using the CHARMM36 force field (Huang & Mackerell, 2013) and the TIP3P model for water molecules. CHARMM-compatible topology and parameters for the compounds were obtained using the CHARMM General Force Field (CGenFF) (Vanommeslaeghe et al., 2010) and atomic charges from Time-dependent Density Functional Theory (TDDFT) calculations. The total electrostatic charge of each system was neutralized by the addition of physiological concentrations of counter ions. The time step for integrating the equations of motion was 2 fs, and covalent bonds to hydrogens were constrained using SHAKE (Ryckaert et al., 1977). Simulations were performed with periodic boundary conditions in the NPT ensemble, with P=1 atm and T=310 K, using a Langevin thermostat with a damping constant of 5 ps−1 and a Langevin piston with a constant decay of 100 ps−1 and an oscillation period of 200 fs. A flexible unit cell was used with constant ratio in the x–y

plane. Long-range electrostatic interactions were computed using the particle-mesh Ewald method, with a fourth-order spline and 1 Å grid spacing (Darden et al., 1998). The following simulations were performed: five, independent, 1 μs runs for spontaneous insertion in the membrane of a single photoswitch and two runs of 2 μs each with eight copies of the compound embedded in the membrane, in dark or light conformation. When multiple copies of the compounds were considered, they were distributed symmetrically in the upper and lower leaflet.

The electronic and optical properties of the photoswitches were investigated in the framework of time-dependent density functional theory (TDDFT) using the ORCA suite of programs (Neese, 2018; Neese & Wiley, 2012). A configuration of the solvated BV-1 was extracted from a preliminary MD trajectory and it was fully optimized using a revised PBE0 hybrid functional with 37.5% of exact exchange (Zhang & Yang, 1998), suitable for accurately describing the strong charge-transfer transition which dominates the absorption spectrum of BV-1, and the D3BJ dispersion correction (Grimme et al., 2010). The Kohn-Sham orbitals have been expanded on a Gaussian-type def2-TZVPP basis set (Schäfer et al., 1992). The corresponding def2/J basis was also used as an auxiliary basis set for Coulomb fitting in a resolution-of-identity/chain-of-spheres (RIJCOSX) framework. Time-dependent DFT calculations were performed using the same functional and the same basis sets; a large basis of 600 vectors connecting occupied and unoccupied Kohn-Sham orbitals was used for the calculations of the first 30 electronic transitions of the absorption spectrum of the molecule, shown as Gaussian convolution of electronic transitions (FWHM = 4000 cm-1). Solvent effects have been included in the calculations through the linear-response conductor-like polarizable continuum model (LR-CPCM) (Cammi et al., 2000). Mulliken charges obtained in the case of the ground and of the first singlet excited state using this setup were then employed to improve the accuracy of the force field in MD simulations, with the aim of introducing a realistic yet cost-effective differentiation between ground and excited state in large systems.

3.3 Cultures of primary hippocampal neurons

Low density preparations. Primary hippocampal neurons were obtained from WT C57BL/6 J mice sourced from Charles River (Calco, Italy). Animals were anesthetized by CO_2 inhalation and sacrificed by cervical dislocation. Embryos at embryonic day 17/18 were immediately extracted via cesarean section. Hippocampi were dissected in iced cold media and then incubated in 0.25% Trypsin-EDTA (Gibco ThermoFisher Scientific, Segrate, Italy) at 37 °C for 15 minutes for enzymatic digestion. Subsequently, the cells were mechanically dissociated using a fire-polished Pasteur pipette, and cell viability was assessed using the Trypan Blue exclusion assay. Neurons were plated onto poly-D-lysine (0.1 mg/ml, Sigma-

Aldrich)-coated 18-mm glass coverslips (4 × 104 cells/coverslip) in the culture media containing Neurobasal media (Gibco) supplemented with 2 % B27 (Gibco), 0.5 mM Glutamate (Gibco), and 1 % Penicillin-Streptomycin (Gibco) and kept at 37 °C in a 5 % CO_2 humidified atmosphere. All experiments were performed at 14-18 days in vitro (DIV).

Autaptic neuron preparations. To study Ziapin2 light-dependent modulation of synaptic neurotransmission in excitatory and inhibitory neurons, autaptic neurons were used. Primary hippocampal neurons were prepared from postnatal GAD67-GFP knock-in mice (P0–P1). dissociated neurons were plated at very low density (20 cells/mm^2) on microdots (40–400 µm in diameter) obtained by spraying poly-D-lysine (0.1 mg/ml) on dishes which had been pretreated with 0.15 % agarose the day before. Primary hippocampal neurons were obtained, dissociated and then cultured as described before for low density preparations. Patch-clamp experiments were performed at 17–23 days in vitro (DIV).

3.4 Light stimulation

All light stimulations during electrophysiological recordings were performed using a Spectra X Light Engine LED system (Lumencor, Beaverton, OR) fiber-coupled to an upright Nikon FN1 microscope (Nikon Instruments, Tokyo, Japan). The light source emission was in the cyan spectrum (470±10 nm) to match the photochromic molecules absorption spectrum. For the viability assay of BV-1-loaded neurons, cells were stimulated using a Eclipse-80i upright epifluorescence microscope (Nikon Instruments). The light source emission was filtered through an Iridian single band filter set optimized for fluorescein isothiocyanate (FITC) (470 nm). During live confocal imaging experiments with BV-1-loaded neurons, neurons were stimulated using a Hg fluorescence lamp (Leica Microsystems, Wetzlar, Germany). For all imaging configurations, the power density employed was 3 mW/mm^2 for BV-1 and 20 mW/mm^2 for the other molecules. These measurements were taken at the output of the respective microscope objective.

3.5 Cell viability assays

Primary hippocampal neurons were either incubated with the respective Vehicle (DMSO 2.5 %/H_2O, 0.1 %) or with Push-pull molecules /BV-1 (5 µM/ 1 µM) for 5 min at room temperature. Cells were then stained with propidium iodide (PI; 1 µM) for cell death and with Hoechst 33342 (1 µM) for nuclei visualization for further 5 min. Images were acquired at 10x (0.5 NA) magnification using an Eclipse-80i upright epifluorescence microscope (Nikon Instruments). Cell viability was obtained by the ratio of Propidium Iodide (PI)-/Hoechst 33342-positive cells. Cell viability was compared between neurons that were untreated, incubated with Vehicle or incubated with Push-pull molecules/BV-1. Neurons loaded with

either BV-1 or Vehicle were then subjected first to a train stimulation of 10 light pulses of 200 ms at 1 Hz, and then to a continuous illumination for 30 s. PI was present in the extracellular medium all along the experiment and cell viability was recalculated 5 min after each stimulation. Image analysis was performed using the ImageJ software and the Cell Counter plugin.

3.6 Patch-clamp electrophysiology

Whole-cell patch clamp recordings of low-density and autaptic primary hippocampal neurons were performed in the dark at room temperature (22-24 °C) using an EPC10 (HEKA Elektronik, Reutlingen, Germany) amplifier and the PatchMaster program (HEKA). Borosilicate glass pipettes (Kimble, Kimax, Mexico) with a 3–4 MΩ resistance were used. For all experiments, if not differently stated, pipettes were filled with an intracellular solution containing (in mM): 126 K gluconate, 4 NaCl, 1 $MgSO_4$, 0.02 $CaCl_2$, 0.1 BAPTA, 15 glucose, 5 HEPES, 3 ATP, and 0.1 GTP (pH 7.3 with KOH). The approximate concentration of free calcium in the intracellular solution was around 0.1414 µM. Cells were maintained in standard extracellular Tyrode solution containing (in mM): 140 NaCl, 2 $CaCl_2$, 1 $MgCl_2$, 4 KCl, 10 glucose, and 10 HEPES (pH 7.3 with NaOH). All chemicals were purchased from Sigma Aldrich (St. Louis, MO, USA), except for Tetrodotoxin (TTX) from Tocris Bioscience (Bristol, UK). Cells with leak currents >100 pA or series resistance (R) > 15 Ω were discarded. Hippocampal neurons were incubated with the respective Vehicle (DMSO/H_2O; 2.5 %/0.1;1 %, v/v) or Push-pulls, Ziapin2 or Branched molecules/BV-1 (2/0.1;1 µM) for 5 min at room temperature and then washed twice with extracellular medium. Neurons were recorded acutely after incubation (day 0) or 4 days after (when loaded with BV-1, day 4). Data analysis employed FitMaster software version 2.71 (HEKA), Origin 8.6 (OriginLab Corporation; Northampton), and GraphPad Prism 5 (GraphPad Software, Inc.).

Synaptic transmission in autaptic neurons. Autaptic neurons were voltage-clamped at −70 mV, and action potentials (APs) were elicited by depolarizing the cell body to +40 mV for 0.5 ms at a frequency of 0.1 Hz in the dark and during light stimulation. Evoked excitatory and inhibitory postsynaptic currents (eEPSCs/eIPSCs) were recorded at a sampling frequency of 10–20 kHz and filtered at half the acquisition rate using an 8-pole low-pass Bessel filter. Visual inspection of eEPSCs/eIPSCs ensured exclusion of those contaminated by spontaneous activity. For peak current calculation during an isolated stimulus or a train of stimuli, an averaged trace containing the stimulus artifact and the AP current, but lacking any discernable synaptic current (i.e., synaptic failures), was subtracted. Such traces were easily identified toward the end of a stimulus train, coinciding with maximal synaptic depression. These traces were averaged and normalized to the peak Na^+ current that may have contaminated the excitatory postsynaptic

current (EPSC). In analyzing the paired-pulse ratio (PPR), two brief depolarizing pulses were administered to autaptic neurons with a 50-ms interval in the dark and under light stimulation. For each pair of eEPSCs/eIPSCs, PPR was computed as the ratio I_2/I_1, where I_1 and I_2 represent the amplitudes of the EPSCs/IPSCs evoked by the conditioning and test stimuli, respectively. Then 40 repetitive stimuli administered at 40 Hz were applied to use the cumulative amplitude analysis to calculate the size of the readily releasable pool of synaptic vesicles (RRP_{syn}) and the probability (Pr) that any given synaptic vesicle (SV) within the RRP would be released. This calculation involved summing up peak postsynaptic current amplitudes over. The analysis assumes that the release probability (Pr) approaches 1.0 during the train and that depression during the steady-state phase is constrained by a constant recycling of synaptic vesicles with an equilibrium between released and recycled vesicles (Schneggenburger et al., 1999). The determination of the number of data points for the linear fitting of the steady-state phase was made by evaluating the best linear fit that includes the maximal number of points starting from the last data point (i.e., from the 40th evoked EPSC/IPSC). Linear regression was applied to the cumulative amplitude profiles of the final 15–20 data points, and the resulting regression line was back-extrapolated to time 0:

$$I_{fit}(x) = m \cdot x + b$$

The point where the regression line intercepted the Y-axis provided the size of the readily releasable pool of synaptic vesicles (RRP_{syn}):

$$RRP_{syn} = I_{fit}(0) = b$$

The probability (Pr) was obtained by calculating the ratio between the amplitude of the first excitatory postsynaptic current (I_1) and the determined RRP_{syn}.

$$P_r = \frac{I_1}{RRP_{syn}}$$

Light-induced neuronal activity modulation. To study light-dependent membrane voltage modulation in low-density neurons synaptically isolated from the neuronal network, D-AP5 (50 µM), CNQX (10 µM) and Bicuculline (30 µM) were added to the extracellular medium to block excitatory and inhibitory transmissions. Current-clamp recordings of light-induced depolarization were performed by holding the cell at its resting membrane potential (Ih = 0) and stimulating it with 7 subsequent 20 ms or 200 ms light pulses. The resulting depolarization was calculated in a 300 ms time window after each light pulse and compared to the basal membrane potential before stimulation. Modulation of membrane resistance was measured with current-clamp (CC) ramps driving the membrane voltage from -95 mV to -40 mV in 20 ms,

to calculate the corresponding slope of the recorded voltage traces. The protocol was repeated for 10 cycles in the dark, followed by 10 cycles with light pulses (200 ms) preceding the CC-ramp. To study the features of APs, train stimulation was used with 20 ms light-pulses at a frequency of 1 Hz holding the membrane voltage at -40 mV. Current-clamp recordings of the firing activity were sampled at 50 kHz and low-pass filtered at 10 kHz using an EPC10 amplifier (HEKA Elektronik), and the following parameters were measured: (i) half-width (ms), calculated at the membrane voltage of -20 mV; (ii) AP peak (mV) calculated as the most positive voltage reached during depolarization. The plot of the time derivative of voltage (dV/dt) vs voltage was then constructed (phase-plane plot) to extract: (i) maximal rising slope (mV/ms) from the positive peak; (ii) maximal repolarizing slope (mV/ms) from the negative peak. Four representative time-points were selected for each cell: one in the dark, and three during the light-stimulation protocol (t1, t2, and t3).

Study of subthreshold membrane properties. To study the contribution of voltage-gated ion channels to the light-induced depolarization, in addition to synaptic blockers, TTX (1 µM) was added to the extracellular medium to block voltage-gated Na^+ channels. Current- and voltage-clamp recordings were performed at a holding potential of -70 mV. Cells were stimulated with a 30-s train of light stimuli (1 Hz, 20 ms), and the membrane potential and inward current at the end of the 40-s trace were compared to the values at the beginning of the protocol, respectively. To evaluate the possible reversibility of the observed light-induced depolarization, neurons were incubated with either vehicle Vehicle (H_2O, 0.1 % v/v) or BV-1 (0.1 µM) and then stimulated with light pulses of increasing duration (20-3000 ms). The extent of depolarization was measured in two 300-ms time windows: the first starting at the light pulse offset (early depolarization), and the second at the end of the 8 s recording time (late depolarization). To study membrane permeabilization upon light stimulation, standard internal solution was used in combination with an extracellular solution, where Na^+ was replaced by choline (135 mM), and current- and voltage-clamp recordings were performed at a holding potential of -70 mV, as previously described.

Light-induced modulation of sodium and potassium conductances. In order to investigate the modulation of voltage-dependent sodium currents the intracellular solution contained (in mM): 120 Cs methanesulfonate, 4 NaCl, 0.02 CaCl2, 1 $MgSO_4$, 0.1 EGTA CsOH, 10 phosphocreatine, 3 ATP-Na_2, 0.1 GTP-Na, 10 HEPES (pH 7.3 with CsOH) and an external “"blocking” " solution containing (in mM): 120 NaCl, 3 KCl, 2 $CaCl_2$, 1 $MgCl_2$, 10 HEPES, 11 Glucose, 20 TEA-Cl, 1 4-aminopyridine, 0.5 $CdCl_2$. Membrane voltage was held at -40 mV, and voltage-dependent Na^+ currents were elicited through 5 mV voltage steps reaching 20 mV. The recorded traces were analyzed to obtain the voltage-current (I/V) curve and the time-

constant of current decay (corresponding to Na^+ channel inactivation) at -10 mV. Steady-state voltage-dependent K^+ currents were studied using standard intracellular and extracellular solutions and I/V curves were obtained by depolarizing neurons for 200 ms with voltage steps from -20 mV to 60 mV applied in 10 mV increments from a holding potential of -40 mV. Data were analyzed using FitMaster v2x90.1 (HEKA Elektronik) together with Prism 6.07 (GraphPad) and OriginPro 9 (OriginLab) softwares.

3.7 Light-induced membrane-patch perforation

BV-1 light-dependent membrane poration. To investigate the formation of pores on a membrane patch upon light stimulation, patch-clamp recordings were performed in cell-attached configuration. Pipettes were filled with K-Aspartate internal solution containing (in mM): 130 K-Aspartate, 10 NaCl, 10 HEPES (pH 7.3 with KOH). The patch pipettes were minimally front-filled with K-aspartate solution (from 1 to 5 s of tip immersion) and then backfilled with the same solution containing either BV-1 (diluted to a final concentration of 0.1 µM) or vehicle (H_2O; 0.1 % v/v). We measured the transient capacitive currents by applying a 20 ms depolarizing voltage pulse of 5 mV (V_{pulse}) from a holding potential of -70 mV, in the absence of light-stimulation (dark) or after successive cycles of illumination (200 ms, 3 mW/mm^2). The charge under the capacitive peak (Q_{peak}) was calculated by integrating the current traces (I(t)), subtracting the charge passing through the patch membrane resistance (Q_{res}) from the total charge (Q_{tot}), obtained as the whole area as follows:

$$Q_{tot} = \int I(t)dt$$

$$Q_{res} = R_{patch} \cdot V_{pulse}$$

$$Q_{peak} = Q_{tot} - Q_{res}$$

After giga-seal formation, the decrease in patch resistance after light-dependent perforation was calculated as the ratio between the voltage step and the amplitude of the steady-state current (ISS):

$$\Delta R_{patch} = \frac{V_{step}}{ISS}$$

3.8 Confocal live imaging

Photochromic molecules localization. Primary hippocampal neurons were incubated with the Branched molecules or BV-1 (5 µM/ 1 µM, 5 min) in culture media. To evaluate the distribution of the different

molecules, the neuronal surface was labeled with CellMaskTM (5 µM, 5 min) and live imaging was performed with a SP8/HyD confocal scanning microscope equipped with the super-resolution LAS-X Lightning deconvolution software (Leica Microsystems). Colocalization of the two fluorescent signals was analyzed using ImageJ plugin "JACoP".

Light-dependent cell-swelling in BV-1-loaded neurons. The observed swelling of neuronal soma of neurons incubated with BV-1 upon light stimulation was quantified using CellTrace™ Calcein Red-Orange (2 µM; ThermoFisher Scientific) as intracellular marker. Cells were first incubated for 5 min with either BV-1 (1 µM) or vehicle Vehicle (H_2O; 0.1 % v/v) and then with the fluorescent dye for 10 min at room temperature. The somatic area was first quantified in the dark and then 1 min after 1-s light stimulation. To study light-induced membrane permeabilization, neurons were first incubated with a Ca^{2+}-tracer (Biotracker609 Red Ca^{2+}-AM, 3 µM) for 30 min at 37 °C and then with either vehicle (H_2O; 0.1 % v/v) or BV-1 (0.1 µM) for 5 min. Calcium levels were acquired in the dark, immediately after a 3-s light pulse (t = 0 s) and 30 s later (t = 30 s). Sodium intracellular levels were monitored by incubating neurons with the Na^+ tracer (Ion NaTRIUM Green2-AM (2 µM; Interchim Bioscence, Montluçon, France). Given the overlap between the absorption spectra of BV-1 (λex 472 nm, λem 637 nm, see Figure 16A) and Ion NaTRIUM Green2-AM (λex 525, nm, λem 545 nm), either vehicle (H_2O; 0.1 % v/v) or BV-1 (0.1 µM) was added after acquisitions in the dark to avoid interference with the Na^+ tracer excitation. After 5 min, neurons were stimulated with a 3-s light pulse and Na^+ levels were acquired in the dark, at the light offset (early), and 30 s later (late).

3.9 Atomic force microscopy

BV-1-induced and Light-triggered membrane destabilization. POPC and ovine cholesterol (chol) were purchased from Avanti Polar Lipids Inc. (Alabaster, AL). Supported lipid bilayers (SLBs) were prepared according to previously described protocols (Mingeot-Leclercq et al., 2008). Briefly, POPC and POPC:chol=1:1 small unilamellar vesicles (SUVs) were prepared by first dissolving in chloroform and mixing the lipids at the indicated molar ratio. The solubilized lipids were then dried under a gentle nitrogen stream and left overnight under vacuum to remove any leftover traces of solvent. Subsequently, the dried lipids were resuspended into standard AFM buffer (150 mM NaCl, 20 mM HEPES-NaOH at pH 7.4, and 2 mM $CaCl_2$) and sonicated (ultrasonic bath, 40 kHz) for 30 min to generate SUVs. Before HS-AFM imaging, 2 µl of diluted SUV suspension (0.1 mg/ml) was deposited onto a freshly cleaved mica disk to form SLBs through vesicle fusion. After 15 min incubation, excess lipids were removed by thorough rinsing with standard AFM buffer. All AFM observations were performed in the tapping mode using a laboratory-built apparatus as previously described (Marchesi et al., 2021). Briefly, a glass sample stage (diameter, 2 mm;

height, 2 mm) with a thin mica disc (2 mm in diameter and ~ 0.1 mm thick) fixed on top with cyanoacrylate glue was attached onto the upper face of the z-scanner by a drop of nail polish. The sample stage with the SLB of choice adsorbed on top was immersed in a liquid cell filled with ~ 100 µl standard AFM buffer. Short cantilevers (BL-AC10DS-A2, Olympus) with nominal spring constant of ~ 100 pN/nm, resonance frequency of ~ 0.5 MHz, and quality factor of ~ 1.5 in water were used (Marchesi et al., 2018). An amorphous carbon tip was fabricated on the original AFM tip by electron beam deposition (~ 500 nm in length and apex tip radius of ~ 4 nm) and etched under argon plasma (Tergeo, PIE Scientific) to further sharpen the apex radius. The cantilever's free oscillation amplitude A0 and set point amplitude As were set at ~ 2 nm and around 0.9 x A0, respectively. Under these conditions, the energy delivered by a tip-sample interaction is 1–3 kBT on average (Marchesi et al., 2018). For sample irradiation, a blue LED diode (460 nm) was used. Light intensity and pulse width were manually controlled with a LED driver (LEDD 1B, ThorLabs) operated in constant current mode. The used LED power density after the objective lens was in the range of 11-12 mW/mm^2. All experiments were performed at room temperature (24-26 °C) and dark ambient conditions. Data were collected using laboratory-developed software based on Igor Pro 8 (WaveMetrics) and Visual Basic.NET (Microsoft) (Puppulin et al., 2021). HS-AFM movies were x,y-drift-corrected using the ImageJ plugins "Template Matching and Slice Alignment" "(https://sites.google.com/site/qingzongtseng/template-matching-ij-plugin). Image flattening was achieved by means of plane or second order polynomial surface fitting, as appropriate. Afterwards, median (0 order) line-by-line leveling was used to remove height offsets along the fast scan axis (Zuttion et al., 2018). These steps were performed using in-house software routines developed in MATLAB (MathWorks), available at https://github.com/arin83/U1067/.

3.10 Multielectrode array recordings in blind retinal explants

BV-1 applied on blind retinal explants. Dystrophic retinas were dissected from the enucleated eyes of 12-month-old retinal degeneration 10 (rd10) mice carrying a spontaneous mutation of the rod-phosphodiesterase (PDE) gene leading to a rod degeneration that starts around P18. Eyes were enucleated and transferred to a Petri dish with carboxygenated Ames medium (Sigma-Aldrich, Milano, Italy). The dissection procedure was performed in dim red light. After the removal of cornea, iris, lens, and vitreous, each retina was dissected from the sclera and subdivided into pieces and kept oxygenated in Ames medium. Each piece was incubated with either BV-1 (5 µM in Ames medium) or PBS (10 % H_2O in Ames medium) for 30 min, subsequently washed in fresh recording medium and positioned RGC side down onto a 60 electrodes MEA chip using the MEA1060-inv system (Multi Channel Systems MCS GmbH,

Reutlingen, Germany). Light-evoked extracellular activity was obtained with a fiber-coupled Spectra X Light Engine LED system (Lumencor) peaking at 460 nm fed to an inverted Eclipse Ti microscope (Nikon Instruments). The illumination spot covered an area of about 1 mm^2 at 0.5, 1 and 3 mW/mm^2. Data were acquired at 25 kHz and filtered between 200 Hz and 3 kHz. Spike detection was performed using MC Rack software (Multi Channel Systems). After the recording of a period of baseline firing in the dark, a 200-ms light pulse protocol administered at 1 Hz was employed at increasing power densities. Each power density protocol lasted 100 s (100 sweeps).

3.11 In vivo injection and extracellular recordings in the primary visual cortex

BV-1 injection in the primary visual cortex (V1). Naïve C57BL/6 mice (Charles River) were anesthetized with xylazine (5 mg/kg) and ketamine (50 mg/kg) and placed in a stereotaxic frame (World Precision Instruments, Sarasota, FL) for surgery. Mice were injected in the binocular portion of V1 (OC1b; stereotaxic coordinates: 2.7 mm from the intersection between the sagittal and lambdoid sutures and ~400 µm ventral to brain surface) with 1 µl of either BV-1 (500 µM in PBS) or Vehicle (10% H_2O in PBS) using a 5-µl Hamilton syringe. A hole in the skull was drilled in correspondence of OC1b, the dura mater was gently removed after the exposure of the brain surface and the injection was done at a rate of 500 nl/min with a nano-jector (World Precision Instruments, Fl, USA), keeping the needle in place for additional 20 min.

BV-1 in vivo extracellular recordings. Five min after the injection, anesthetized C57BL/6 mice were subjected to an extended craniotomy to perform in vivo recordings. After 60 min of recovery, an optic fiber cannula (400 µm in diameter; 50° normal to the skull; Doric Québec, Canada) and a glass micropipette (2-4 MΩ, filled with 3 M NaCl) were inserted in OC1b (350 µm depth) to reach the injected area. Pulsed light stimulation (430 nm, 40 mW/mm^2) was delivered 100-200 times at 0.25 and 1 Hz (200 ms), while prolonged light stimulation was subsequently administered for 30 and 60 s. Extracellular signals in response to stimulation were amplified and band-pass filtered (1-3000 Hz) by a NeuroLog system (Digitimer Ltd, Welwyn Garden City, UK), and finally digitized through a multifunction I/O device (NI USB-6251; National Instrument Co., Austin, TX). The same application software (MATLAB R2022b) was employed to drive both light stimulation and signal acquisition through a customized application. During the recordings, both eyes were maintained closed to avoid contamination by physiological visual signals from the retina. Mice reflexes and body temperature (36-37 °C) during the experiments were monitored and were stable. After recordings, mice were euthanized for imaging and immunohistochemical analysis.

Firing rate analysis. Extracellular signals were high-pass filtered (500 Hz) and spike detection was set above 5.5-fold the standard deviation (SD) of the baseline. As readout of light-induced firing rate modulation, we measured the average ratio between the highest firing rate (10 s bins) after and before each stimulation protocol. MATLAB R2022b software was employed to perform data analysis.

3.12 Visual cortex immunohistochemistry

Immunohistochemistry of BV-1-injected brain sections. Mice were transcardially perfused with 4 % paraformaldehyde (PFA) and then subjected to cervical dislocation. Brains were extracted, post fixed in 4 % PFA in 0.1 M PBS overnight, extensively washed in 0.1 M PBS. Brain sections of 40 µm thickness were obtained using a vibroslicer (Vibratome 5100mz, Camden Instruments, Loughborough, UK), cryo-protected by equilibration with 30 % sucrose and incubated in Freezing solution (3% Ethylene Glycol, 0.2% Glycerol in PBS) at - 20°C. Brain sections were first incubated in blocking solution (0.1 M PBS, 10% bovine serum albumin, BSA, 1% Triton X-100) for 1 h at room temperature, and then incubated overnight at 4 °C with rabbit anti-active cleaved caspase-3 (#AF835; 1:50 dilution; RD System,). Alexa Fluor 647-conjugated secondary antibodies (Alexa 488-conjugated secondary antibodies hosted in goat, ThermoFisher Scientific) were diluted 1:100 and incubated at room temperature for 1 h. After counterstaining with Hoechst 33342, sections were let dry and mounted with Mowiol. Brain sections were imaged with a SP8 confocal laser scanning microscope (Leica Microsystems). The levels of induced cell death in the proximity of the BV-1 injection sites were quantified based on Hoechst 33342 and cleaved caspase-3 (CC 3) stainings within 20 µm z-stack volumes, acquired at 512 x 512 resolution and compared with the corresponding vehicle-injected areas. The percentage of cell death was calculated as the ratio between caspase-3 positive cells and total number of Hoechst 33342-labeled cells in the stack.

3.13 Statistical analysis

Data are shown as box plots or means ± SEMs with superimposed individual experimental points. The box plots elements are: center line, median (Q_2); square symbol, mean; box limits, 25th (Q_1)-75th (Q_3) percentiles; whisker length is determined by the outermost data points within 3-fold the interquartile range (Q_3-Q_1). Normal distribution of data was assessed using the D'Agostino-Pearson's normality test. The F-test was used to compare variance between two sample groups. To compare two normally distributed sample groups, the unpaired or paired Student's t-test was used, as appropriate. To compare two sample groups that were not normally distributed, were used: the Mann-Whitney's U-test and Wilcoxon test were used for unpaired and paired data, respectively. To compare more than two

experimental groups, one- or two-way ANOVA/Šídák's tests and Kuskal-Wallis/Dunn's tests were used in case of normal or non-normal distribution, respectively. A p value < 0.05 was considered significant. Statistical analysis was carried out using OriginPro-8 (OriginLab Corp., Northampton, MA, USA) and Prism (GraphPad Software, Inc.).

4 Results

4.1 Ziapin2

Previous studies have established that Ziapin2 possesses the capacity to induce light-triggered action potentials through its ability to alter membrane capacitance via spontaneous incorporation into the cellular membrane, particularly within lipid rafts (DiFrancesco et al., 2020). Lipid rafts represent specialized microdomains within the cellular membrane, characterized by their heightened concentrations of cholesterol and sphingolipids, known to selectively concentrate specific proteins (Lingwood & Simons, 2010). In neurons, accumulating evidence has shown that both the presynaptic and postsynaptic sites are highly enriched in lipid rafts, which are likely to organize and maintain synaptic proteins in their precise localization, impacting synaptic plasticity and vesicle trafficking (Allen et al., 2007; Hering et al., 2003; Korade & Kenworthy, 2008; Sebastião et al., 2013). The sudden alteration in membrane thickness, particularly within the lipid rafts, has the potential to affect the activity of proteins situated within these areas. Consequently, this could give rise to distinct alterations in synaptic neurotransmission, contingent upon the specific proteins that are present. Given the structural variations and differential protein expression observed between excitatory and inhibitory neurons, especially at the presynaptic terminal, we hypothesized that Ziapin2 might induce diverse effects in these two neuronal subpopulations.

4.1.1 Light-modulated post-synaptic currents: synaptic profile-dependent modulation

To unambiguously identify inhibitory and excitatory neurons, we used heterozygous mice expressing the fluorescent reporter GFP under the control of the glutamic acid decarboxylase 67 (Gad67) promoter, which specifically expresses GAD67, an enzyme involved in the synthesis of GABA (Erlander et al., 1991), in inhibitory neurons. Specifically, we used GAD67 hippocampal neuronal cultures and categorized them based on their strong positivity or negativity to GFP, allowing us to distinguish between inhibitory and excitatory neurons, respectively (Figure 5A). This strategy allowed us to examine the effects of Ziapin2 in the dark and during light stimulation on these distinct synaptic profiles. We first confirmed that the light-dependent increase in firing activity observed in our previous study (DiFrancesco et al., 2020) could be obtained in a similar extent in both excitatory and inhibitory neurons incubated with Ziapin2 (Figure 5B). To then focus specifically on the light-triggered effects on synaptic neurotransmission, we employed autaptic hippocampal neurons, which enabled the precise recording from isolated neurons (Valente et al.,

2015) (Figure 6A). This isolation is valuable for investigating the specific characteristics of individual neurons without the confounding influences of neighboring cells. Employing patch-clamp recordings in this configuration allows for the detailed exploration of postsynaptic currents with high temporal and spatial resolution, given that the presynaptic terminals and the postsynaptic sites belong to the very same neuron.

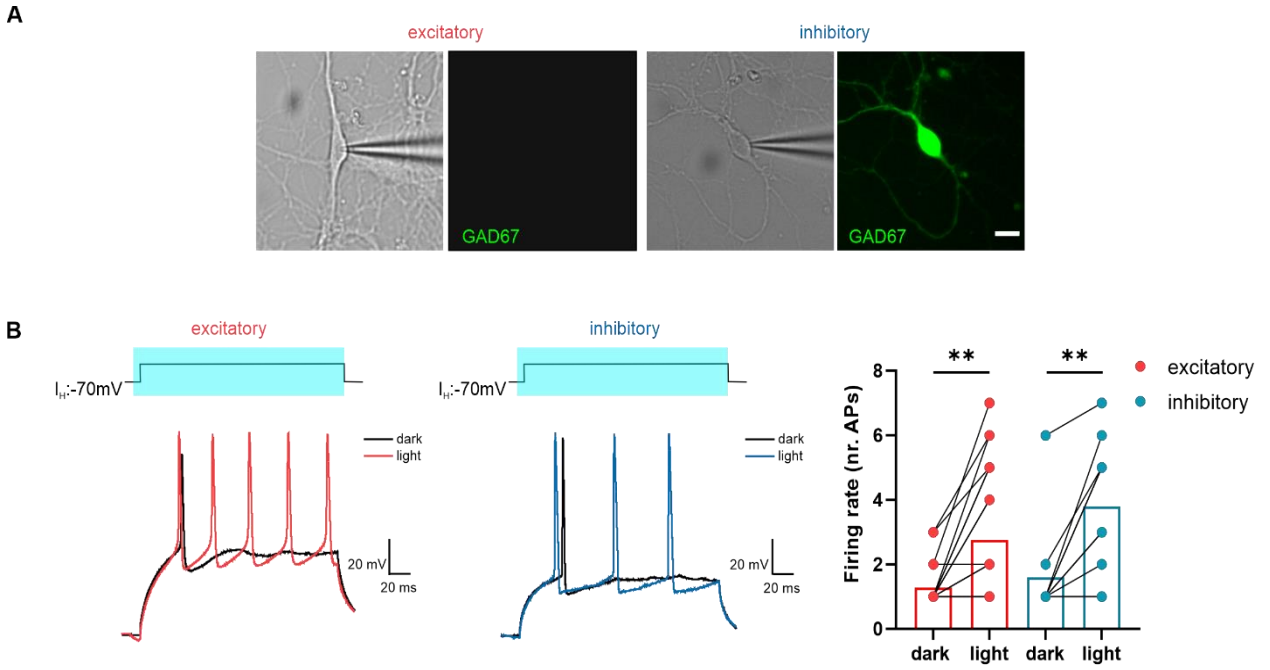

Figure 5 Ziapin2 increases firing activity in excitatory and inhibitory neurons from low-density hippocampal cultures

A. Representative GAD67+ hippocampal cultures categorized into excitatory and inhibitory neurons based on their negativity or strong positivity to GFP+, respectively. **B.** Representative recordings of action potentials (APs) evoked by a depolarizing current step lasting 190 ms in the dark and during light stimulation (200 ms, 20 mW/mm^2) in excitatory and inhibitory neurons incubated with Ziapin2 (*left)*. All recordings were performed in the presence of synaptic blockers in the extracellular medium to isolate the recorded neuron from network activity. Quantification of evoked APs in the dark and during light stimulation in both neuronal subpopulations (*right*) (n= 21 excitatory, n= 11 inhibitory).

*Statistics: **p<0.01, paired Student's t-test (dark vs. light) (B).*

Consequently, autaptic neurons present an unparalleled opportunity to study synaptic transmission and plasticity. Specifically, we triggered neuronal firing by depolarizing the recorded neurons to + 40 mV for 0.5 ms using two consecutive stimuli at an interstimulus interval (ISI) of 50 ms in the dark and during light stimulation and recorded the amplitude of the two evoked excitatory (eEPSCs) and inhibitory (eIPSCs) synaptic currents (Figure 6A). Subsequently, we explored the paired-pulse ratio (PPR), a parameter reflecting short-term plasticity phenomena at the presynaptic side that could be influenced by the

transient light-triggered effects induced by Ziapin2. PPR is determined by calculating the ratio between the amplitude of the second response and the amplitude of the first response elicited by the two consecutive stimuli. A second response larger than the first one (PPR > 1; paired-pulse facilitation) suggests an increased probability of neurotransmitter release with the second pulse, while a second response smaller than the first one (PPR <1; paired-pulse depression) indicates a reduction in release probability. Excitatory and inhibitory neurons operate at distinct baseline probabilities of release (low for excitatory neurons and high for inhibitory neurons) so that excitatory neurons are predominantly facilitating and inhibitory neurons mainly depressing when challenged with paired stimuli. This dichotomy is crucial for sustaining a physiological network balance between excitation and inhibition (Bhatia et al., 2019).

In excitatory neurons treated with vehicle (DMSO), the first eEPSC showed no light-dependent modulation, whereas neurons incubated with Ziapin2 displayed a significant increase in the EPSC amplitude following light stimulation (Figure 6B,C). Interestingly, excitatory neurons incubated with Ziapin2 displayed a significant decrease in synaptic facilitation during light stimulation compared to darkness (Figure 6B,C), suggesting a light-dependent increase of the probability of release in the presence of Ziapin2. When inhibitory autaptic neurons treated with Ziapin2 were investigated with the same experimental paradigms, we observed an opposite modulation of the eIPSC amplitude and PPR in response to light, with a decrease in the amplitude of the first eIPSC upon light stimulation associated with an increased PPR (Figure 6D,E), indicating a reduction in synaptic depression compared to the dark condition.

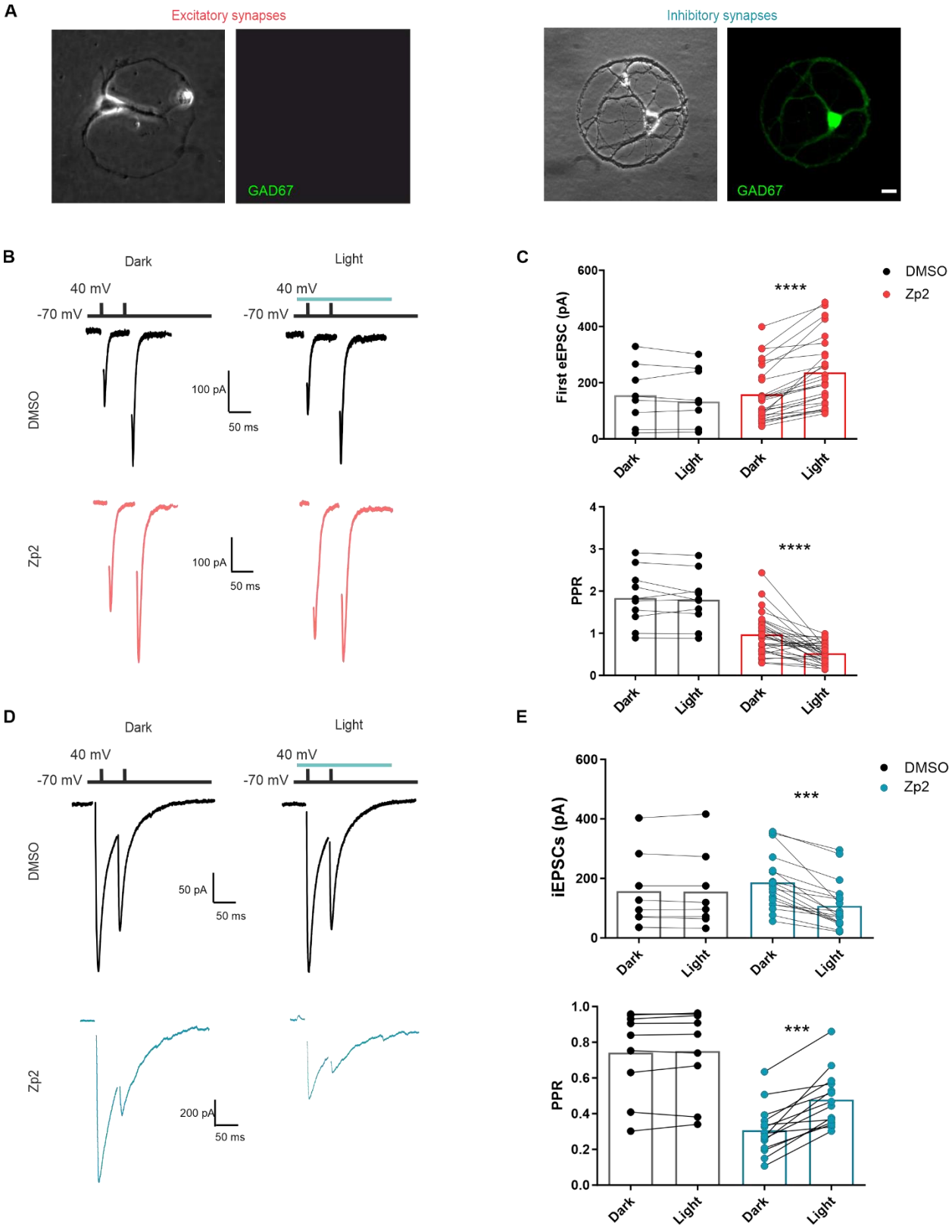
A
Excitatory synapses
GAD67
Inhibitory synapses
GAD67
B
Dark
Light
40 mV
-70 mV
DMSO
100 pA
50 ms
Zp2
100 pA
50 ms
C
DMSO
Zp2
First eEPSC (pA)
600
400
200
0
****
Dark
Light
Dark
Light
PPR
4
3
2
1
0
****
Dark
Light
Dark
Light
D
Dark
Light
40 mV
-70 mV
DMSO
50 pA
50 ms
Zp2
200 pA
50 ms
E
DMSO
Zp2
iEPSCs (pA)
600
400
200
0
***
Dark
Light
Dark
Light
PPR
1.0
0.8
0.6
0.4
0.2
0.0
***
Dark
Light
Dark
Light

Figure 6 Ziapin2 modulates the amplitude of evoked PSCs in a light-dependent manner
A. Representative GAD67$^+$ autaptic hippocampal neurons categorized into excitatory and inhibitory neurons based on their negativity or strong positivity to GFP+, respectively. **B.** Representative eEPSCs recordings evoked by a depolarizing pulse at +40 mV lasting 0.5 ms from a holding potential of -70 mV in excitatory autaptic neurons incubated with either Vehicle (DMSO, 0.25 %) or Ziapin2 (5 µM). The protocol was first performed in the dark and then during 100 ms light stimulation (20 mW/mm^2). In all traces, stimulation artifacts were blanked for clarity. **C.** *Upper panel:* Quantification of first eEPSC in the dark and during light stimulation in neurons incubated with either Vehicle or Ziapin2. *Lower panel:* Quantification of paired-pulse ratios (PPRs) in the dark and during light stimulation in both experimental groups (n= 8 DMSO, n=25 Ziapin2). **D.** Representative eIPSCs recordings evoked by a depolarizing pulse at +40 mV lasting 0.5 ms from a holding potential of -70 mV in inhibitory autaptic neurons incubated with either Vehicle (DMSO, 0.25 %) or Ziapin2 (5 µM). The protocol was first performed in the dark and then during 100 ms light stimulation (20 mW/mm^2). In all traces, stimulation artifacts were blanked for clarity. **E.** *Upper panel:* Quantification of first iPSC in the dark and during light stimulation in both neurons incubated with the Vehicle and with Ziapin2. *Lower panel:* Quantification of paired-pulse ratios (PPRs) in the dark and during light stimulation in both experimental groups (n= 16 Ziapin2, n=9 DMSO).
*Statistics: ***p<0.001, paired Student's t-test (dark vs. light) (C,E).*

4.1.2 Modulation of release probability by Ziapin2 upon light stimulation

The observed variations in PPR suggest changes at the presynaptic terminal, involving modifications in neurotransmitter release dynamics, such as alterations in the number or fusion probability of synaptic vesicles (SVs) ready for release. To delve deeper into the observed phenomena in neurons treated with Ziapin2, we studied the specific quantal release parameters influenced by the light-dependent modulation. Our approach involved a cumulative analysis of eEPSC amd eIPSC amplitudes in the presence of Ziapin2, both in the dark and during light stimulation. This method involves the analysis of the cumulative amplitude profile during high-frequency trains of stimuli (Figure 7A), enabling the extraction of the probability of release (Pr) and the size of the ready releasable pool (RRP) of SVs (Schneggenburger et al., 1999; Baldelli et al., 2007). When excitatory neurons were subjected to a 40 Hz train for 2 s, a significant depression in eEPSCs was observed, regardless of the amplitude of the first current in the train (Figure 7A). The assumption made by this method is that when Pr approaches unity during the train, the depression during the steady-state phase is constrained by a constant recycling of SVs. Accordingly, the cumulative profile displayed a rapid initial rise followed by a slower linear increase, reflecting the equilibrium between depletion and replenishment of the RRP (Figure 7B,D).

In the presence of Ziapin2, excitatory neurons exhibited an increase in release probability during light stimulation with no significant changes in the RRP size between dark and light conditions (Figure 7C). This finding aligns with our earlier observations, revealing an augmented first eEPSC and a subsequent decrease in PPR. Considering that release probability is primarily affected by the extent of calcium entry

in response to the action potential (Catterall & Few, 2008), these data suggests a potential upregulation of these currents during light stimulation, thereby contributing to the heightened release probability without impacting the RRP. In inhibitory neurons, a distinct neurophysiological pattern emerged. In this neuronal population, exposure to light induced a reduction in the RRP without concurrent changes in release probability (Figure 7E). This observation suggests that the light-triggered membrane stretch induced by Ziapin2 might interfere with the coupling of calcium influx through voltage-gated calcium channels (VGCCs) and SVs fusion at the active zone. This uncoupling causes nearby SVs to leave the functional RRP, despite the fact that the docked vesicles remain physically stationary (Nanou & Catterall, n.d.; Wadel et al., 2007). The divergent Ziapin2-mediated responses observed during light stimulation in excitatory and inhibitory neurons underscore the importance of the physiological machinery Ziapin2 is modulating. These differences may in fact arise from physiological differences in SV pools, release mechanisms, and VGCCs between the two distinct neuronal subpopulations.

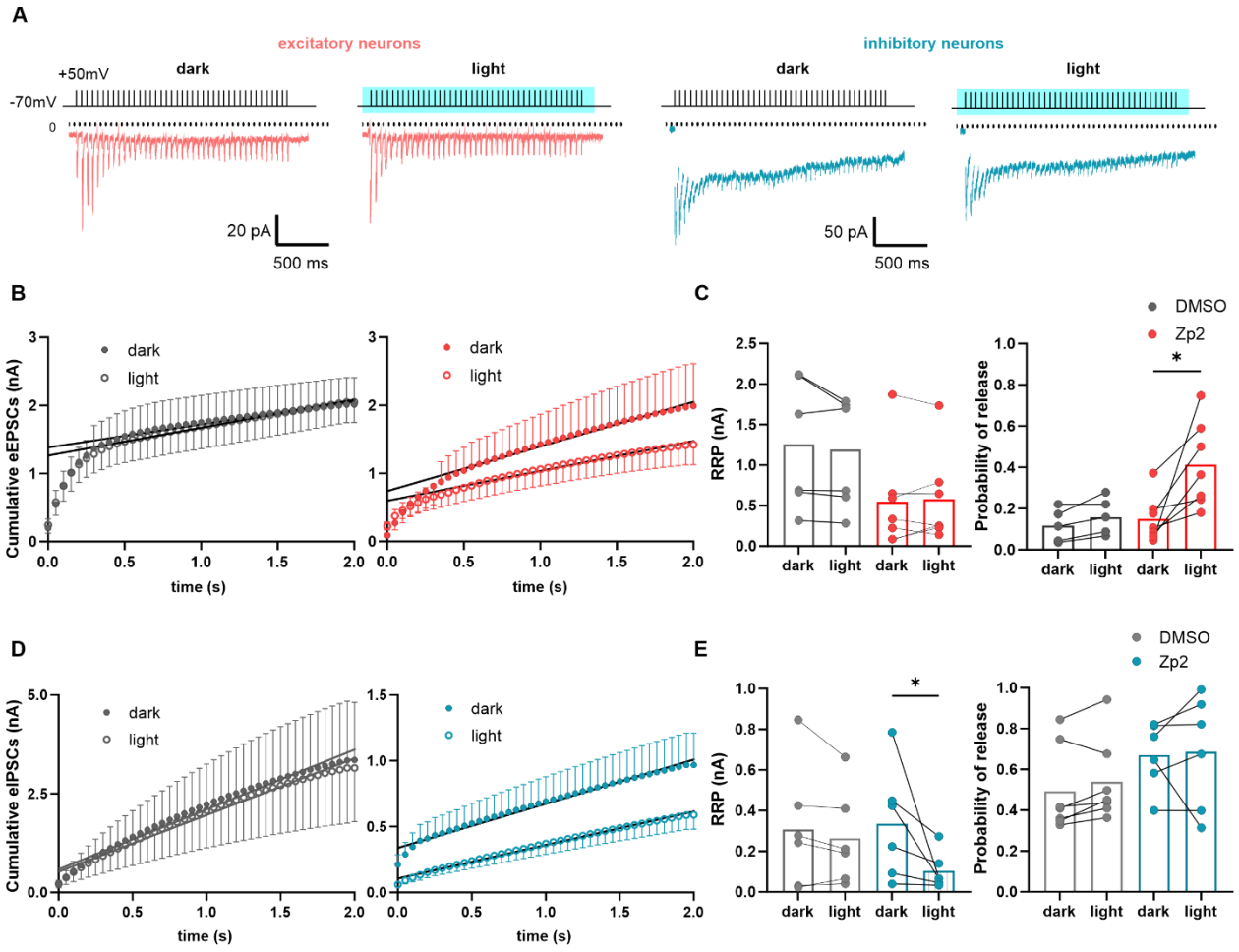

Figure 7 Light modulates synaptic transmission in neurons incubated with Ziapin2

A. Representative traces showing the 2-s stimulation protocol at 40 Hz used to estimate the quantal properties of synchronous release in the dark and during light stimulation in excitatory (red traces) and inhibitory neurons (blue traces) autaptic hippocampal neurons incubated with Ziapin2. **B.** Cumulative curves of eEPSC amplitude during the stimulation train in the dark and during illumination in excitatory neurons incubated with either DMSO (*left;* black) or Ziapin2 (*right;* red) are shown as means ± SEM together with the linear regression fit to their linear phases. **C.** Box plots of the RRP size (*left*) and release probability (*right*) for excitatory neurons incubated with either DMSO (black) or Ziapin2 (red) (n= 5 DMSO, 7 Ziapin2). **D.** Cumulative curves of eIPSC amplitude during the stimulation train in the dark and during illumination in inhibitory neurons incubated with either DMSO (*left;* black) or Ziapin2 (*right;* red) are shown as means ± SEM together with the linear regression fit to their linear phases. **E.** Box plots of the RRP size (*left*) and release probability (*right*) for excitatory neurons incubated with either DMSO (black) or Ziapin2 (blue) (n= 7 DMSO, n=6 Ziapin2).

*Statistics: *p<0.05; Wilcoxon's test (B,E)*

4.2 2Pyr-2Pyr

4.2.1 2Pyr-2Pyr spontaneously partitions into the membrane and modulates membrane capacitance without the formation of dimers

The photochromic molecule investigated in this study was synthesized with the aim of improving upon the characteristics of Ziapin2. Ziapin2 relies on the interaction of two photoswitches positioned on opposite leaflets of the cellular membrane, forming dimers that locally decrease membrane thickness (DiFrancesco et al., 2020). Upon light-triggered isomerization, these dimers transiently disrupt, resulting in a relaxation of membrane thickness. The branched molecule with four polar branches, named 2Pyr-2Pyr because of the presence of two Pyridine groups on each side, has the potential to bypass the dimerization requirement by combining all necessary components into a single molecule while maintain the light sensibility in the cyan spectrum (Figure 8).

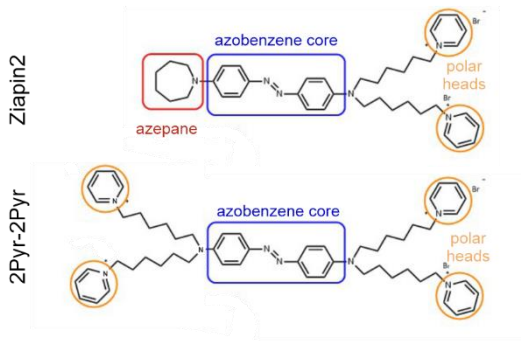

Figure 8 2Pyr-2Pyr, the evolution of Ziapin2.
Compared molecular structure of Ziapin2 and 2Pyr-2Pyr. 2Pyr-2Pyr was engineered with twin Pyridine heads embracing the azobenzene core, replacing the azepane present in Ziapin2.

Through Molecular Dynamics (MD) simulations, we observed that a spontaneous insertion into the cellular membrane is predicted with 2Pyr-2Pyr (Figure 9), as previously observed with Ziapin2 (DiFrancesco et al., 2020). After 800 ns the molecule partitions into the outer leaflet of the membrane, aligning all four Pyridine terminals with the lipid heads of the membrane (Figure 9). To enable additional characterization through MD simulations, we initiated the process by assuming that the molecules would ultimately traverse the lipid bilayer from one leaflet to the opposite leaflet and we closely monitored their behavior under dark conditions (Figure 10).

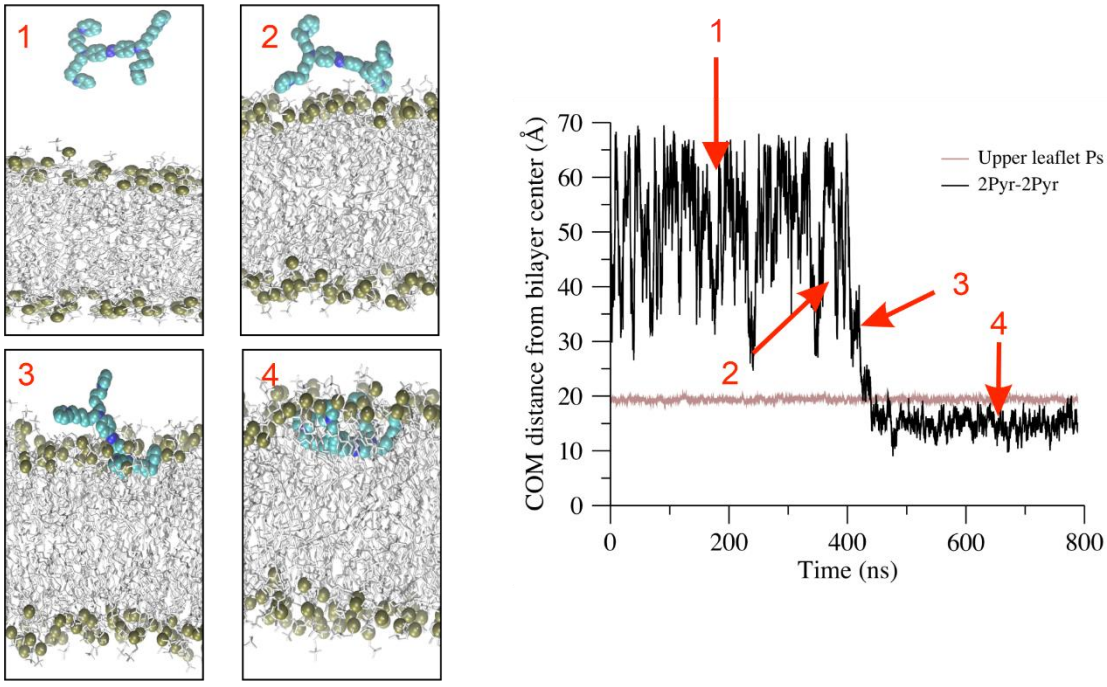

Figure 9 2Pyr-2Pyr spontaneously partitions into the lipid bilayer
Left: Snapshots extracted from MD simulations showing 2Pyr-2Pyr (trans isomer) spontaneously entering the membrane (POPC lipid model) at four consecutive time frames (1-4). Lipid phosphate atoms are shown as tan spheres and acyl chains as grey lines; water molecules are not reported for clarity. *Right:* The graph shows the time-dependence of the distance between the center of mass (COM) of 2Pyr-2Pyr and the bilayer center during the simulation; the brown line is the average position of the upper leaflet lipid head groups.

What we observed is that over time, the photoswitches exhibit a tendency to aggregate, resulting in localized thinning of the membrane (Figure 10). To validate experimentally these predictions, the molecule was added to the extracellular medium of primary hippocampal neurons, and its co-localization with the cell membrane marker CellMask was assessed (Figure 11). Following a 5-min incubation period, approximately 53 % of the 2Pyr-2Pyr molecules co-localized with CellMask, covering 3 % of the total membrane (Figure 11B). Interestingly, the same measurements performed 4 days after the pulse incubation revealed that the compound was still present on the membrane (Figure 11B, left), despite the ongoing membrane recycling; accordingly, also the percentage of membrane covered by 2Pyr-2Pyr was not significantly lower than after acute incubation (Figure 116B, right). These observations and the previous results from MD simulations suggest that 2Pyr-2Pyr accumulates in small areas of the membrane and while part of the compound is internalized or diffused over time, some molecules remain stable in these areas. These findings confirm the successful insertion of the molecules into the membrane and

suggests that the coverage of the membrane decreases less over time than observed with Ziapin2 (DiFrancesco et al., 2020).

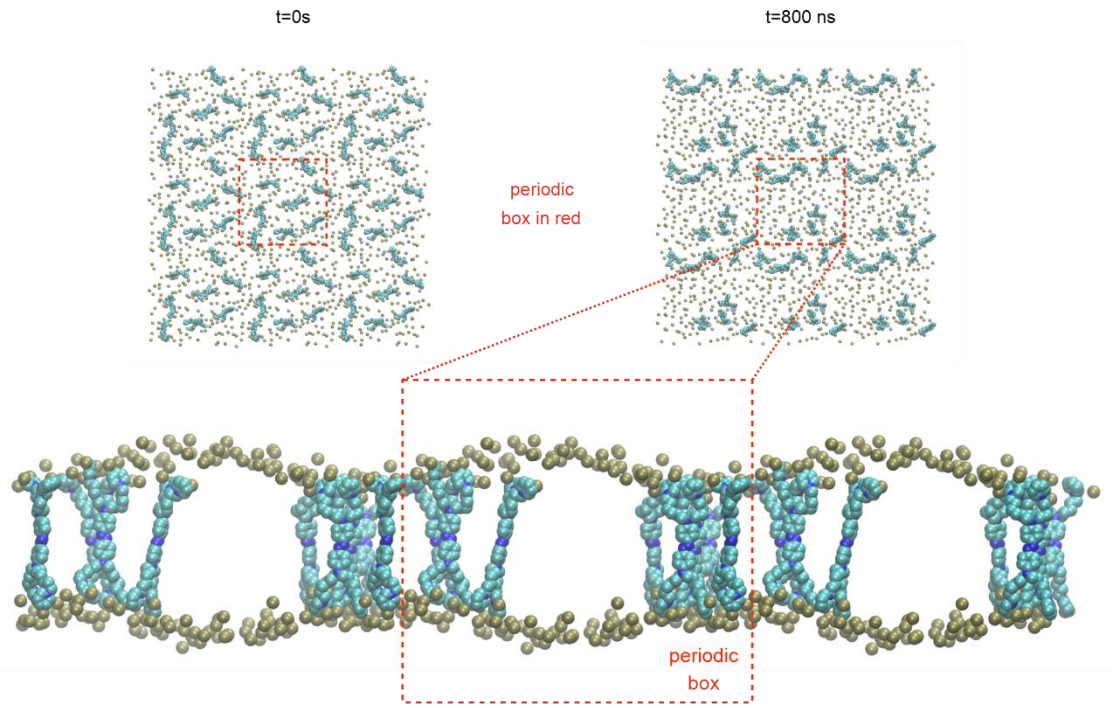

Figure 10 2Pyr-2Pyr tends to aggregate in the dark
Top and side view of the system showing 2P2P (trans) within the membrane (POPC lipid model) replicated along x and y directions, at t = 0 ns and t=800ns. The dashed red box indicates the unit cell of the simulated system.

As MD simulation predicted a localized shrinkage of membrane thickness in the dark, we hypothesized that the light-triggered isomerization of 2Pyr-2Pyr molecules would result in the membrane relaxation, inducing a transient decrease in membrane capacitance. In fact, membrane thickness and membrane capacitance are inversely related since the membrane can be considered analogous to a capacitor. Here, the lipid layers act as the dielectric between two conductive layers (extra- and intra-cellular fluids). Therefore, the parallel plate capacitor model can be applied as follows:

$$C_m = \frac{\varepsilon \cdot A}{d}$$

Where C_m is the membrane capacitance, ε is the membrane permeability, A is the membrane surface, and d is the thickness of the membrane.

To confirm the hypothesized light-induced decrease in membrane capacitance, neurons incubated with either 2Pyr-2Pyr or the vehicle (DMSO, 0.25%) were subjected in the dark and during light stimulation to a hyperpolarizing voltage step in voltage-clamp configuration and the evoked capacitive charge was quantified. The relationship between the membrane capacitance, voltage and capacitive charge can be described by the following equation:

$$C_m = \frac{Q}{V(t)}$$

Where V(t) is the voltage across the membrane as a function of time and Q is the capacitive charge and can be obtained as follows:

$$Q = \int I_{cap}(t)\, dt$$

Being I_{cap} the induced capacitive current.

Indeed, we could observe a significant decrease of membrane capacitance during light stimulation (Figure 11C).

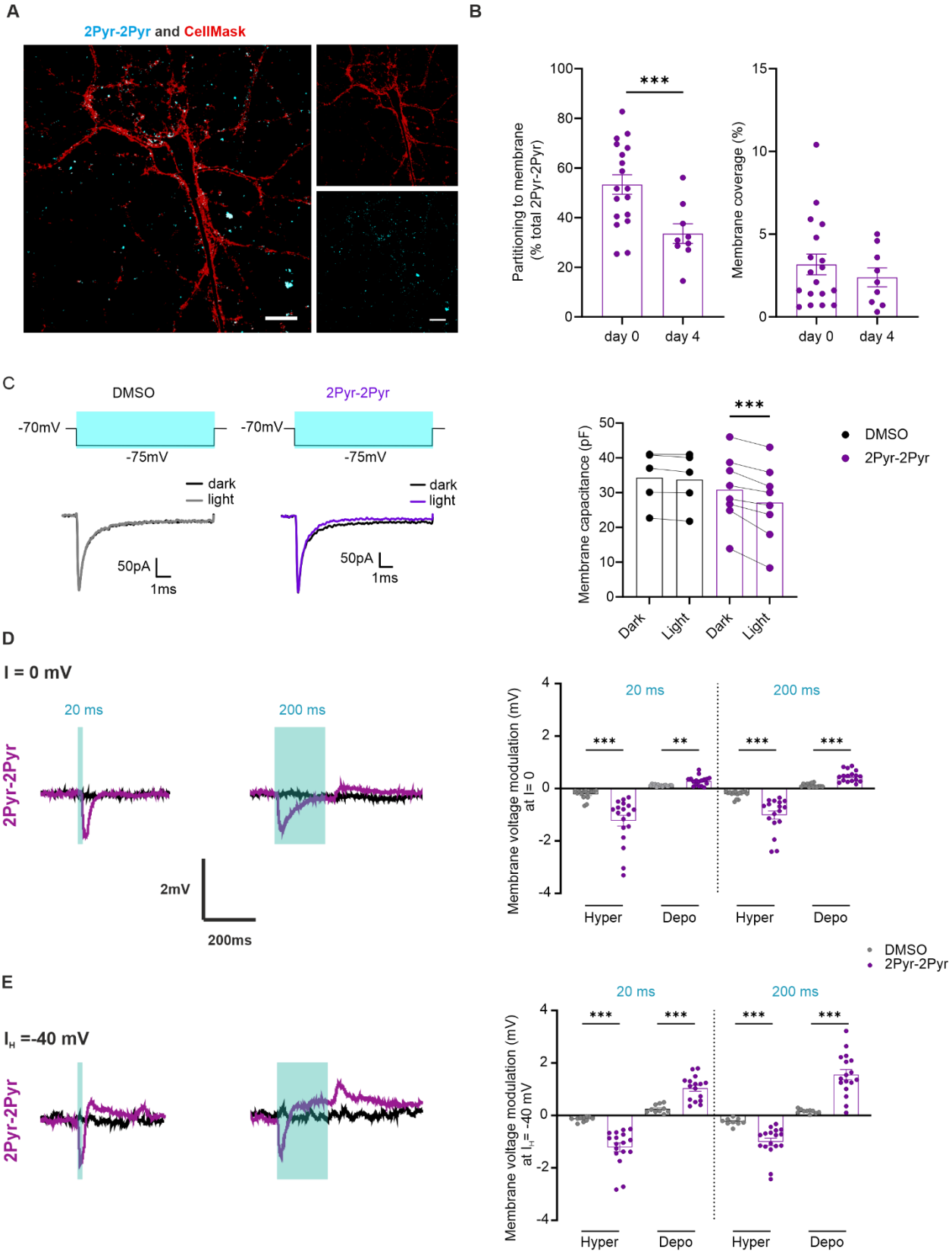
A
2Pyr-2Pyr and CellMask
B
Partitioning to membrane (% total 2Pyr-2Pyr)
***
day 0
day 4
Membrane coverage (%)
day 0
day 4
C
DMSO
2Pyr-2Pyr
-70mV
-75mV
dark
light
50pA
1ms
Membrane capacitance (pF)
***
DMSO
2Pyr-2Pyr
Dark
Light
Dark
Light
D
I = 0 mV
20 ms
200 ms
2Pyr-2Pyr
2mV
200ms
Membrane voltage modulation (mV) at I= 0
20 ms
200 ms
Hyper
Depo
Hyper
Depo
DMSO
2Pyr-2Pyr
E
I_H =-40 mV
2Pyr-2Pyr
Membrane voltage modulation (mV) at I_H= -40 mV
20 ms
200 ms
Hyper
Depo
Hyper
Depo

Figure 11 2Pyr-2Pyr partitions into the neuronal membrane and modulates membrane capacitance and voltage
A. Representative confocal images of primary hippocampal neurons acquired after incubation with 2Pyr-2Pyr (5 µM). Cell membranes are stained with CellMask (red) while 2Pyr-2Pyr is acquired through auto-fluorescence (cyan). Scale bars, 20 µm. **B.** *Left:* Quantification of 2Pyr-2Pyr fraction colocalizing with CellMask at day 0 and 4 after the pulse incubation (% of total compounds fluorescence). *Right*: Quantification of membrane coverage at day 0 and 4 after incubation (% of membrane covered by the compounds) (n= 18 day 0, n= 9 day 4). **C.** *Left:* Representative traces of evoked capacitive currents by applying a hyperpolarizing step (- 5 mV, 10 ms) from a holding potential of – 70 mV in neurons incubated with DMSO or 2Pyr-2Pyr in the dark and during light stimulation. *Right*: Quantification of membrane capacitance modulation in the dark and during light stimulation (n= 5 DMSO, n=8 2Pyr-2Pyr). **D,E.** *Left panels:* Representative traces of membrane voltage modulation upon light stimulation (20 ms or 200 ms light pulses in the cyan spectrum at 20 mW/mm²) recorded in current-clamped neurons at resting membrane potential (**D**) or holding the membrane potential at -40 mV (**E**). Excitatory and inhibitory synaptic blockers were added to the extracellular medium. Neurons were incubated with either vehicle (DMSO, 0.25 %, black traces) or 2Pyr-2Pyr (5 µM, purple traces). *Right panels*: Quantification of the respective light-induced hyper- and depolarization upon 20 ms and 200 ms light stimulation in neurons incubated with either Vehicle or 2Pyr-2Pyr and clamped at resting potential (**D**) or at -40 mV (**E**). (n= 15 DMSO, n=17 2Pyr-2Pyr).
*Statistics: **p>0.01, ***p>0.001; paired t-test (B,C), Kruskal-Wallis test (D,E).*

4.2.2 Light-dependent membrane voltage and firing activity modulation

To assess the light-dependent modulation of membrane voltage by 2Pyr-2Pyr, whole-cell patch-clamp recordings were conducted on primary hippocampal neurons. Neurons were loaded with either 2Pyr-2Pyr (5 µM) or vehicle (DMSO, 0.25 %) in the presence of synaptic blockers to isolate neurons from network activity. Throughout the experiment, neurons were kept in the darkness, and light pulses of 20 and 200 ms in the cyan region of the spectrum (470 nm) were administered to match their peak absorbance. Neurons were either current-clamped at their resting membrane potential (I=0) or at a holding membrane potential of -40 mV (I_H=-40 mV) to examine membrane voltage modulation under and approaching the firing threshold (Figure 11D,E). Incubation with the compound followed by light stimulation resulted in an early hyperpolarization and, in some cases, a delayed depolarization (Figure 11D,E). Interestingly, 2Pyr-2Pyr exhibited a modulation pattern similar to that observed with Ziapin2 (DiFrancesco et al., 2020). The light-induced hyperpolarization was consistent across all experimental conditions, while the depolarization depended on the holding potential and light stimulus duration. Specifically, at resting membrane potential, 2Pyr-2Pyr induced hyperpolarization of approximately 1.23 and 1 mV upon 20 and 200 ms light stimulation, respectively (Figure 11D). At -40 mV, 2Pyr-2Pyr caused a delayed depolarization of around 1 and 1.5 mV (Figure 11E).

To further investigate the light-controlled firing activity, neurons incubated with 2Pyr-2Pyr, Ziapin2 (5 µM), or DMSO (0.25 %) were current-clamped at -40 mV and subjected to a light-train stimulation of 30 20 ms light pulses at 1 Hz (Figure 12A). The light-evoked action potentials were quantified (Figure 12B),

demonstrating that neurons incubated with 2Pyr-2Pyr exhibited light-dependent firing activity similar to those incubated with Ziapin2. These findings indicate that despite having a modified structure compared to Ziapin2, 2Pyr-2Pyr exhibit overall a similar light-dependent modulation pattern of neuronal properties.

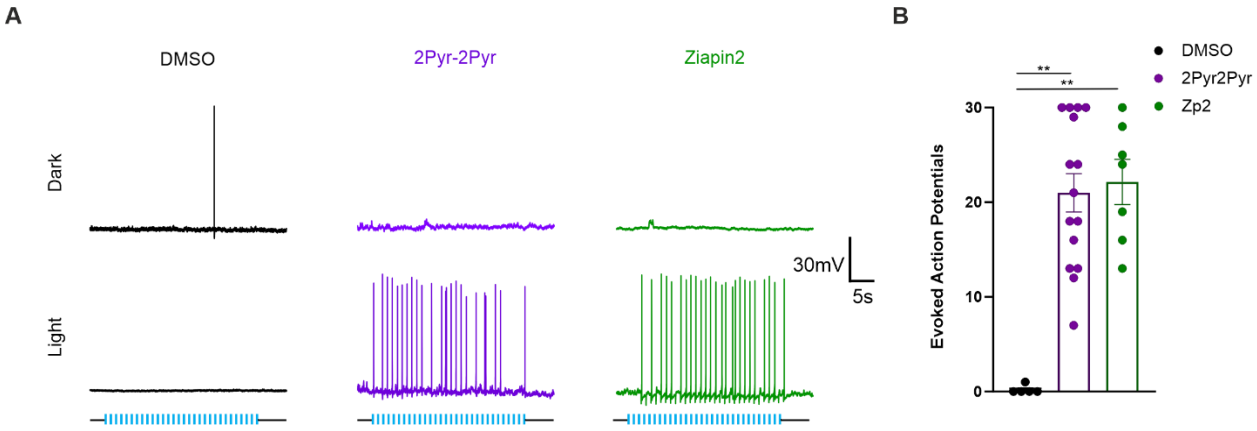

Figure 12 2Pyr-2Pyr induces light-triggered firing
A. Membrane voltage traces recorded in current-clamp configuration holding the membrane potential at -40 mV in neurons incubated with DMSO (0.25 %, black traces), 2Pyr-2Pyr or Ziapin2 (5 µM, purple and green traces, respectively) in the dark or under light-pulse stimulation (1 Hz, 20 ms, 30 light-pulses, 3 mW/mm²). Excitatory and inhibitory transmission were blocked with synaptic blockers. **B.** Quantification of light-evoked action potential firing in the three experimental groups (n= 5 DMSO, 15 2Pyr-2Pyr, 7 Zp2).
*Statistics: **p>0.01; Kruskal-Wallis test (B).*

4.3 Push-Pull

4.3.1 Push-Pull molecules induce a light-dependent depolarization

In an effort to investigate other viable options for a photoswitch, we investigated four distinct synthetic Push-Pull molecules, using a donor-acceptor strategy distinct from the mechanism of Ziapin2 and 2Pyr-2Pyr. Specifically, we replaced the azepane group positioned para to one side of the azobenzene in Ziapin2 with a potent electron-withdrawing group, namely, a nitro group (NO_2), capable of serving as an acceptor in a donor-acceptor system, while keeping the light-dependent isomerization (Figure 13A). This modification led to a red shift in the absorption of the trans-isomer compared to Ziapin2 (Figure 13B).

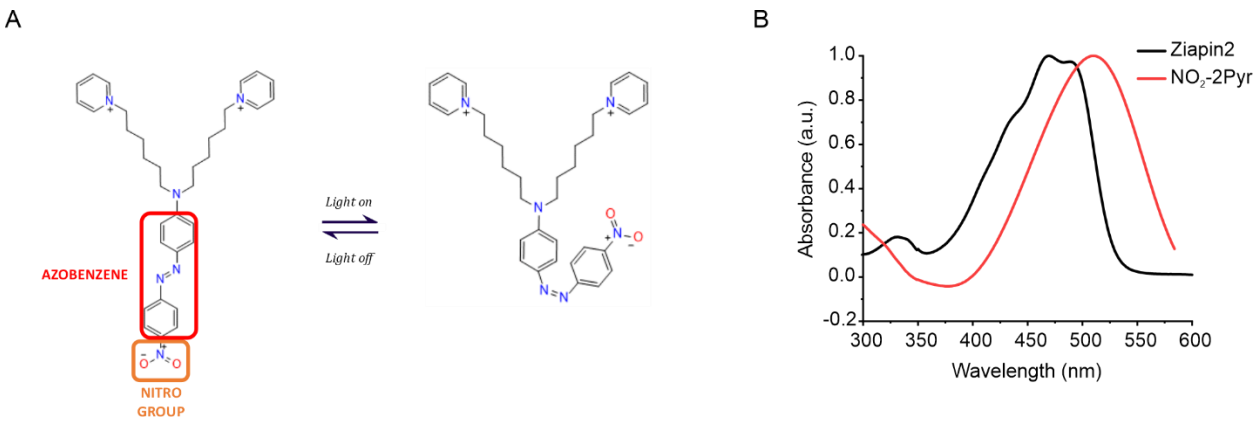

Figure 13 NO_2-2Pyr: a red-shifted donor-acceptor photoswitch
A. Molecular structure of NO2-2Pyr, featuring a Nitro group as a robust electron-withdrawing moiety, facilitating a donor-acceptor mechanism concurrent with light-induced isomerization. **B.** Red shift in absorbance for NO_2-2Pyr in comparison to Ziapin2.

The four studied Push-Pull molecules vary only in the number of polar branches on one side of the azobenzene core, either one or two branches, and the terminal polar group, Pyridine or Ammonium (Figure 14). The quantity of polar branches and the specific terminal functional group can impact hydrophilicity, solubility, and interactions with the lipid bilayer, consequently influencing the photoswitch response to light. Notably, the Pyridine group, as a heterocyclic aromatic compound, may introduce distinct electronic and steric effects, while the Ammonium group, as a positively charged moiety, has the potential to introduce electrostatic interactions with the negatively charged components of the lipid bilayer. The investigated Push-Pull molecules exhibit two resonance structures: a neutral configuration and a zwitterionic one. The zwitterionic state possess a net positive charge on the amine group and a net negative charge on the nitro group. We anticipated that this peculiar structure should allow a substantial dipole moment variation during photoisomerization, inducing a change in the polarization of the cell membrane. This change, we hypothesized, might not only facilitate neuronal firing through mechanical strain, but also via electrical stimulation.

To examine the spontaneous integration of Push-Pull compounds into the cellular membrane, we conducted five independent 1 µs-long MD simulations. During these simulations, we placed a single NO_2-2Pyr molecule in the dark state at random orientations within bulk water, proximate to a 1-palmitoyl-2-oleoyl-phosphatidylcholine (POPC) double-layer. In all instances, NO_2-2Pyr partitioned into the bilayer within 500 ns, initially inserting the side containing the nitro-group, and remained embedded in the membrane throughout the simulation trajectory (Figure 14B). The primary axis of the molecule aligned nearly parallel to the bilayer's normal (Figure 14B). MD simulations did not indicate any interactions between photoswitches present on the opposing leaflets, resulting in no discernible modulation of the membrane thickness (Figure 14C). An analysis of molecular thickness revealed no observable changes upon integration of the molecules (Figure 14D).

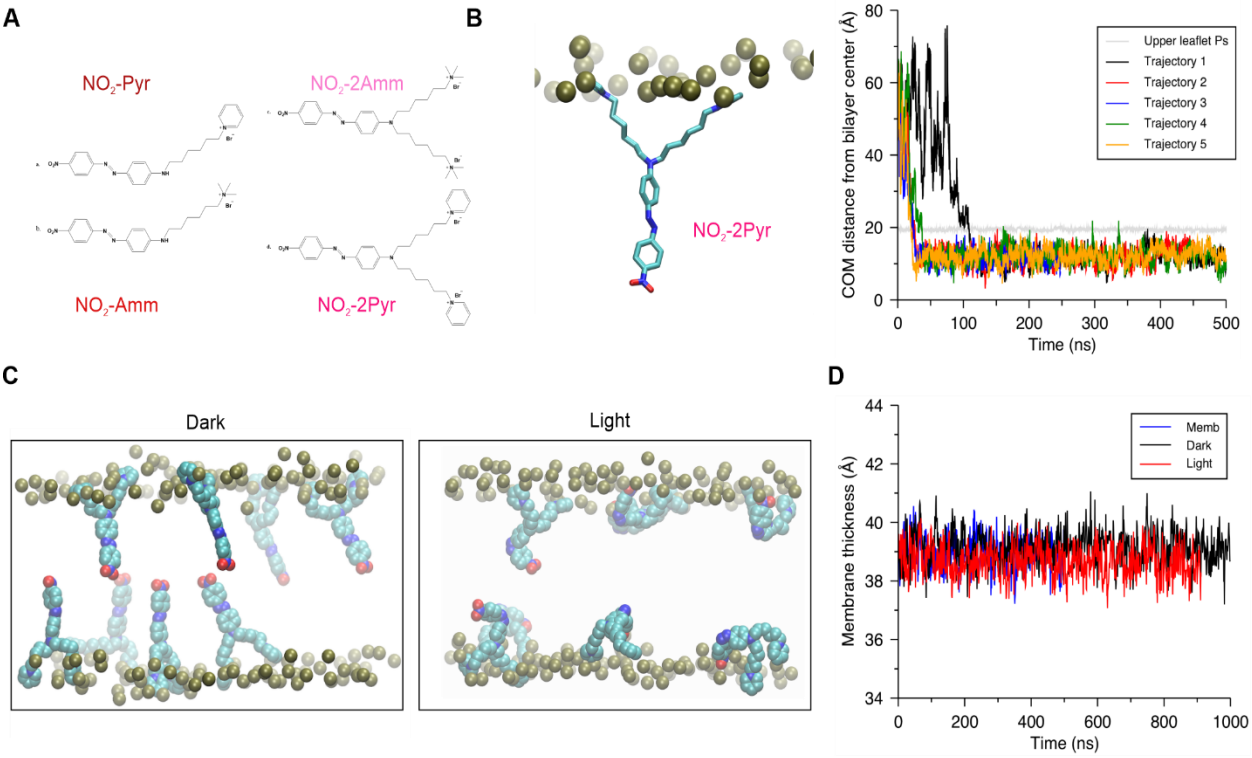

Figure 14 NO_2-2Pyr partitions spontaneously into the lipid bilayer
A. Molecular structure of NO_2-2Pyr and its light-triggered isomerization. **B.** *Left:* Snapshot extracted from an MD simulation showing NO_2-2Pyr (trans) embedded into the membrane (POPC lipid model); lipid phosphate atoms are shown as tan spheres; water molecules and acyl chains are not reported for clarity. *Right:* Time-dependence of the distance between the center of mass (COM) of NO_2-2Pyr and the bilayer center, in five independent trajectories; the grey line is the average position of the upper leaflet lipid head groups. **C.** Snapshot extracted from an MD simulation showing 8 molecules of NO_2-2Pyr (trans and cis) embedded in the membrane (POPC lipid model); lipid phosphate atoms are shown as tan spheres; water molecules and acyl chains are not reported for clarity. **D.** The average membrane thickness under dark and light conditions does not change along the trajectories.

Before studying the effect induced by light stimulation upon insertion of the Push-Pull molecules into the cell membrane, we assessed their biocompatibility. Primary hippocampal neurons incubated either with the various photoswitches (5 µM) or their vehicle (0.25 % DMSO) were subjected to propidium iodide staining. Neurons loaded with molecules exhibited no significant difference in viability compared to those loaded with vehicle alone (Figure 15A). Confocal imaging was conducted to confirm the partitioning of all molecules into the neuronal membrane; however, their detection was unsuccessful when stimulated at their peak absorbance (data not shown). This is likely due to the complete utilization of absorbed energy for intra-molecular electron transfer without any fluorescence emission. Nonetheless, patch-clamp experiments in whole-cell configuration were performed, in which primary neurons loaded with the different molecules were stimulated with 20 and 200 ms light pulses in the cyan region of the spectrum (470 nm) and the membrane voltage modulation was recorded within a 300 ms time window from light onset. The representative traces reported in Figure 15C reveal that all molecules induce a transient depolarization. Notably, molecules with two polar branches caused approximately 1 mV depolarization, while those with a single branch induced an average depolarization of 1.5 mV (Figure 15D). Although no differences in amplitude of the evoked depolarization were observed between the two stimulation times, a rebound hyperpolarization was evident after the 200 ms stimulation, likely due to the long-lasting depolarization during light stimulation. Additional experiments aimed at studying the possibility to induce light-dependent firing activity did not exhibit any differences compared to neurons loaded with the Vehicle, suggesting that the induced depolarization is insufficient to trigger action potentials (data not shown).

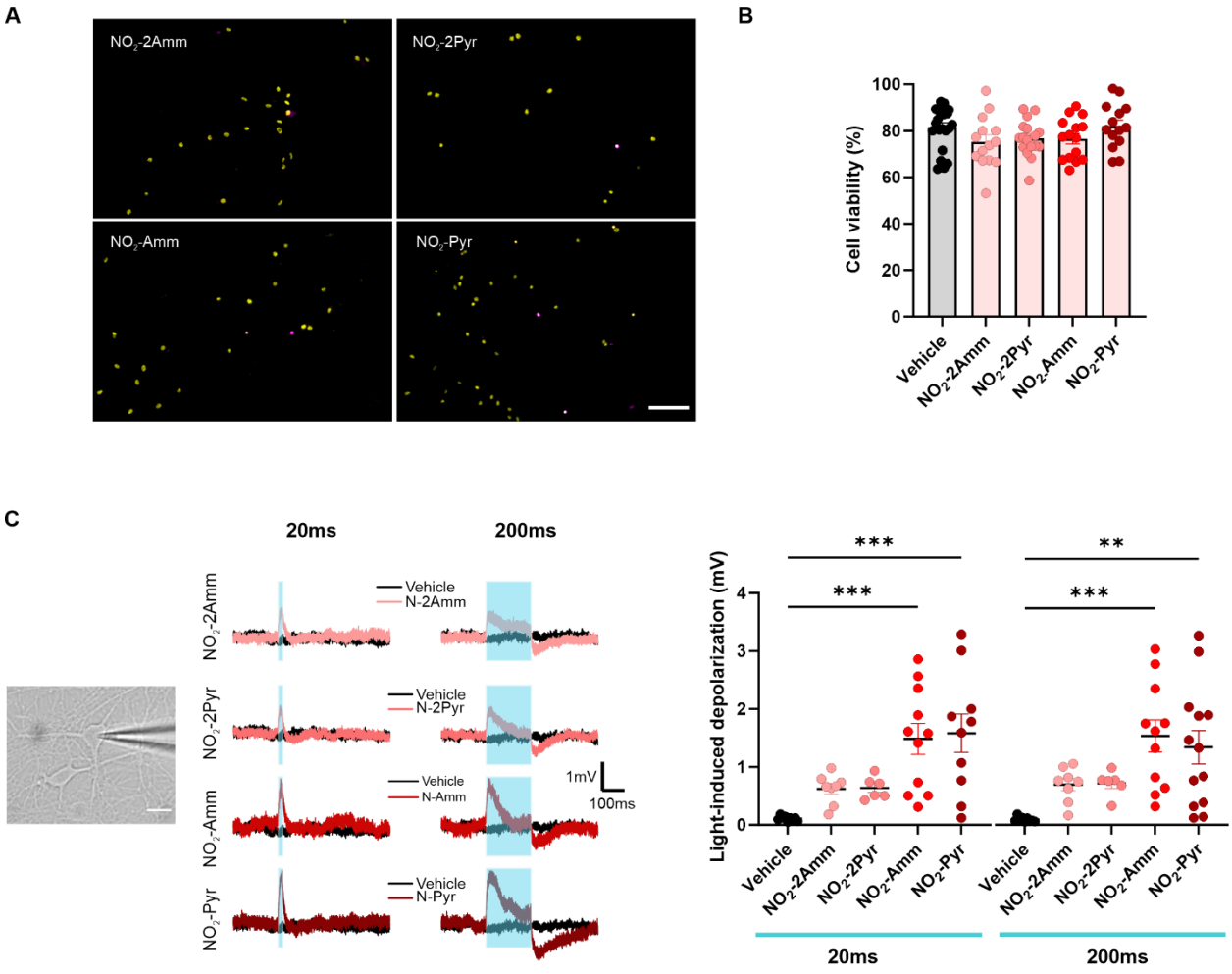

Figure 15 Light-induced depolarization in primary hippocampal neurons

A. Representative images of viability test on primary hippocampal neurons incubated with each Push-pull molecule (5 µM) or Vehicle thereof (DMSO, 0.25 %). All cells are stained with Hoechst (yellow) and apoptotic cells with propidium iodide (purple). Scale bar, 100 µm. **B.** Viability after incubation with either Vehicle (DMSO, 0.25%) or the different Push-pull molecules (5 µM). Viability ratio is expressed as: (all cells -propidium iodide-positive cells)/all cells x 100) (n= 24 Vehicle, n=14 NO_2-2Amm, n=17 NO_2-2Pyr, n=15 NO_2-Amm, n=14 NO_2-Pyr). **C**. *Left:* Representative image of whole-cell patch clamp on primary hippocampal neurons (upper panel). Scale bar, 20 µm. *Right:* Representative traces of membrane voltage modulation upon light stimulation (20 ms or 200 ms light pulses in the cyan spectrum at 20 mW/mm²) recorded in current-clamped neurons at resting membrane potential. Excitatory and inhibitory synaptic blockers were added to the extracellular medium. **D.** Quantification of light-induced depolarization upon 20 ms and 200 ms light stimuli in neurons incubated with vehicle or the different molecules (n= 9 vehicle, n=8 NO_2-2Amm, n=6 NO_2-2Pyr, n=11 NO_2-Amm, n=13 NO_2-Pyr).

*Statistics: D) One-way ANOVA (Push-pulls vs. Vehicle). **p<0.005, ***p<0.0005.*

4.4 BV-1

We also characterized a different Donor-Acceptor photoswitch, named BV-1 that shares a similar amphipathic structure with previously presented photoswitches allowing it to spontaneously partition into the plasma membrane. BV-1 responds to light but differs from the previously studied photoswitches as it lacks the azobenzene core. The structural arrangement of BV-1 is shown in in Figure 16A. BV-1 is a closed-shell di-cation compound that possesses positively charged alkyl-ammonium and N-alkyl-pyridinium groups. The molecule features an electron-deficient pyridinium block connected to an electron-rich terthiophene block via a conjugated trans double bond, resulting in a large and planar optimized structure. The electronic properties of BV-1, characterized by a HOMO orbital predominantly localized on the terthiophene block and a LUMO orbital centered on the pyridinium cation, contribute to its optical properties. The calculated absorption spectrum of BV-1 shows a dominant S0→S1 transition in the visible range, primarily attributable (94%) to a single particle HOMO-LUMO excitation with a peak at 478 nm, which is consistent with the experimentally measured spectra (Figure 16A). The charge density difference between the ground state S0 and the excited S1 state, as depicted in Figure 16A, indicates a charge-transfer nature of S1 with a depletion of charge from the thiophene units and an accumulation of charge predominantly on the pyridinium ring (blue and red regions, respectively). By comparing the absorption and emission spectra of BV-1 in water and detergent (sodium dodecylsulfate, SDS) micelles mimicking the membrane environment, a blue shift of approximately 50 nm in BV-1 emission accompanied by an increase in emission quantum yield in SDS is observed. This suggests that BV-1 may spontaneously partition into the plasma membrane due to its amphiphilic properties.

To investigate the spontaneous insertion of BV-1 into the membrane, we conducted five independent 1 μs-long MD simulations, placing one BV-1 molecule in the dark state at random orientations in bulk water near a 1-palmitoyl-2-oleoyl-phosphatidylcholine (POPC) double-layer. In all simulations, BV-1 entered the bilayer within 500 ns by first inserting the side containing thiophene groups, and remained in the membrane for the remainder of the trajectory. The molecule's main axis aligned almost parallel to the bilayer normal (Figure 16B). In this stable conformation, the positively charged alkyl-ammonium group resided near the phospholipid heads, interacting with the phospholipid phosphate groups.

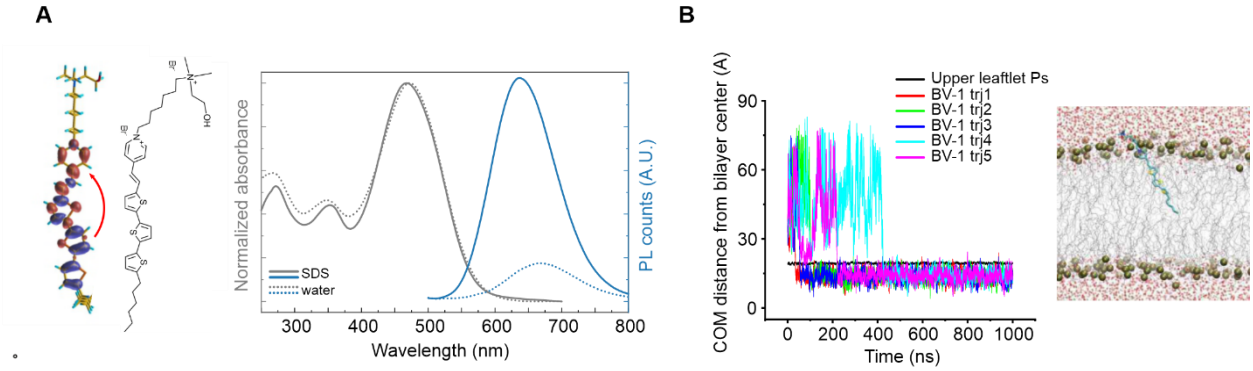

Figure 16 Chemical structure and Molecular Dynamics simulations of BV-1 insertion into the lipid bilayer
A. *Left:* Chemical structure of BV-1 and BV-1 optimized geometry with charge density displacement between ground and the first excited state. Blue and red regions indicate charge depletion and accumulation, respectively, upon excitation. *Right:* BV-1 (25 µM) absorbance and photoluminescence spectra in sodium dodecylsulfate (0.1 µM) and water. **B.** MD simulations of BV-1 insertion into the lipid bilayer: snapshot of the membrane-inserted BV-1 (*left*) and insertion dynamics (*right*).

4.4.1 BV-1 spontaneously partitions into lipid bilayer and induces a sustained depolarization

To validate the predicted spontaneous insertion of BV-1 into the cellular membrane, BV-1 was loaded into the extracellular medium of primary hippocampal neurons, and its co-localization with the cell membrane marker CellMask was examined over time (Figure 17A,B). Following a 5-min incubation period, approximately 80 % of the BV-1 molecules co-localized with CellMask, confirming the predictions from MD simulations. Interestingly, differently from the previous studied molecules, BV-1 seems to partition homogeneously over the whole membrane, covering on average 60 % of the cell surface, without assuming a spotted pattern (Figure 17C, left panel). Subsequently, the compound displayed time-dependent internalization over several days, with a progressive decrease in surface localization (~52 % at day 4 compared to day 0; Figure 17C, right panels) in line with the physiological membrane turnover.

To investigate the impact of BV-1 on neuronal physiology, whole-cell patch-clamp recordings were performed on primary hippocampal neurons loaded with BV-1 and either kept in the dark or subjected to light pulses at 470 nm, corresponding to the peak absorbance of BV-1 (Figure 17D). Upon 20- or 200-ms light pulses (3 mW/mm^2) administered at 0.25 Hz, a stepwise depolarization was observed after each

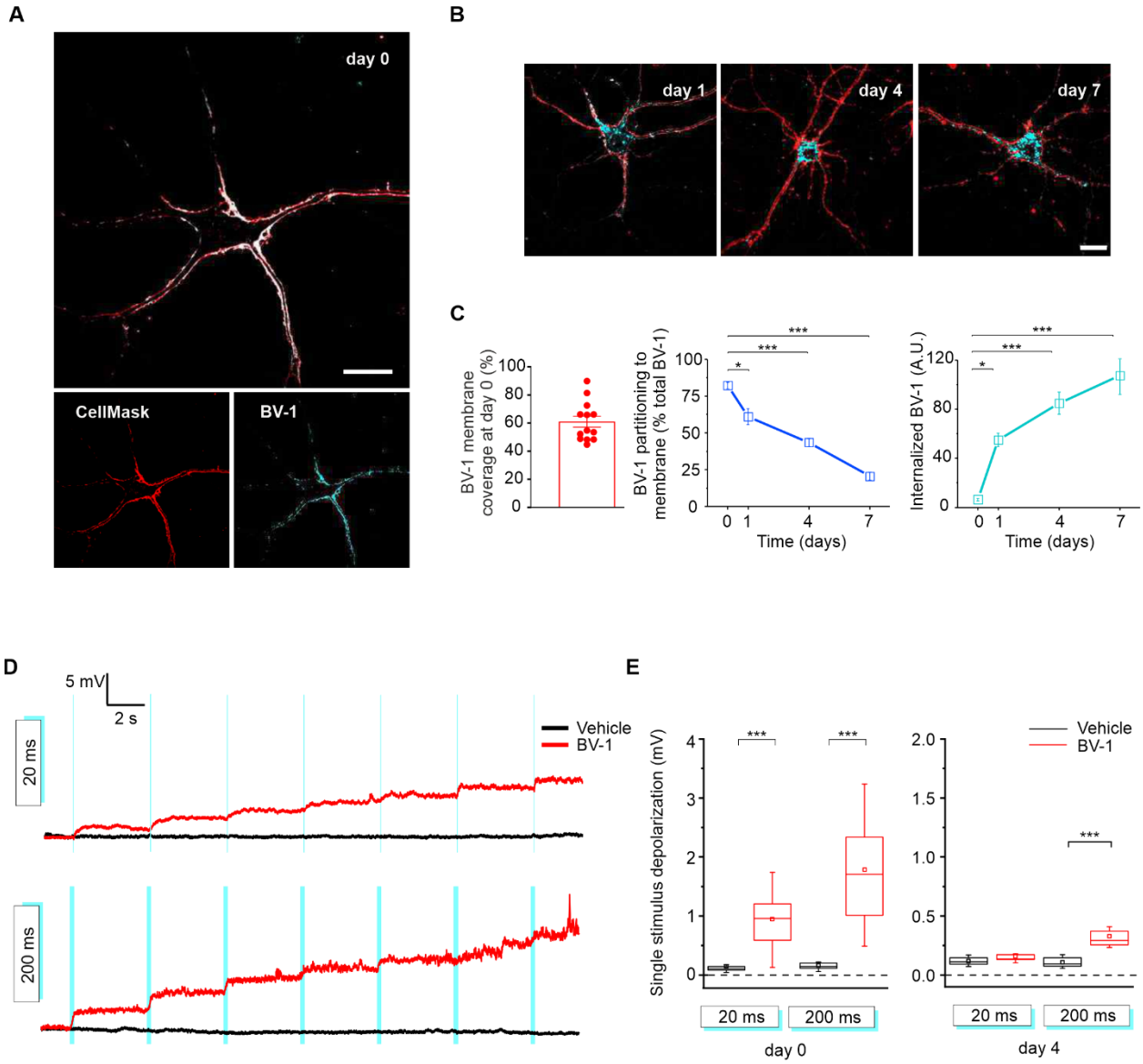

Figure 17 Time-dependent internalization of BV-1 and membrane voltage modulation

A. Representative confocal images of primary hippocampal neurons acquired after incubation with BV-1 (1 µM). Cell membrane stained with CellMask (red) and BV-1 acquired through auto-fluorescence (cyan). Scale bars, 20 µM. **B.** Confocal images at day 1,4 and 7 after incubation with BV-1. Scale bar, 20 µM. **C.** *Left:* Quantification of BV-1 fraction colocalizing with CellMask (% of total BV-1 fluorescence) (n= 14 day 0, 12 day 1, 16 day 4, 9 day 7). *Right:* Quantification of the BV-1 amount on the membrane and its time-dependent internalization (n= 6 day 0, 15 day 1, 16 day 4, 6 day 7) (right panel). **D.** Membrane voltage traces recorded in current-clamp (CC, I= 0 pA) primary hippocampal neurons. Cells were incubated with either vehicle (H_2O, 0.1 %, black traces) or BV-1 (1 µM, red traces) and light-stimulated with 7 subsequent pulses in the cyan region of the spectrum (470 ± 10 nm) at 3 mV/mm² for 20 ms (upper traces) or 200 ms (lower traces). Recordings were performed at day 0 and day 4 after incubation in presence of excitatory and inhibitory synaptic blockers. **E.** Single stimulus depolarization calculated in a 300 ms window from light onset, quantified from neurons at day 0 (*left*) and 4 (*right*) after initial incubation with either vehicle or BV-1 (day 0: n=13 vehicle, n=16 BV-1; day 4: n= 8 vehicle, n=13 BV-1).

*Statistics: E. Kruskal-Wallis multiple comparison (day 0 vs. day 1/4/7). G. Unpaired t-test and Mann-Whitney test (Vehicle vs. BV-1). *(p<0.05), ***(p<0.001).*

stimulus, demonstrating the correlation between light stimulus duration and magnitude of depolarization (Figure 17E, left panel). Four days after incubation, a smaller but still significant depolarization was observed in response to 200 ms light stimulation, whereas no significant responses were detected with 20-ms pulses (Figure 17E, right panel). The reduced effectiveness over time, starting from the initial pulse administration of BV-1, aligns with the progressive decrease in plasma membrane BV-1 levels due to membrane trafficking and internalization (Figure 17). The proportionally smaller depolarization at day 4 (19 % depolarization compared to day 0) relative to the decrease in membrane BV-1 concentration suggests that the light-dependent effect may arise from cooperative interactions among multiple BV-1 molecules.

4.4.2 Light-dependent formation of pores in the lipid bilayer by BV-1

To elucidate the mechanism underlying light-dependent modulation of the membrane potential, we examined the impact of light stimulation on BV-1-loaded membranes. We performed two independent simulations, each lasting 2 µs, involving eight BV-1 molecules either in the dark or in the light-stimulated state. The simulations took place within a 1:1 POPC:cholesterol bilayer. Our results revealed that BV-1 molecules remained separate in the dark state but tended to form aggregates following light stimulation (Figure 19A). This was evident from the distinct radial distribution functions of the sulfur atoms in the central thiophene rings, showing no features for the molecules in the dark state, but a clear peak at approximately 5 Å for the excited molecules (Figure 19A, left). Snapshots extracted from the end of the dark and light-stimulated simulations demonstrated the formation of aggregates only in the latter case (Figure 19A, right).

To examine the consequences of light-dependent BV-1 aggregation within the cell membrane, BV-1 was added to mica-supported POPC:cholesterol (1:1) bilayers. A single light stimulus was applied, and the membrane was imaged using high-speed atomic force microscopy (HS-AFM; Figure 19B). We observed irreversible lipid fusion and a significant reduction in membrane thickness upon light stimulation, as evidenced by cross-sectional analysis along the dashed lines (Figure 19B, bottom). Time-lapse AFM analysis of the membrane patch height above the mica plane revealed a clear reduction upon light stimulation (Figure 19C). Notably, there was a significant change in the height distribution between t1 = 126 s (black trace) and t5 = 932 s (blue trace), corresponding to a decrease in bilayer height from 4.9 to 4.1 nm, respectively (Figure 19D). Further examination of the membrane morphology using HS-AFM imaging at the lipid bilayer plane revealed the formation of nanometric membrane depressions,

consistent with the presence of BV-1-induced membrane pores upon light stimulation (Figure 19E). These pores led to an irreversible increase in membrane roughness from approximately 0.12 to 0.17 nm upon illumination (Figure 19F). Our findings were corroborated by patch-clamp experiments conducted on primary neurons in the cell-attached configuration. Neurons treated with BV-1 exhibited extra-large pore-opening events upon light stimulation, which were superimposed to physiological K^+ single-channel currents (Figure 18).

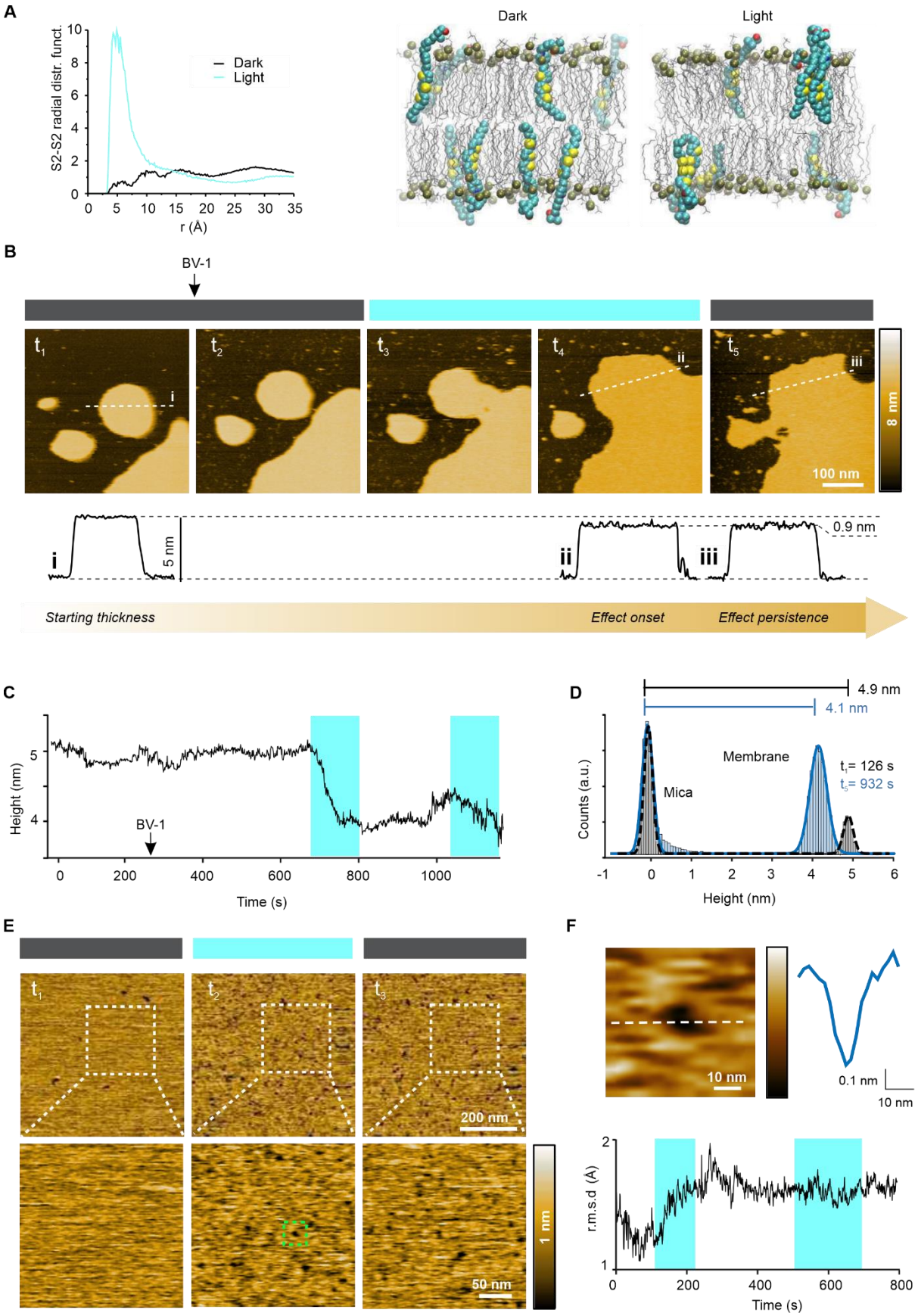
A
S2-S2 radial distr. funct.
r (Å)
Dark
Light
Dark
Light
B
BV-1
t1
t2
t3
t4
t5
i
ii
iii
8 nm
100 nm
5 nm
0.9 nm
Starting thickness
Effect onset
Effect persistence
C
Height (nm)
BV-1
Time (s)
D
4.9 nm
4.1 nm
Membrane
Mica
t1= 126 s
t2= 932 s
Counts (a.u.)
Height (nm)
E
200 nm
50 nm
1 nm
F
10 nm
0.1 nm
10 nm
r.m.s.d (Å)
Time (s)

Figure 19 BV-1 triggers thinning and formation of pores in planar lipid bilayers

A. *Left:* Radial distribution function of the central thiophene sulfur atoms (S2) calculated from 2 µs long MD simulations of eight dark (black line) or light-stimulated (blue line) BV-1 within the membrane. *Right:* Snapshot from the simulation of BV-1 in the dark and after light stimulation. **B.** Time-resolved AFM topographies of POPC:Chol=1:1 (mol:mol) mica-supported membranes dynamics imaged at 1 frame per seconds at 5 representative time points of the experimental protocol (t_1 = 126 s, t_2 = 667 s, t_3 = 688 s, t_4, 791 s, t_5 = 932 s). BV-1 was added in the fluid chamber at a final concentration of ~50 µM and allowed to partition into the bilayer for ~7 min. HS-AFM recordings captured irreversible lipid fusion and reduction in membrane thickness upon cyan-light irradiation, as documented by cross-sectional analysis along the dashed lines (i-iii, lower panels). **C.** Time-lapse analysis of the height of the membrane patches above the mica plane. Each data point is the difference between the means of the height distribution of the membrane- and the mica-associated Gaussian components (see panel D). **D.** Height distributions of the bilayers shown at t_1 (black) and t_5 (blue). For both times, the distributions segregate into two well-resolved peaks separating mica and lipid bilayer height distributions. The two peaks were fitted with the sum of two Gaussian functions. A ~0.8 nm reduction in membrane thickness was observed upon illumination. **E.** Time-resolved topographies of POPC:Chol=1:1 (mol:mol) planar membrane imaged at 1 frame per second at 3 representative time points of the experimental protocol (t_1 = 45 s, t_2 = 211 s, t_3 = 434 s) in the presence of 50 µM BV-1 (incubated for about 15 min prior to imaging). HS-AFM recording captured the dynamic formation of nanometric membrane depressions or pores upon cyan-light irradiation, only resolved upon tight contrast adjustment on the membrane plane. Enlargements of the white boxed area highlighting the dynamic membrane defects are shown at the bottom of each corresponding frame. **F.** Zoom-in of the depression of BV-1-treated bilayer highlighted in panel E (green box), and corresponding depth profile (*top*). Time-lapse analysis of the membrane surface roughness defined as the bilayer r.m.s.d. (*bottom*). Pore formation results in irreversible increase of membrane roughness from ~0.12 to ~0.17 nm upon illumination.

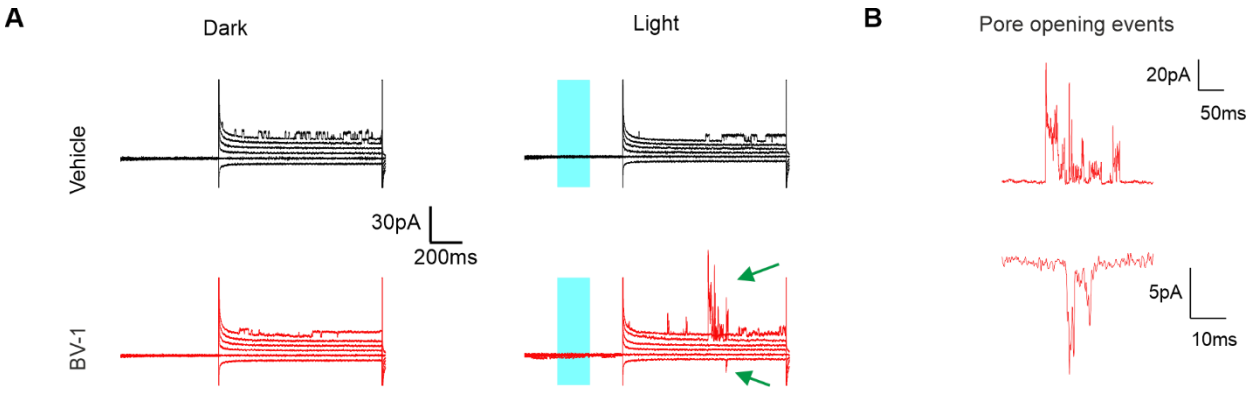

Figure 18 Light-triggered pore generation by BV-1

Measurements were performed on neurons in cell-attached configuration with Vehicle (H_2O; 0.1 % v/v) or BV-1 (0.1 µM) in the pipette filled with Tyrode external solution. Current traces were recorded with 40 mV voltage steps in the absence of light stimulation (Dark), and after 12 light pulses (200 ms at 3 mW/mm^2, 0.5 Hz). Arrows indicate extra-large pore opening events highlighted in the right panel.

4.4.3 Light stimulation induces changes in the passive membrane properties and Na^+ inward currents in BV-1 treated neurons

To explore the impact of light stimulation on BV-1 treated neurons, we first assessed changes in membrane resistance through a series of light pulse stimulations. Using inward current ramps below the neuronal firing threshold, we measured the resulting voltage slope to calculate membrane resistance (R) using the Ohm's Law, which correlates the voltage change (ΔV) to the injected current (ΔI). Our observations revealed that membrane resistance remained unaltered in the absence of light.

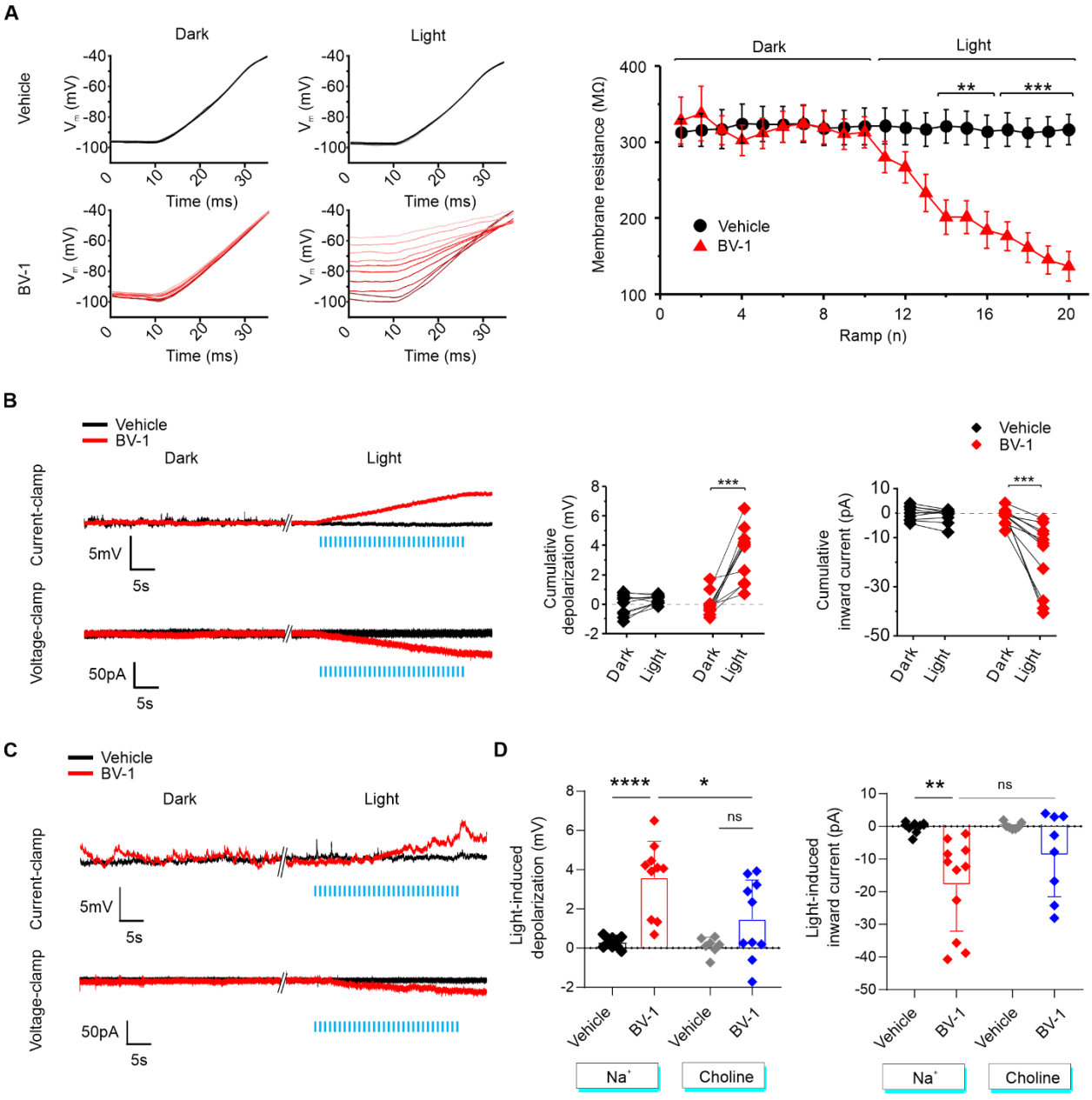

Figure 20 Light-dependent modulation of the passive electrophysiological properties by BV-1
A. *Left:* Membrane voltage traces recorded with 10 current-clamp ramps applied at 2 Hz, driving the membrane voltage from -95 mV to -40 mV in 20 ms in the dark and upon light stimulation (200 ms, 3 mW/mm²) from neurons incubated with either Vehicle (H_2O, 0.1 %) or BV-1 (1 µM). *Right*: Membrane resistance calculated from the slope of the recorded voltage traces during 10 ramps in the dark and 10 ramps under light stimulation (n = 7 and 8 for Vehicle and BV-1, respectively). **B.** *Left:* Representative membrane voltage traces recorded in current-clamp configuration by holding the membrane voltage of primary hippocampal neurons at -70 mV (upper traces). Corresponding current traces recorded in the voltage-clamp configuration by clamping the voltage at -70 mV (lower traces). Cells were incubated with either Vehicle (H_2O, 0.1 %, black traces) or BV-1 (1 µM, red traces) and measurements were performed either in the dark or under light-train stimulation (1 Hz, 20 ms, 30 light-pulses, 3 mW/mm²) in the presence of synaptic blockers and tetrodotoxin (TTX; 1 µM). *Right*: Cumulative membrane depolarization and inward current intensity (I) modulation calculated at the end of the 40 s recorded sweeps (n = 10 and n=11 for Vehicle and BV-1, respectively). **C.** *Left:* Na^+ in the external medium was replaced with choline (135 mM). Representative membrane voltage traces recorded in current-clamp configuration by holding the membrane voltage at -70 mV (upper traces) and corresponding current traces recorded in the voltage-clamp configuration by clamping the voltage at -70 mV (lower traces). Cells were incubated with either Vehicle (black traces) or BV-1 (1 µM; red traces) and measurements were performed in the dark and under light-pulse stimulation (1 Hz, 20 ms, 30 light-pulses, 3 mW/mm²) in the presence of synaptic blockers and TTX (1 µM) in the extracellular medium. *Right*: Comparison of the cumulative light-induced depolarization and inward current in presence of either Na^+ or choline in the extracellular medium (n = 10, 11, 7, 9 for Vehicle/Na^+, BV-1/Na^+, Vehicle/Choline and BV-1/Choline, respectively).
*Statistics: *p<0.05, **p<0.01, ***p<0.001; two-way ANOVA/Šídák's tests (A,C); Wilcoxon's test (B).*

However, with successive cycles of light stimulation, the membrane resistance progressively decreased (Figure 20. A), consistent with the light-dependent opening of membrane pores observed in lipid bilayers.

To further characterize the light-dependent membrane depolarization, we focused on the modulation of subthreshold neuronal properties. Neurons incubated with BV-1 were current-clamped at a holding membrane voltage of -70 mV in the presence of synaptic transmission blockers, tetrodotoxin (TTX) to inhibit voltage-dependent Na^+ channels and action potential firing. Upon stimulation with a 30-s train of light pulses, these neurons experienced a cumulative depolarization of 3.5 ± 0.5 mV accompanied by an evoked inward current of -17.8 ± 4.3 pA compared to the vehicle control (-0.03 ± 0.22 mV and -1.2 ± 0.9 pA, respectively) (Figure 20B).

To determine if the light-evoked inward current involved Na^+ ions, we repeated the experimental protocol with external Na^+ replaced by an equal concentration of choline. Under these conditions, both the light-evoked depolarization and the inward current were significantly reduced (Figure 20C), supporting the involvement of Na^+ influx in mediating the effects of photostimulation.

To assess the possible reversibility of the progressive light-induced depolarization, we decreased the concentration of BV-1 to 0.1 µM and varied the duration of light pulses. At this lower BV-1 concentration, depolarization became significant for pulses of 100 ms or longer and was proportional to the duration of light stimuli (Figure 21A). However, the membrane voltage failed to return to basal levels at the end of

the 8-s protocol, indicating substantial irreversibility of the light-triggered membrane depolarization (Figure 21B).

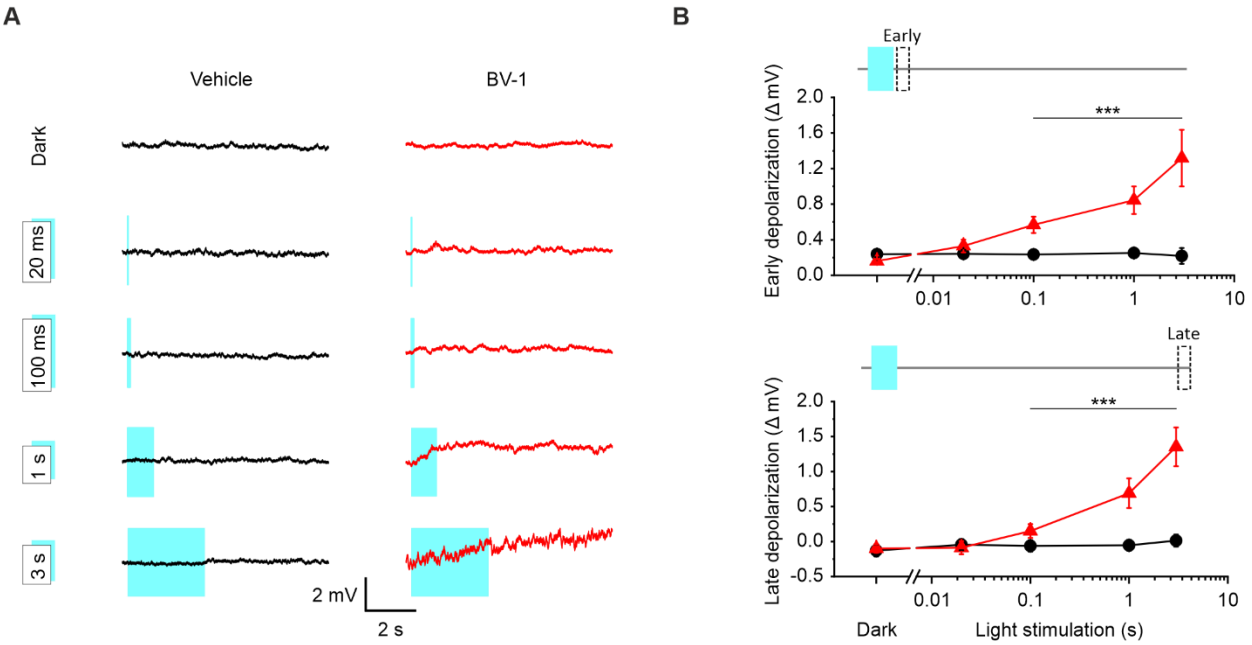

Figure 21 The light-induced membrane depolarization induced by BV-1 is not reversible
Left: Membrane voltage traces (8 s) recorded in current-clamp configuration (I_h = 0 pA) from primary hippocampal neurons incubated with either Vehicle (H_2O) or BV-1 (0.1 µM) in the presence of synaptic blockers and kept in the dark or subjected to cyan light stimuli of increasing duration (20 ms, 100 ms, 1 s, 3 s) at 3 mW/mm². *Right*: Depolarization peak calculated in a time-window of 300 ms from light offset, or from 200 to 500 ms when exposed to dark (Early depolarization, upper panel). Late membrane voltage calculated in the last 300 ms of the 8 s recorded trace (Late depolarization, lower graph) (n = 14 and 11 for Vehicle and BV-1).
*Statistics: ***p<0.001; two-way ANOVA/Šídák's tests.*

4.4.4 Alteration of action potential firing in BV-1 treated neurons upon light stimulation

To evaluate the potential modulation of neuronal firing, we performed current-clamp recordings on neurons incubated with BV-1. The membrane voltage was held at subthreshold levels (-40 mV) in the presence of synaptic blockers. In the dark, both vehicle-treated and BV-1-loaded neurons displayed similar spontaneous firing activity (Figure 22A). However, only BV-1-loaded neurons responded to a train of light stimuli with a progressive depolarization, leading to a significant increase in AP firing when TTX was absent (Figure 22B). Interestingly, the AP waveform underwent progressive changes during the light train. Phase-plane plot analysis was employed to quantitatively examine the light-induced alterations in AP shape,

comparing recordings in the dark with three time points during the light stimulation protocol (Figure 22C). Following a few stimulation pulses, the AP duration increased, and along the stimulation protocol, the AP waveform exhibited an after-spike plateau slightly below 0 mV, often accompanied by repetitive spikelets. Although individual neurons displayed different dynamics, virtually all BV-1-treated cells showed a clear and progressive increase in AP half-width, with noticeable slowdowns in both rising and repolarizing slopes, as well as a decreased AP peak amplitude at the end of the light train stimulation (Figure 22D).

To investigate the underlying mechanisms, which involve voltage-dependent Na^+ and K^+ currents, we examined the modulation of their conductances under illumination. Patch-clamp recordings in the voltage-clamp configuration were performed on vehicle- and BV-1-treated neurons under conditions to isolate Na^+ and K^+ currents. BV-1-loaded neurons subjected to light stimulation exhibited a significant increase in the time constant of current decay (Figure 23A). Analysis of the current-voltage (I/V) relationship in BV-1-treated neurons revealed a slight, but consistent, decrease in Na^+ current amplitude in the voltage range of -10 to +20 mV upon light stimulation, while the I/V curve of vehicle-treated neurons remained unchanged (Figure 23B).

When investigating K^+ currents, BV-1-loaded neurons demonstrated a significant decrease in K^+ current amplitude in response to light stimulation (Figure 23C). The I/V relationship in BV-1-treated neurons displayed a light-dependent decrease in current amplitude across the entire voltage range upon light stimulation, whereas vehicle-treated neurons showed no response to light pulses (Figure 23D). These observations align with the pronounced and progressive changes in AP shape observed during repetitive light stimulation.

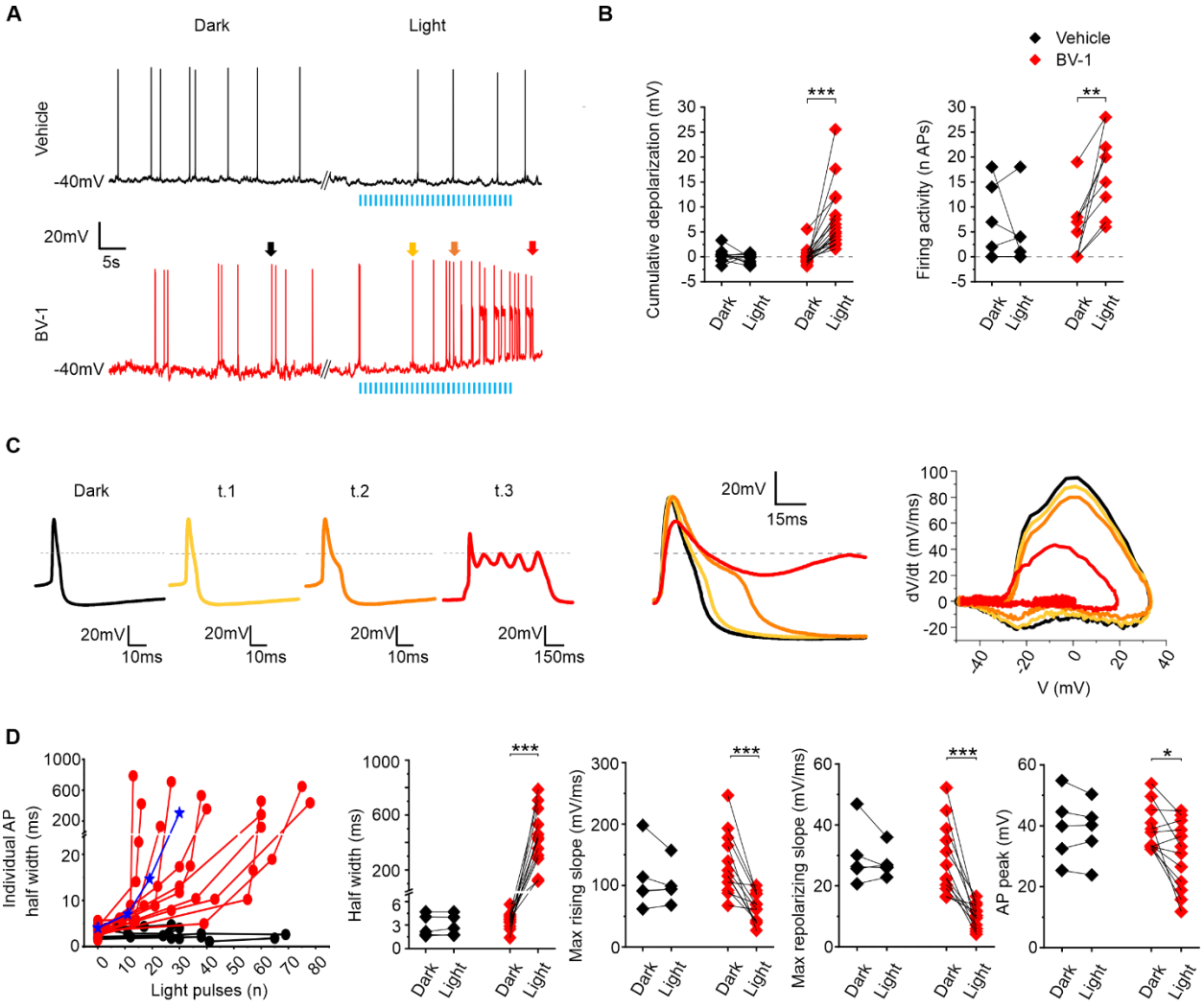

Figure 22 Light-dependent modulation of neuronal firing by BV-1

A. Action potential (AP) traces measured from neurons incubated with either Vehicle (H_2O) or BV-1 (1 µM) in the dark or under light-pulse stimulation (1 Hz, 20 ms, 30 light-pulses, 3 mW/mm²). Excitatory and inhibitory synaptic activities were pharmacologically blocked and APs were recorded in CC configuration holding the membrane voltage at -40 mV. **B.** *Left:* Cumulative depolarization (membrane voltage at 300 ms before the end of the 40-s protocol compared to the initial membrane voltage) in neurons incubated with either Vehicle (black) or BV-1 (red) in the dark or under light-pulse stimulation as described in panel A (n = 10 and 18 for Vehicle and BV-1, respectively). *Right*: Firing activity calculated as the number of APs during 40 s in the dark and under light stimulation (n= 8 and 9 for Vehicle and BV-1, respectively). **C.** *Left*: Zoom-in of the APs recorded in panel A (colored arrows) in the dark and at subsequent time-points (black: dark; light yellow, orange and red: refer to t.1, t.2 and t.3, respectively). *Middle and right*: Superimposition of the four representative AP traces and respective phase-plane plots. **D.** AP half-width *versus* number of light pulses in individual neurons incubated with either Vehicle (black) or BV-1 (red). Data from the representative recordings of panels A and C are shown in blue. **E.** Phase-plane plot analysis of the AP waveform. From left to right: half-width, maximal rising slope, maximal repolarizing slope and AP peak recorded from either Vehicle (black) or BV-1 (red) treated neurons in the dark and at the end of the light stimulation (t.3) (n = 5 and 12 for Vehicle and BV-1, respectively).

*Statistics: *p<0.05, **p<0.01, ***p<0.001; paired Student's t-test or Wilcoxon's test.*

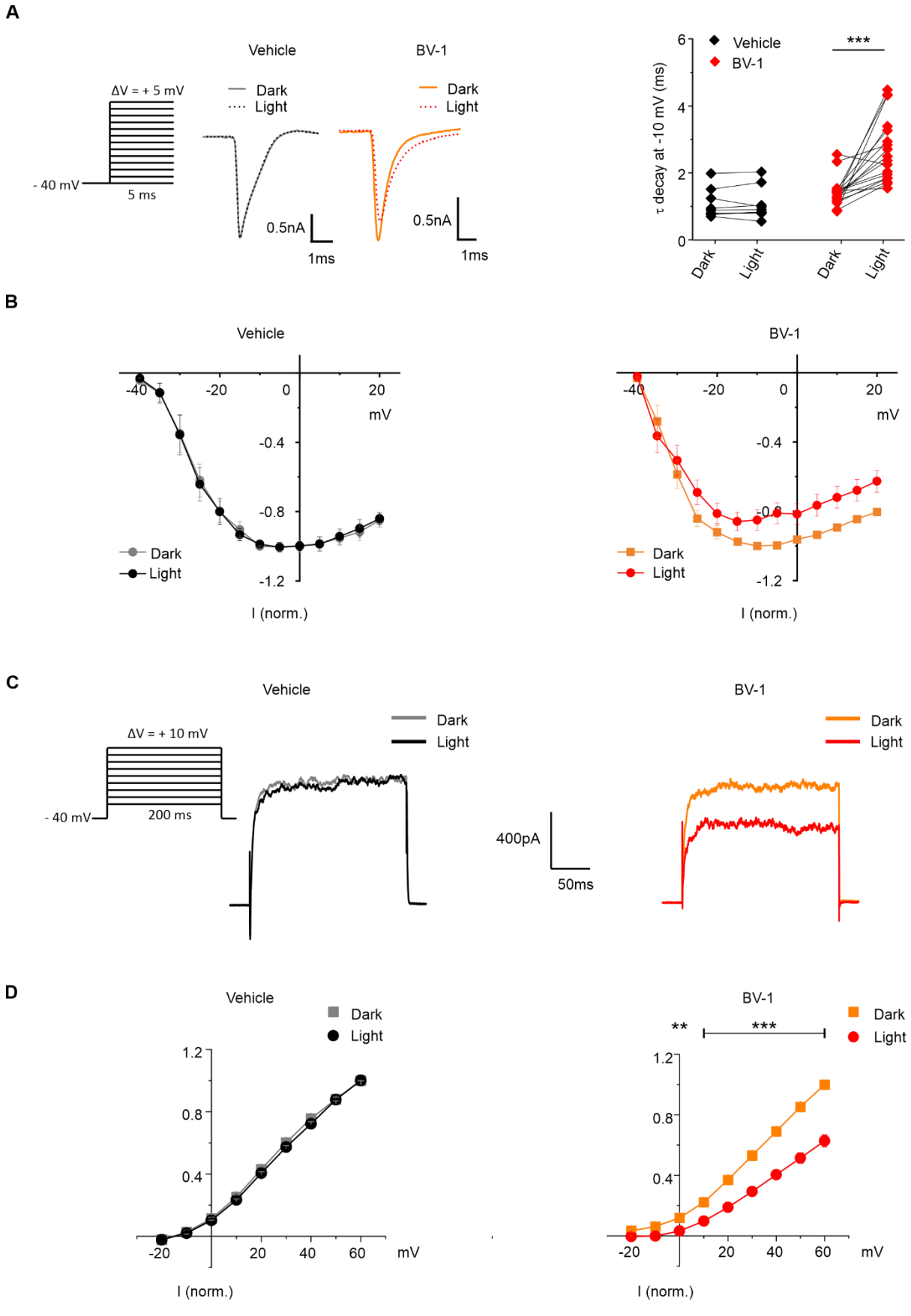
A
Vehicle
BV-1
ΔV = + 5 mV
- 40 mV
5 ms
Dark
Light
0.5nA
1ms
τ decay at -10 mV (ms)
***
B
mV
I (norm.)
C
ΔV = + 10 mV
200 ms
400pA
50ms
D
mV
I (norm.)
**
***

Figure 23 BV-1 light-dependent modulation affects voltage-gated sodium and potassium channels.
A. *Left:* Representative Na^+ current traces elicited by a depolarizing pulse to -10 mV from a holding potential (V_h) of -40 mV in the dark (grey traces: Vehicle; yellow traces, BV-1) and after 20-ms light stimulation (dotted traces). *Right:* Time constants of Na^+ current decay elicited at -10 mV in the dark and after light stimulation. (n = 12 and 20 for Vehicle and BV-1, respectively). **B.** Current-voltage (I/V) relationship in the dark (grey trace: Vehicle; orange trace: BV-1) and after light stimulation (black trace: Vehicle; red trace: BV-1) normalized to the peak current at -10 mV in the dark (n =12 and 20 for Vehicle and BV-1, respectively). Holding potential (V_h) -40 mV, steps between -40 and +20 mV for 5 ms, in 5-mV increments. Data are means ± SEM. **C.** Representative potassium currents elicited by a depolarizing pulse to +60 mV from a holding potential of -40 mV, in the dark (grey traces: Vehicle; yellow traces, BV-1) and after 20 ms light stimulation (dotted traces). **D.** Current-voltage (I/V) relationships in the dark and after light stimulation (n = 14 and 18 for Vehicle and BV-1). Potassium currents were elicited from a holding potential of -40 mV, by depolarizing neurons for 200ms, through voltage steps from -20 mV to +60 mV, applied in 10 mV increments. Color codes as in panel B. Data are means ± SEM.
*Statistics: ***p<0.001; paired Student's t-test (A), two-way ANOVA/Šídák's tests (D).*

4.4.5 Light stimulation of BV-1 loaded neurons induces membrane permeabilization to Na^+ ions, cell swelling, and cell death

Pore formation on the neuronal surface can disrupt ion permeability and affect the osmotic equilibrium of the cell. To investigate the impact of light stimulation, we examined the light-dependent changes in intracellular Ca^{2+} and Na^+ concentrations in BV-1 treated primary neurons. Neurons were loaded with either the fluorescent Ca^{2+} tracer Biotracker-609 Red Ca^{2+}-AM or the Na^+ tracer Ion NaTRIUM Green2-AM. Neurons were incubated with low-concentration BV-1 (100 nM), and a single 3-s light pulse was administered in the presence of synaptic blockers and TTX to prevent voltage-dependent Na^+ and secondary Ca^{2+} currents associated with action potential firing. While no noticeable increase in intracellular Ca^{2+} levels was observed in response to light stimulation immediately after light offset and 30 s later (Figure 24A), Na^+ levels exhibited a significant increase at both time points (Figure 24B). These results highlight the predominant role of Na^+ influx in mediating the effects of photostimulation and suggest a monovalent cation specificity of the pores generated by BV-1 upon light stimulation.

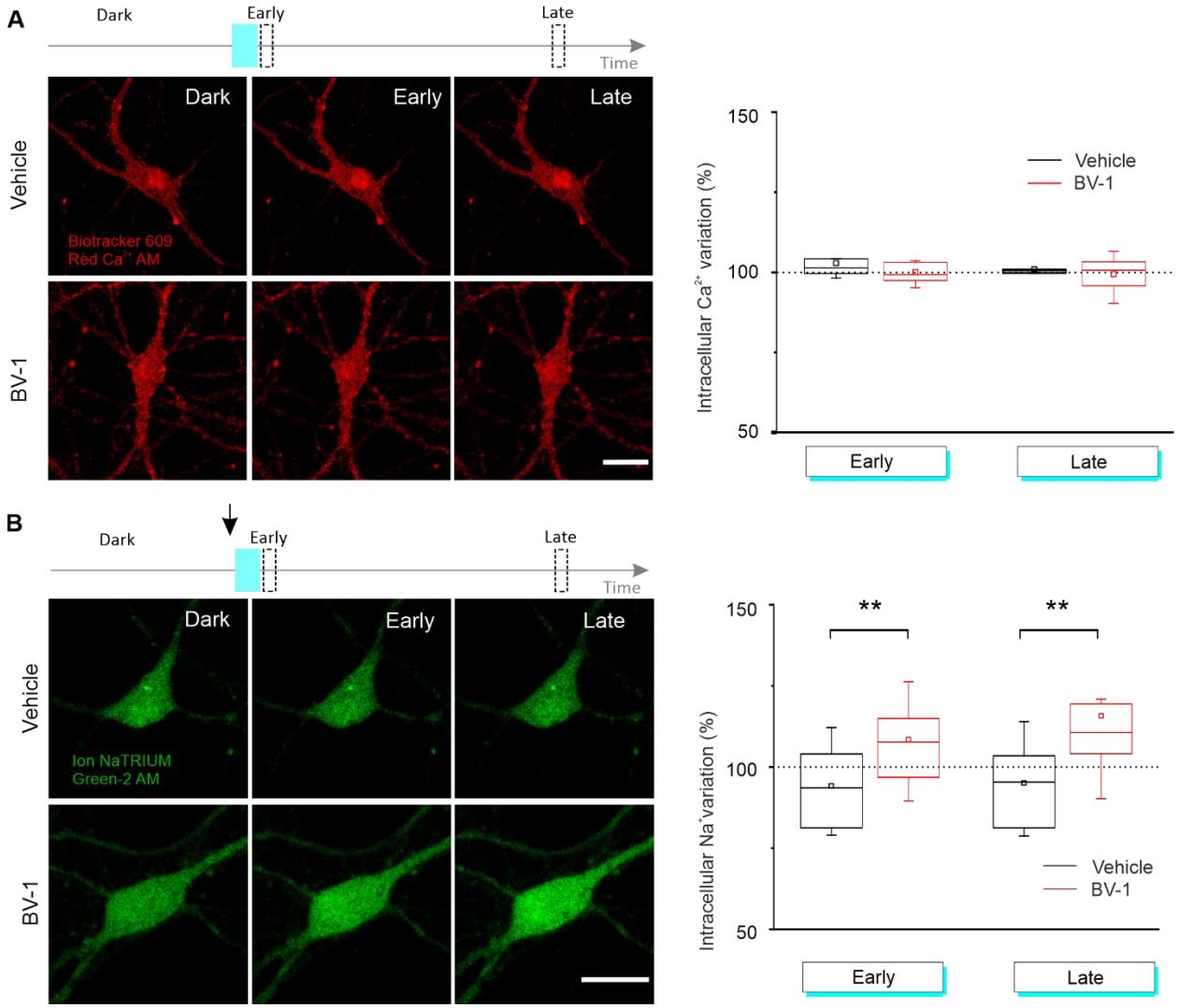

Figure 24 Light stimulation of BV-1 loaded neurons induces selective membrane permeabilization upon prolonged illumination.

A. *Left:* Representative confocal images of intracellular Ca^{2+} levels using a Ca^{2+} fluorescent tracer (Biotracker 609 Red Ca^{2+} AM) at 0 and 30 s after light stimulation. Primary hippocampal neurons were incubated with either Vehicle (H_2O, 0.1 %) or BV-1 (100 nM). Ca^{2+} levels were acquired immediately after (Early) and 30 s after (Late) a single-pulse light stimulation (3 s at 3 mW/mm^2). All acquisitions were performed in the presence of synaptic blockers and TTX (1 µM) in the extracellular medium. Scale bar, 20 µm. *Right:* Quantification of the early and late changes in intracellular Ca^{2+} levels. The fluorescence increases of the Ca^{2+} tracer upon light stimulation were normalized by the fluorescence levels in the dark (F/F_0 x 100) (n = 5 and 11 for Vehicle and BV-1, respectively). **B.** *Left:* Representative confocal images of intracellular Na^+ levels using a Na^+ fluorescent tracer (Ion NaTRIUM Green-2 AM) at 0 and 30 s after light stimulation. Basal levels of Na^+ were defined in the dark prior to incubation. After incubation with either Vehicle (H_2O, 0.1 %) or BV-1 (100 nM), neurons were light-stimulated with cyan light at 3 mW/mm^2 for 3 s. Na^+ levels were acquired immediately after (Early) and 30 s after (Late) a single-pulse light stimulation (3 s at 3 mW/mm^2). All acquisitions were performed in presence of synaptic blockers and TTX (1 µM) in the extracellular medium. Scale bar, 20 µm. *Right:* Quantification of the early and late changes in intracellular Na^+ levels. The fluorescence increases of the Na^+ tracer upon light stimulation were normalized by the fluorescence levels in the dark (F/F_0 x 100) (n = 11 and n=16 for Vehicle and BV-1, respectively).

*Statistics: *p<0.05, **p<0.01, ***p<0.001; unpaired Student's t-test/Mann-Whitney's U-test (A,B).*

Having established the presence of membrane pores induced by BV-1 under illumination, we examined osmotic effects and neuronal viability based on the duration of light stimulation. BV-1-treated primary neurons were subjected to continuous light stimulation at 3 mW/mm^2 for 1 s, and their somatic area was measured using live-labeling with Calcein Red/Orange. The light-induced inward ionic flux led to a progressive osmotic swelling of the neuronal cell body (Figure 25).

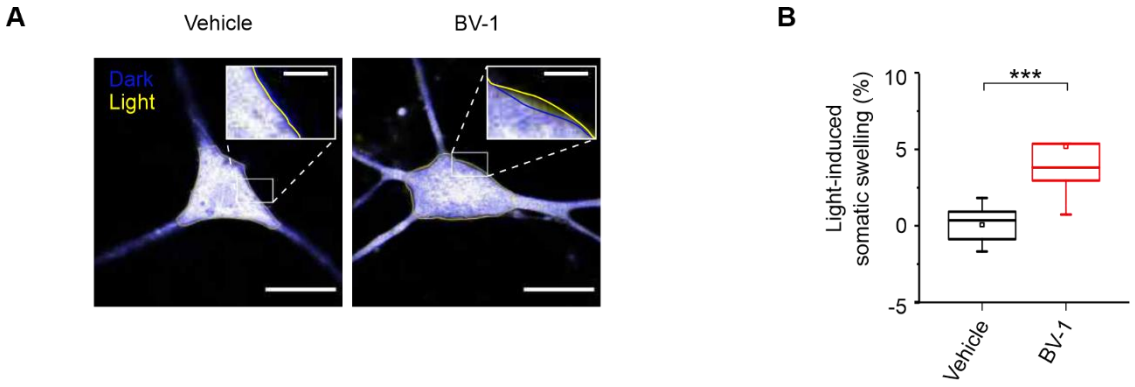

Figure 25 Light induces somatic swelling in neurons incubated with BV-1
A. Representative confocal images of primary hippocampal neurons with the intracellular volume labeled with Calcein Red-Orange and incubated with either Vehicle (H2O; 0.1% v/v) or BV-1 (1 µM). The same neuron in the dark (blue) and 1 min after 1-s light stimulation (3 mW/mm^2, yellow) are superimposed. Scale bars, 20 and 4 µm, for low and high magnification, respectively. **B.** Quantification of light-dependent variation of the somatic area normalized to the area measured in the dark (n = 13 and n=16 for Vehicle and BV-1, respectively).
*Statistics: ***p<0.001, Mann-Whitney U-test.*

Given the observed swelling and the substantial irreversibility of BV-1 effects, we investigated whether prolonged continuous illumination could induce light-triggered neuronal death. BV-1 treatment in the dark did not affect neuronal viability compared to untreated or vehicle-treated neurons (Figure 26A). However, while short light stimulation (e.g., 10 light pulses of 200 ms at 1 Hz) did not impact neuronal viability, continuous illumination for 30 seconds resulted in significant cell death of approximately 50%, as evidenced by propidium iodide incorporation (Figure 26B).

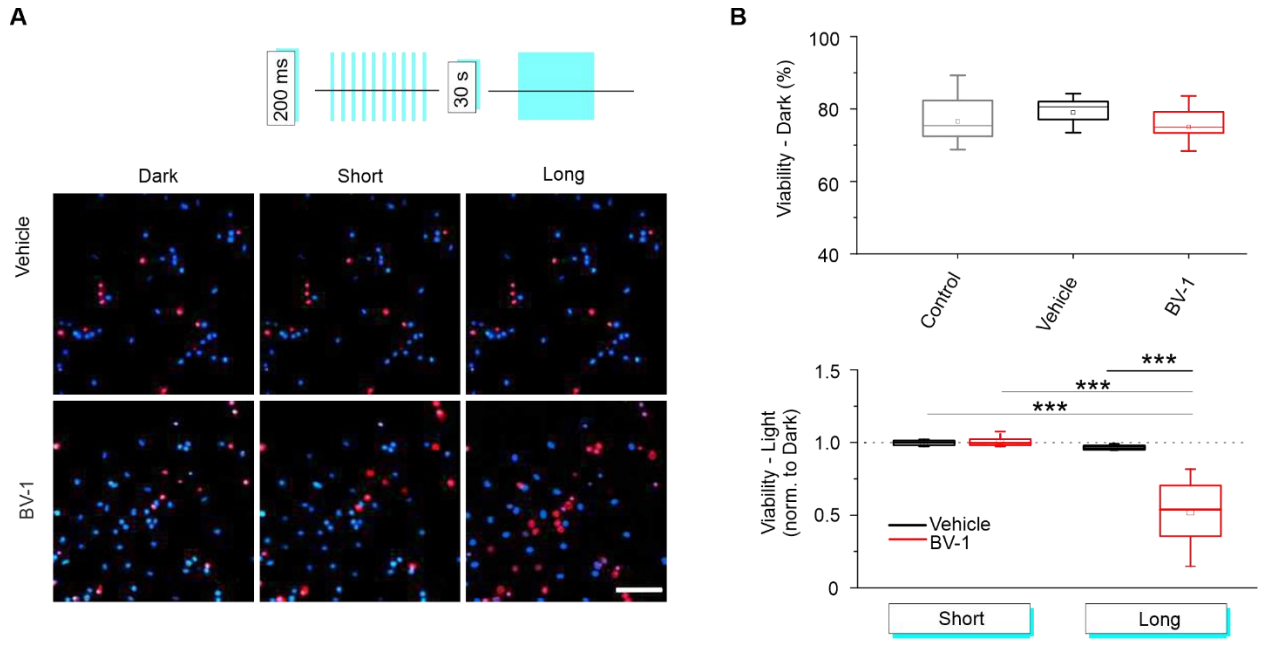

Figure 26 Prolonged light stimulation of BV-1 loaded neurons induces cell death
Neuron viability in the dark and upon sustained light stimulation. *Left:* Neurons were incubated with either Vehicle (H_2O; 0.1%) or BV-1 (1 µM) and viability was quantified in the dark, after a train of 10 short light-pulses (200 ms, 1 Hz, 3 mW/mm^2) and after 30-s continuous light stimulus (3 mW/mm^2). Untreated primary neurons were used as control. Neurons were stained with propidium iodide (PI; 1 µM; red) for dead cell counts and the nuclear stain Hoechst 33342 (1 µM, light blue) for total cell counts. Scale bar, 200 µm. *Right:* Quantification of cell viability in the dark and after light stimulation. Percent viability in the dark (upper panel; n = 27, 21 and 56 fields for Control, Vehicle, and BV-1, respectively from at least 3 independent preparations) and after the two light stimulation protocols (lower panel; n = 6 and n=8 fields for Control and BV-1, respectively from at least 3 independent preparations). The viability data after light stimulation were normalized by the respective values obtained in the dark.
*Statistics: ***p<0.001; one-way ANOVA/Šídák's tests.*

4.4.6 Local application of BV-1 enables light-modulated perforated patch-clamp recordings

To investigate the potential applications of BV-1 and explore its unique features for controlled optoporation, our objective was to intentionally induce local optoporation in specific membrane patches, utilizing the pore-forming effects induced by BV-1 during prolonged light stimulation. BV-1 was loaded into the patch pipette containing the internal solution, and a cell-attached configuration was obtained (Figure 27A). The increase in transient capacitive current, resulting from a 5-mV depolarizing step lasting 20 ms from a holding potential of -70 mV, was analyzed to assess the appearance of pores in the membrane patch during prolonged pulsed light stimulation. Pore formation was determined when the Q_{peak} reached a plateau (Figure 27B). At this plateau, we observed a significant increase in Q_{peak} and a

significant reduction in patch resistance compared to the dark condition, indicating light-induced membrane perforation (Figure 27C, D). BV-1 offers advantages over existing perforant molecules, not only in providing control over the initiation of membrane perforation through light stimulation, but also showing a consistently faster onset, with the average time to reach the plateau ranging from 2 to 5 min (Figure 27E). This rapidity contrasts with established perforating techniques involving antibiotics like amphotericin B, nystatin, or gramicidin that are much slower in achieving membrane perforation (Ebihara et al., 1995; N., 1994; Rae et al., 1991).

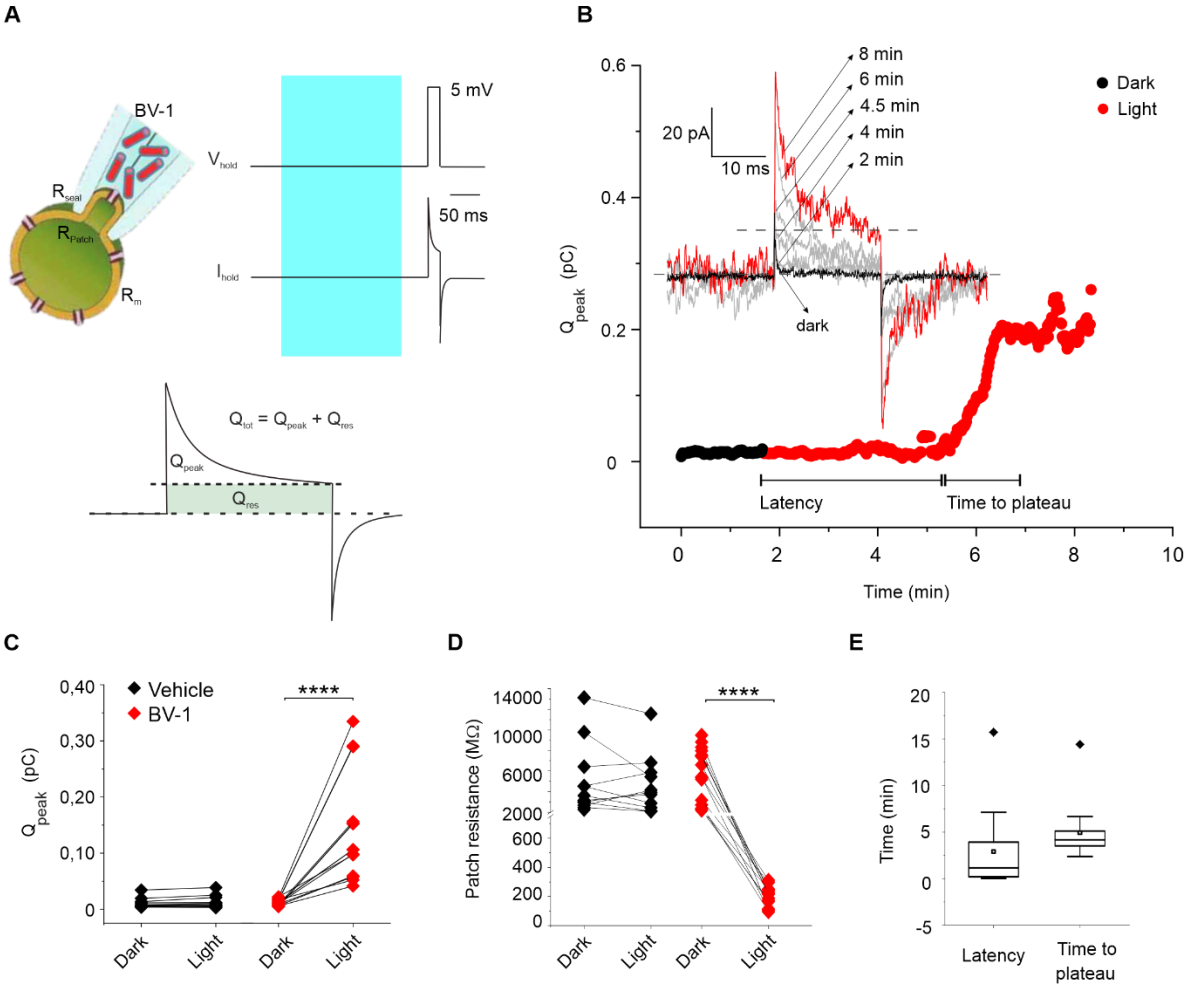

Figure 27 Light-triggered membrane poration dynamics from cell-attached to perforated-patch configuration by BV-1.

A. Measurements were performed on primary hippocampal neurons in the cell-attached configuration with BV-1 (0.1 µM) in the patch pipette. The transient capacitive currents were elicited by 20 ms depolarizing voltage step of 5 mV from a holding potential of -70 mV, in the absence of light-stimulation (Dark) or after successive cycles of illumination (200 ms, 3 mW/mm²). **B.** Representative charge modulation over time in the dark and upon illumination calculated as shown in the bottom part of panel A (Q_{peak}). The inset shows the capacitive currents in the dark (black trace) and at successive times during light stimulation (grey and red traces). **C,D.** Q_{peak} amplitude (**C**) and patch resistance (**D**) in the dark and after subsequent cycles of illumination (left and right respectively; n = 18 and 17 for Vehicle and BV-1). **E.** Distribution of the latency and time-to-plateau obtained by the evaluation of Q_{peak}/time relationships in BV-1 treated neurons (n = 17).

*Statistics: ***p<0.001; paired Student's t-test or Mann-Whitney's U-test (C,D).*

4.4.7 Light-dependent neuronal firing and activity silencing by BV-1 in blind retinal explants and mouse visual cortex after short and prolonged light stimuli

The bifunctional properties of BV-1, which is inactive in the dark but induces neuronal photostimulation or trigger neuronal death depending on the timing and intensity of light stimulation, were investigated in intact nervous tissue ex vivo (retinal explants) and in vivo (primary visual cortex, V1). Degenerated retinas from 12-month-old rd10 mice, a model of Retinitis pigmentosa, were acutely explanted and incubated with either Vehicle or BV-1. The retinas were placed on multielectrode arrays (MEAs) in the epiretinal configuration to record the firing activity of retinal ganglion cells (RGCs). Cyan light pulses were delivered at increasing power densities. Despite the absence of photoreceptors, both Vehicle-treated and BV-1-treated retinas displayed an initial and short-lived increase in light-evoked firing activity by intrinsically photosensitive RGCs (ipRGCs) (Figure 28.A). However, BV-1-treated retinas exhibited a significantly higher firing rate in response to the light train compared to Vehicle-treated retinas (Figure 28B, left panel), which is in line with the light-induced depolarization observed in primary neurons incubated with BV-1. The effect was quantified by calculating the ratio between the maximum firing rate during the first 100 safter light onset and the maximum firing rate evoked by ipRGCs at the initial light onset. BV-1-treated retinas showed a two-fold maximum firing rate during the early phase of light stimulation (Figure 28B, left panel). However, in a later phase of the illumination protocol (>100 s after light onset), BV-1 led to a pronounced silencing of RGC firing activity, while Vehicle-treated retinas maintained a stable firing rate over time (Figure 28B, right panel). The decrease in RGC firing progressed over time under light stimulation, with approximately 38 % of the electrodes displaying a strongly decreased firing rate after up to 300 s of light train stimulation (Figure 28B, right panel). These data align with the light-induced cell death upon long stimulation observed in primary neurons.

To investigate the dual effect of BV-1 on light-dependent neural activity modulation *in vivo*, either BV-1 or Vehicle was stereotaxically injected into the primary visual cortex (V1) of naïve mice. Optical stimulation was performed using a 430-nm laser, and extracellular recordings were performed. The diffusion of BV-1 within cortical tissue was observed to have an approximately 200 µm diameter around the injection site (Figure 28C). Optical stimulation evoked a significant increase in the multi-unit activity of V1 cortical neurons, which was evident immediately after the 200-ms light pulses (Figure 28D). Calculating the ratio between the maximum firing rate measured after each stimulation pulse and the baseline firing rate revealed a significant two-fold increase in cortical firing activity in BV-1-injected mice

compared to Vehicle-injected controls (Figure 28D, right panel). Following the short-pulse light stimulation protocol, the injected mice underwent prolonged light stimulation of 30 s. Under these conditions, the light-locked firing was lost, and retrospective immunohistochemical analysis of the injected areas demonstrated a significant increase in active caspase-3-positive neurons, indicating the presence of light-triggered programmed cell death (Figure 28E) as seen in primary neurons.

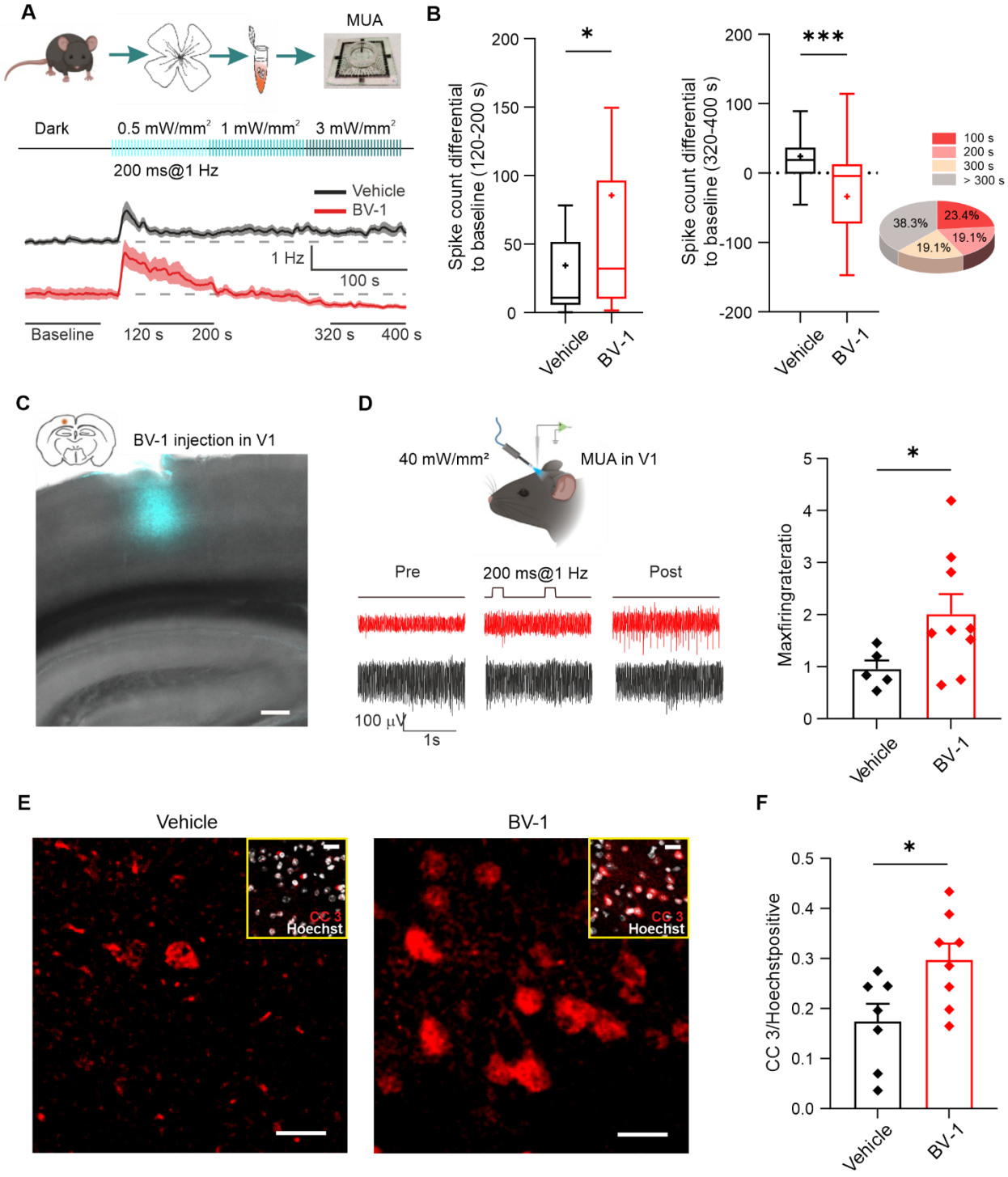

Figure 28 Light-dependent modulation of firing activity by BV-1 in blind retinal explants and primary visual cortex in vivo.

A. Schematic representation of the *ex vivo* experiments. Explanted blind rd10 retinas incubated with either Vehicle (H_2O, 10 %, black trace) or BV-1 (5 µM, red trace) for 30 min were positioned onto MEA in epiretinal configuration, stimulated with the illustrated illumination protocol (200 ms cyan light pulses, 1 Hz, 0.5, 1 and 3 mW/mm^2) to evoke RGC multiunit firing activity (MUA) represented as Peri-Stimulus Time Histograms (PSTHs). **B.** Light-evoked RGC firing rates in blind retina explants. *Left:* Early changes in RGC firing. After an initial and short-lived physiological increase in the light-evoked firing activity (see panel A) ascribed to intrinsically photosensitive RGCs (ipRGCs), BV-1 treated retinas showed a significantly higher firing rate with respect to the Vehicle-treated group. The effect was quantified as the ratio between the maximum firing rate recorded during the first 100 s after light onset and the maximum firing rate evoked by ipRGCs at the first light onset (n = 42 and n=44 electrodes for Vehicle and BV-1, respectively from 5 rd10 mice). *Right:* Late changes in RGC firing. Quantification of the firing rate in a later phase of the illumination protocol (between 100 and 200 s after light onset) revealed a significant decrease of the activity in BV-1-treated retinas with respect to the mean firing rate of Vehicle-incubated retinas. The inset shows the percentage of electrodes having a significantly decreased firing at 100, 200, and 300 s after light onset. In ~38 % of the electrodes at times > 300 s the firing rate was not affected by the illumination (n = 37 and n=41 electrodes for Vehicle and BV-1, respectively from 5 animals). **C.** BV-1 (500 µM in 1 µl of PBS) was injected in the V1 cortex of naïve C57BL/6 mice (top-left schematic). A representative confocal image of V1 slices showed a spread of BV-1 of ~200 µm (cyan), as detected through the molecule intrinsic fluorescence. Scale bar, 200 µm. **D.** *Left:* Schematic representation of the setup for *in vivo* MUA recordings in either Vehicle- or BV-1-injected visual cortices (V1) light stimulated with an optic fiber in the proximity of the injection site (430 nm, 40 mW/mm^2). Representative traces of extracellular signals recorded before (pre), during (200 ms pulses at 1 Hz; 100 sweeps) and after (post) illumination of C57BL/6 mice injected with either Vehicle or BV-1. *Right:* Mean $\pm$ sem ratio between the maximum firing rates recorded after and before each stimulation protocol showed a significant increase of cortical activity in BV-1 injected mice compared to sham-treated controls (n = 5 and n=9 animals for Vehicle and BV-1, respectively; at least 3 recordings for each animal). **E**. Following the illumination protocol described in D, the injected areas were subjected to a prolonged stimulation of about 30 to 60 s. Representative confocal images of brain slices stained for active caspase-3 (Cas3, red) and nuclei (Hoechst 33342, white) in a region adjacent to the injection site that was subjected to prolonged illumination in either Vehicle or BV-1 injected animals. The inset shows the merged channels. Scale bar, 20 µm**. F.** Quantification of the ratio between the number of active caspase-3 and Hoechst 33342 positive neurons shows a significant increase in programmed cell death in brains injected with BV-1 with respect to the control group subjected to the same sustained light stimulation (n = 7 and n=8 mice for Vehicle and BV-1, respectively).

*Statistics: *p<0.05, **p<0.01; unpaired Mann-Whitney's U-test (B, D, and F).*

5 Discussion and Conclusion

This doctoral thesis explores the use of light for neural stimulation, concentrating on four newly synthesized membrane-targeted photochromic molecules. Engineered for optostimulation, these compounds present an alternative to genetic manipulation in modulating neural circuits. Significantly, they demonstrate the capacity to selectively influence passive properties of the neuronal membrane without disrupting fundamental physiological processes. The exploration starts with a detailed characterization of Ziapin2, previously found to increase neuronal firing with light, unraveling its potential role in modulating synaptic neurotransmission. Subsequently, the study scrutinizes three additional molecules—2Pyr-2Pyr, Push-Pull molecules, and BV-1—each offering unique insights into light-induced neuronal stimulation.

5.1 Ziapin2: unraveling dual modulation in excitatory and inhibitory neurons

Earlier studies established Ziapin2's efficacy in triggering increased neuronal firing upon exposure to visible light (DiFrancesco et al., 2020). Given its prevalent localization within lipid rafts—a pivotal scaffold organizing synaptic proteins—an exploration was prompted into its potential additional effects on synaptic neurotransmission. To achieve a thorough characterization, this study considered the structural and physiological variances between excitatory and inhibitory neurons, offering an in-depth analysis of synaptic modulation across these distinctive neuronal subpopulations.

Notably, Ziapin2 induced alterations in postsynaptic currents by impacting the dynamics of neurotransmitter release. In excitatory neurons, it resulted in an augmentation of postsynaptic currents, increasing the release probability during light stimulation. In inhibitory neurons, it elicited the opposite modulation, however by affecting the availability of SVs ready to fuse without modulating the release probability (Figure 29). The observed differential modulation of synaptic transmission in excitatory and inhibitory neurons by Ziapin2 raises intriguing questions about the underlying mechanisms.

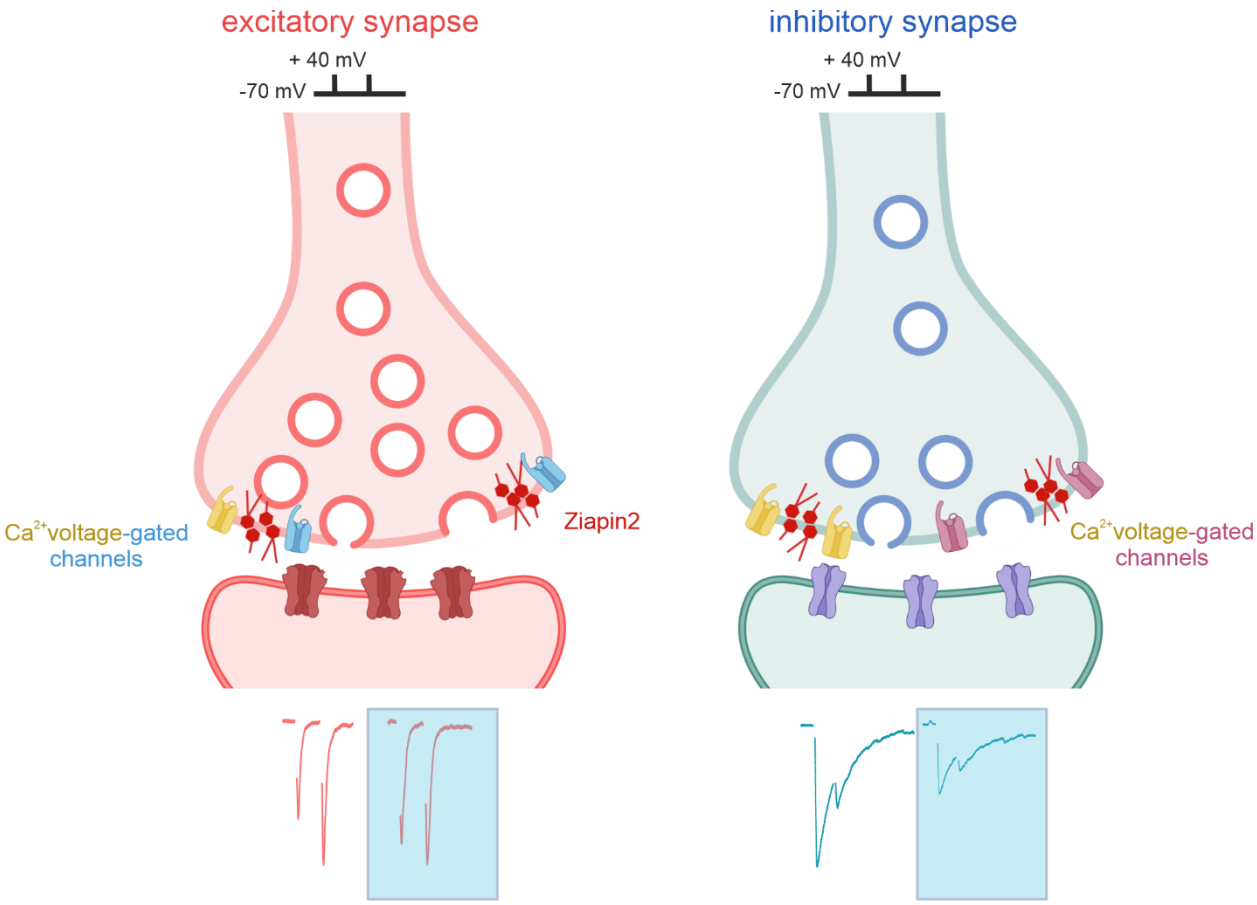

Figure 29 Ziapin2-mediated modulation of synaptic transmission: distinct effects on excitatory and inhibitory synapses

The schematic representation highlights the structural distinctions between excitatory and inhibitory synapses, including the expression of different voltage-gated calcium channels crucial for neurotransmitter release and variations in the sizes of the ready releasable pool. Ziapin2 is known to spontaneously associate with lipid rafts, particularly enriched in ion channels. Upon exposure to light stimulation, there is an observed increase in the amplitude of the first excitatory postsynaptic current (eEPSC). Conversely, in inhibitory neurons, light stimulation induces the opposite effect. In excitatory neurons, this increase in eEPSC amplitude has been experimentally linked to heightened release probability. The hypothesis is put forward that the opposite holds true in inhibitory neurons, in which the response of Ziapin2 to light would partially disassemble the RRP by virtue of its effects on membrane structure and/or topographical changes between voltage-gated Ca^{2+} channels and docked SVs in the RRP.

Figure created with Biorender.com

Excitatory and inhibitory synapses differ in physiological SV release probability, SV number, VGCCs and short-term plasticity (Schmidt et al., 2013; Takahashi & Momiyama, 1993). Studies have highlighted the critical role of VGCC subtype, density, and coupling efficiency with vesicle release at the presynaptic active zone as determinants of synaptic function (Sheng et al., 2012; Vyleta & Jonas, 2014; Wheeler et al., 1994). Considering that Ziapin2 induces light-dependent membrane stretching and the enrichment of membrane

proteins, including ion channels, within lipid rafts, it is plausible that the modulation of membrane capacitance by Ziapin2 indirectly influences VGCCs, as demonstrated with other ion channels (Moschetta et al., 2023). However, membrane stretching could also interfere with SVs fusion process at the active zone as widely demonstrate in many cellular models of exocytosis (Wang & Galli, 2018).

The distinct physiological characteristics between excitatory and inhibitory synapses may contribute to the differential synaptic neurotransmission modulation induced by Ziapin2 upon light stimulation (Figure 29). Excitatory synapses exhibit a very low release probability (<0.1) of SVs in response to a single AP (Rosenmund et al., 1993), possibly due to a lower density of VGCCs at the active zone or a greater distance (weaker coupling) between VGCCs and SVs that constitute the RRP. Here, light-induced membrane stretching by Ziapin2 could enhance VGCC currents or promote a more effective coupling between VGCCs and SVs, thereby increasing the probability of the fusion process.

In contrast, inhibitory synapses exhibit higher density and current of VGCCs, achieving maximal efficiency in the coupling between calcium influx and SV fusion, resulting in extremely high release probability values (>0.5). In this scenario, the light-dependent membrane stretching induced by Ziapin2 may introduce a perturbation to the delicate coupling between VGCCs and SVs within the RRP. While moderate, this perturbation could potentially negatively impact the quantity of SVs released in response to a single AP.

These findings raise the hypothesis that Ziapin2 may have effects on presynaptic calcium currents, which are crucial for neurotransmitter release, exerting a direct effect on the VGCCs that are present in the lipid rafts or indirectly through membrane stretching. This modulation might differ in excitatory and inhibitory neurons due to variations in VGCCs, the structural conformation of the synapse machinery, and the presence of different calcium buffering systems in the two neuronal populations. Further investigation into the modulation of presynaptic calcium levels in both neuronal subpopulations is required to validate this hypothesis.

While acknowledging the considerable diversity in synapse conformation and protein expression across brain regions and neuronal subtypes, this study demonstrates the potential of Ziapin2 to induce a distinct synaptic modulation dependent on the specific physiological synaptic profile it encounters. This nuanced modulation gains particular relevance in the context of vision, where diverse pathways respond divergently to light exposure. Understanding the precise mechanisms through which Ziapin2 modulates these pathways not only paves the way for targeted interventions, but also holds promise for strategies

aimed at restoring vision. Ziapin2 could be a key player in conferring light sensitivity to remaining retinal neurons after photoreceptor degeneration.

5.2 Enhancing neural modulation: prolonged membrane residence and structural innovation with 2Pyr-2Pyr compared to Ziapin2

In contrast to Ziapin2, 2Pyr-2Pyr, a single-molecule approach with two Pyridine groups on both side of the azobenzene core, combines all components in one. Molecular Dynamics (MD) simulations revealed spontaneous insertion into the outer membrane leaflet, aligning Pyridine terminals with lipid heads. Similar to Ziapin2, 2Pyr-2Pyr also exhibited aggregation tendencies, validated in hippocampal neurons, indicating stable accumulation over time. The MD simulation's prediction of localized membrane shrinkage in the dark raised the hypothesis that light-triggered isomerization of 2Pyr-2Pyr would induce a transient decrease in membrane capacitance, a hypothesis confirmed by experimental results demonstrating a significant decrease in evoked capacitive charge during light stimulation, confirming the light-dependent modulation of membrane properties.

Whole-cell patch-clamp recordings on primary hippocampal neurons revealed that 2Pyr-2Pyr induces light-dependent modulation of membrane voltage, displaying a pattern similarly to Ziapin2, including hyperpolarization, delayed depolarization, and light-dependent firing activity, highlighting its comparable modulation despite structural differences.

In summary, the results highlight 2Pyr-2Pyr's potential as a singular light-responsive neural modulator, distinguished by its membrane interaction and capacitance modulation. Its extended presence in the cell membrane over several days, surpassing Ziapin2, presents a hopeful trajectory for sustained efficacy. Yet, the quest for prolonged modulation demands deeper investigations. The unique structure of 2Pyr-2Pyr paves the way for external anchoring possibilities, offering a strategic approach to circumvent membrane recycling mechanisms and secure enduring membrane stability for sustained neural modulation. Additionally, elucidating its preference for lipid rafts, akin to Ziapin2, is imperative for unraveling its comprehensive light-dependent effects beyond neuronal firing. This multifaceted characterization lays the groundwork for a deep understanding and application of 2Pyr-2Pyr in the domain of neural stimulation.

5.3 Push-Pull molecules: light-induced depolarization with absence of firing activity, revealing a subtle neural stimulation

The studied Push-Pull molecules, utilizing a donor-acceptor strategy distinct from Ziapin2 and 2Pyr-2Pyr, induce a light-dependent depolarization in primary hippocampal neurons. MD simulations affirmed their spontaneous integration into the cellular membrane, revealing no interactions between molecules and no modulation of membrane capacitance. This highlights the reliance of the light-dependent effect on the inherent donor-acceptor mechanism within the molecule. In contrast to Ziapin2 and 2Pyr-2Pyr, Push-Pull induced an immediate depolarization upon light stimulation, comparable in amplitude to Ziapin2, but lacking the preceding hyperpolarization. Although the induced transient depolarization is not sufficient to trigger light-dependent firing activity, these molecules provide valuable insights into the requirements for functional photoswitches in neuronal light stimulation. Surprisingly, despite the conventional understanding that depolarization is necessary to open voltage-dependent ion channels for neuronal firing, our findings suggest that the pivotal factor is the initial hyperpolarization. This hyperpolarization elicits the rebound depolarization, facilitating firing even with a modest membrane voltage modulation of a few mV. This observation opens new avenues for exploring the interplay between membrane dynamics and photoswitch mechanisms in achieving effective neuronal modulation.

5.4 BV-1: exploring versatility in light-dependent neural stimulation beyond firing activity

In the exploration of novel light-dependent compounds, BV-1 emerges as a compelling candidate, showcasing spontaneous membrane incorporation and light-controlled modulation. Unlike other photoswitches studied in this thesis, such as Ziapin2 and 2Pyr-2Pyr, BV-1 employs a unique mechanism characterized by charge reorganization upon visible light illumination, leading to intramembrane clustering. MD simulations and experimental evidence affirm the BV-1 capacity for membrane thinning, aggregation, and selective permeability to monovalent cations upon light stimulation (Figure 30).

The ability of BV-1 to evoke excitatory effects and create pores establishes it as a versatile tool, comparable to gramicidin and non-aqueous polyene pores, yet unique in its light-dependent regulation. Notably, when employed in patch pipettes, BV-1 surpasses conventional antibiotic-based setups, ensuring a stable seal, water solubility, on-demand permeabilization, and swift pore formation, ultimately enabling light-triggered perforated patch-clamp configurations.

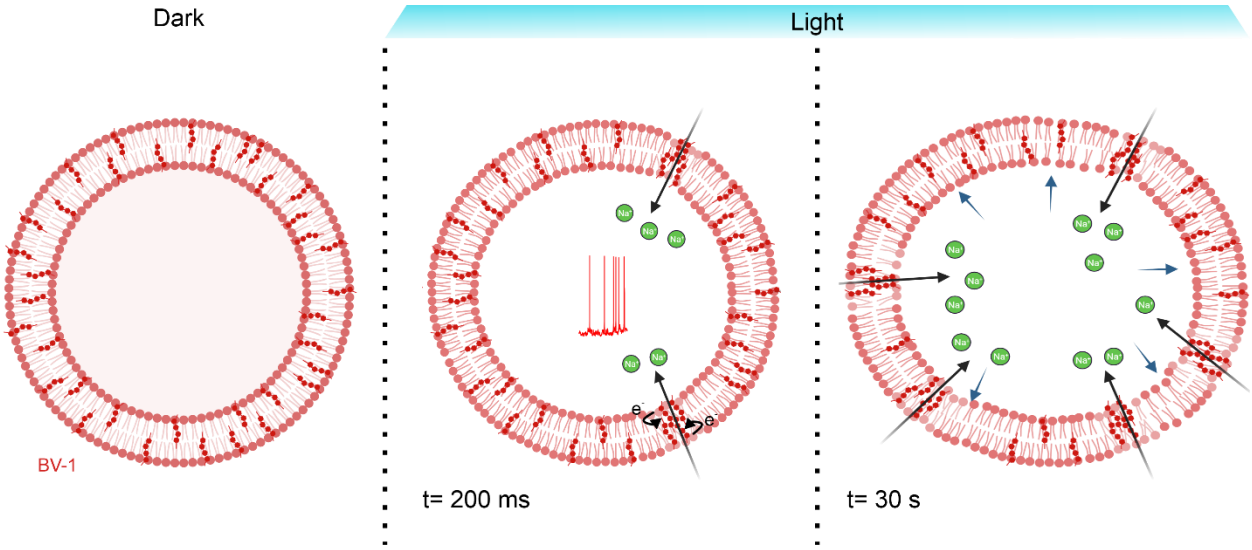

Figure 30 Light-induced effects of BV-1 on membrane stability
Left: BV-1 spontaneously incorporates into the cellular membrane in the dark, aligning with lipids. *Center:* Upon 200-ms light stimulation, electron transfer occurs within some BV-1 molecules, promoting the aggregation of multiple BV-1 molecules. This aggregation disrupts membrane integrity, resulting in pore formation in the cell membrane, facilitating sodium passage and inducing membrane depolarization and increased firing activity (red trace). *Right:* Prolonged light exposure leads to increased aggregation of BV-1 molecules, intensifying cell permeabilization and osmotic imbalance. Ultimately, this process culminates in cell swelling (blue arrows) and eventual cell death.
Figure created with Biorender.com

The diverse effects of BV-1 extend beyond its initial design, demonstrating a broader range of applications despite its original intent for triggering light-dependent firing activity in neurons. *In vitro, ex vivo, and in vivo*, under prolonged illumination, BV-1 has shown the capability to induce cell death due to the extent of the induced permeabilization and cell swelling. Nevertheless, BV-1 distinguishes itself from common dyes used in photodynamic therapy in several key aspects.

Traditional photodynamic therapy dyes typically induce cell death solely through the production of reactive oxygen species (ROS), leading to oxidative stress and cellular damage (Abrahamse & Hamblin, 2016). In contrast, BV-1 operates through a unique mechanism involving charge reorganization upon visible light illumination, leading to intramembrane clustering. BV-1 has been shown to cause membrane

thinning and selective permeability to monovalent cations upon light stimulation. With short light stimulation, BV-1 induces no cell death but increases neuronal firing. Its pore-forming characteristic also presents the possibility of being utilized as an electrophysiological tool for perforating patch-clamp configurations. Moreover, while common photosensitizers may localize in various cellular compartments, contributing to broad-spectrum and long-lasting damage, BV-1 exhibits light-sensitivity only when present in the cell membrane, reducing the risk of long-lasting damage, as with time it gets internalized due to membrane turnover.

This unique combination of excitatory and cytotoxic effects positions BV-1 as a promising tool for targeted applications in diverse neurological and translational contexts, opening avenues for future applications in tumor suppression or modulation of hyperexcitable neurons within epileptic foci. In fact, in future perspectives, BV-1 could be further engineered to target specific cells and allow specific cell death induction with high resolution in time and space, which is highly desirable for the suppression of several medical challenges, such as drug-resistant epileptic foci and very aggressive tumors such as glioblastoma. Current treatment approaches often encounter limitations in achieving precise and effective outcomes. Interventions for epileptic foci are particularly challenging due to the complexity of neural networks involved and the potential for widespread impact on normal brain function (Concepts et al., 2011). BV-1's capacity for light-triggered effects allows for spatiotemporal control, meaning it could be activated only in specific regions and at specific times, minimizing the impact on surrounding normal brain function. Similarly, glioblastoma, being an aggressive form of brain cancer, poses substantial challenges with infiltrative growth, making complete surgical removal difficult (Wirsching et al., 2016). These complexities underscore the critical need for innovative and targeted therapeutic strategies, and BV-1's unique properties position it as a hopeful avenue for addressing these intricate medical challenges.

5.5 Navigating the future: advancements and considerations in photoswitch development - final remarks

In the pursuit of innovative light-responsive compounds, the exploration of Ziapin2, 2Pyr-2Pyr, and Push-Pull molecules alongside the intriguing BV-1 has unraveled a diverse landscape of possibilities for neural stimulation. Ziapin2, localized within lipid rafts, forms dimers between Ziapin2 molecules, intricately modulating neuronal activity by inducing light-dependent dimers disruption and consequent membrane stretching. This alteration induces increased firing activity and alters postsynaptic currents, exhibiting dual effects in excitatory and inhibitory neurons. In contrast, 2Pyr-2Pyr, a further engineered form of Ziapin2, achieves a single-molecule approach and demonstrates prolonged membrane residence and structural

innovation, presenting potential for sustained efficacy in neural modulation compared to Ziapin2. Push-Pull molecules utilize a donor-acceptor strategy, inducing light-dependent depolarization without triggering firing activity. BV-1, the only non-azobenzene-based photoswitch presented, features a unique mechanism involving charge reorganization. It demonstrates versatile effects, encompassing light-dependent aggregation within the cell membrane, leading to pore formation and, ultimately, the capability to induce cell death. This positions BV-1 as a promising tool for diverse neurological applications, from modulating hyperexcitable neurons to potential tumor suppression.

Together, these compounds offer a nuanced understanding and diverse potential for light-driven neural modulation. This exploration into photoswitches has uncovered various opportunities for neural stimulation. As we delve into the relationships among molecular structure, membrane dynamics, and light-responsive effects, ongoing research to improve photoswitch design becomes crucial. Strengthening their structural integrity and permanence in the membrane is essential for realizing their full potential as a reliable alternative to optogenetics. The complex interactions between these compounds and neural membranes offer the potential to influence the future of targeted neurostimulation. This drives us towards a more profound understanding and more effective applications in neurological contexts.

6 References

Abrahamse, H., & Hamblin, M. R. (2016). New photosensitizers for photodynamic therapy. *The Biochemical Journal*, *473*(4), 347. https://doi.org/10.1042/BJ20150942

Allen, J. A., Halverson-Tamboli, R. A., & Rasenick, M. M. (2007). Lipid raft microdomains and neurotransmitter signalling. *Nature Reviews. Neuroscience*, *8*(2), 128–140. https://doi.org/10.1038/NRN2059

Baldelli, P., Fassio, A., Valtorta, F., & Benfenati, F. (2007). Lack of Synapsin I Reduces the Readily Releasable Pool of Synaptic Vesicles at Central Inhibitory Synapses. *The Journal of Neuroscience*, *27*(49), 13520. https://doi.org/10.1523/JNEUROSCI.3151-07.2007

Bandara, H. M. D., & Burdette, S. C. (2012). Photoisomerization in different classes of azobenzene. *Chemical Society Reviews*, *41*(5), 1809–1825. https://doi.org/10.1039/C1CS15179G

Benfenati, F., & Lanzani, G. (2020). Clinical translation of nanoparticles for neural stimulation. *Nature Reviews Materials 2020 6:1*, *6*(1), 1–4. https://doi.org/10.1038/s41578-020-00267-8

Bhatia, A., Moza, S., & Bhalla, U. S. (2019). Precise excitation-inhibition balance controls gain and timing in the hippocampus. *ELife*, *8*. https://doi.org/10.7554/ELIFE.43415

Cao, K. J., Lyons, E. F., Smith, B. E., Denlinger, B. L., Ma, H., Shirian, J. D., & Kramer, R. H. (2021). Cyclodextrin-Assisted Delivery of Azobenzene Photoswitches for Uniform and Long-Term Restoration of Light Responses in Degenerated Retinas of Blind Mice. *Advanced Therapeutics*, *4*(9). https://doi.org/10.1002/adtp.202100127

Cao, Z. F. H., Burdakov, D., & Sarnyai, Z. (2011). Optogenetics: potentials for addiction research. *Addiction Biology*, *16*(4), 519. https://doi.org/10.1111/J.1369-1600.2011.00386.X

Carvalho-de-Souza, J. L., Treger, J. S., Dang, B., Kent, S. B. H., Pepperberg, D. R., & Bezanilla, F. (2015). Photosensitivity of neurons enabled by cell-targeted gold nanoparticles. *Neuron*, *86*(1), 207. https://doi.org/10.1016/J.NEURON.2015.02.033

Catterall, W. A., & Few, A. P. (2008). Calcium channel regulation and presynaptic plasticity. *Neuron*, *59*(6), 882–901. https://doi.org/10.1016/J.NEURON.2008.09.005

Concepts, C., Kwan, P., Schachter, S. C., & Brodie, M. J. (2011). *Drug-Resistant Epilepsy*. 919–926.

Di Maria, F., Lodola, F., Zucchetti, E., Benfenati, F., & Lanzani, G. (2018). The evolution of artificial light actuators in living systems: from planar to nanostructured interfaces. *Chemical Society Reviews*, *47*(13), 4757–4780. https://doi.org/10.1039/C7CS00860K

Dias, A. R., Minas Da Piedade, M. E., Martinho Simões, J. A., Simoni, J. A., Teixeira, C., Diogo, H. P., Meng-Yan, Y., & Pilcher, G. (1992). Enthalpies of formation of cis-azobenzene and trans-azobenzene. *The Journal of Chemical Thermodynamics*, *24*(4), 439–447. https://doi.org/10.1016/S0021-9614(05)80161-2

Diester, I., Kaufman, M. T., Mogri, M., Pashaie, R., Goo, W., Yizhar, O., Ramakrishnan, C., Deisseroth, K.,

& Shenoy, K. V. (2011). An optogenetic toolbox designed for primates. *Nature Neuroscience*, *14*(3), 387–397. https://doi.org/10.1038/NN.2749

DiFrancesco, M. L., Lodola, F., Colombo, E., Maragliano, L., Bramini, M., Paternò, G. M., Baldelli, P., Serra, M. D., Lunelli, L., Marchioretto, M., Grasselli, G., Cimò, S., Colella, L., Fazzi, D., Ortica, F., Vurro, V., Eleftheriou, C. G., Shmal, D., Maya-Vetencourt, J. F., … Benfenati, F. (2020). Neuronal firing modulation by a membrane-targeted photoswitch. *Nature Nanotechnology*, *15*(4), 296–306. https://doi.org/10.1038/s41565-019-0632-6

Ebihara, S., Shirato, K., Harata, N., & Akaike, N. (1995). Gramicidin-perforated patch recording: GABA response in mammalian neurones with intact intracellular chloride. *The Journal of Physiology*, *484*(1), 77–86. https://doi.org/10.1113/jphysiol.1995.sp020649

Emiliani, V., Entcheva, E., Hedrich, R., Hegemann, P., Konrad, K. R., Lüscher, C., Mahn, M., Pan, Z. H., Sims, R. R., Vierock, J., & Yizhar, O. (2022). Optogenetics for light control of biological systems. *Nature Reviews Methods Primers 2022 2:1*, *2*(1), 1–25. https://doi.org/10.1038/s43586-022-00136-4

Erlander, M. G., Tillakaratne, N. J. K., Feldblum, S., Patel, N., & Tobin, A. J. (1991). Two genes encode distinct glutamate decarboxylases. *Neuron*, *7*(1), 91–100. https://doi.org/10.1016/0896-6273(91)90077-D

Fenno, L., Yizhar, O., & Deisseroth, K. (2011). The Development and Application of Optogenetics. *Https://Doi.Org/10.1146/Annurev-Neuro-061010-113817*, *34*, 389–412. https://doi.org/10.1146/ANNUREV-NEURO-061010-113817

Feyen, P., Colombo, E., Endeman, D., Nova, M., Laudato, L., Martino, N., Antognazza, M. R., Lanzani, G., Benfenati, F., & Ghezzi, D. (2016). Light-evoked hyperpolarization and silencing of neurons by conjugated polymers. *Scientific Reports*, *6*. https://doi.org/10.1038/SREP22718

Francia, S., Shmal, D., Di Marco, S., Chiaravalli, G., Maya-Vetencourt, J. F., Mantero, G., Michetti, C., Cupini, S., Manfredi, G., DiFrancesco, M. L., Rocchi, A., Perotto, S., Attanasio, M., Sacco, R., Bisti, S., Mete, M., Pertile, G., Lanzani, G., Colombo, E., & Benfenati, F. (2022). Light-induced charge generation in polymeric nanoparticles restores vision in advanced-stage retinitis pigmentosa rats. *Nature Communications*, *13*(1). https://doi.org/10.1038/S41467-022-31368-3

Fuchter, M. J. (2020). On the Promise of Photopharmacology Using Photoswitches: A Medicinal Chemist's Perspective. *Journal of Medicinal Chemistry*, *63*(20), 11436–11447. https://doi.org/10.1021/acs.jmedchem.0c00629

Fujiwara, H., & Yonezawa, Y. (1991). Photoelectric response of a black lipid membrane containing an amphiphilic azobenzene derivative. *Nature 1991 351:6329*, *351*(6329), 724–726. https://doi.org/10.1038/351724a0

Gadsby, D. C. (2009). Ion channels versus ion pumps: the principal difference, in principle. *Nature Reviews. Molecular Cell Biology*, *10*(5), 344–352. https://doi.org/10.1038/NRM2668

Ghezzi, D., Antognazza, M. R., Dal Maschio, M., Lanzarini, E., Benfenati, F., & Lanzani, G. (2011). A hybrid bioorganic interface for neuronal photoactivation. *Nature Communications*, *2*(1).

https://doi.org/10.1038/NCOMMS1164

Gorostiza, P., & Isacoff, E. (2007). Optical switches and triggers for the manipulation of ion channels and pores. *Molecular BioSystems*, *3*(10), 686–704. https://doi.org/10.1039/B710287A

Hartley, G. S. (1937). The Cis-form of Azobenzene. *Nature 1937 140:3537*, *140*(3537), 281–281. https://doi.org/10.1038/140281a0

Hering, H., Lin, C. C., & Sheng, M. (2003). Lipid Rafts in the Maintenance of Synapses, Dendritic Spines, and Surface AMPA Receptor Stability. *The Journal of Neuroscience*, *23*(8), 3262. https://doi.org/10.1523/JNEUROSCI.23-08-03262.2003

Hinks, J., Wang, Y., Han Poh, W., Donose, B. C., Thomas, A. W., Wuertz, S., Chye Joachim Loo, S., Bazan, G. C., Kjelleberg, S., Mu, Y., & Seviour, T. (2014). *Modeling Cell Membrane Perturbation by Molecules Designed for Transmembrane Electron Transfer*. https://doi.org/10.1021/la403409t

Höglsperger, F., Vos, B. E., Hofemeier, A. D., Seyfried, M. D., Stövesand, B., Alavizargar, A., Topp, L., Heuer, A., Betz, T., & Ravoo, B. J. (2023). Rapid and reversible optical switching of cell membrane area by an amphiphilic azobenzene. *Nature Communications*, *14*(1). https://doi.org/10.1038/S41467-023-39032-0

Kiora pharmaceuticals. (2023). *Kiora - AAO Late-Breaking: Kiora's Small Molecule Photoswitch Demonstrates Meaningful Vision Improvements in Blind Patients with Retinitis Pigmentosa*. https://kiorapharma.reportablenews.com/pr/kiora-presents-abacus-data-at-aao

Korade, Z., & Kenworthy, A. K. (2008). Lipid rafts, cholesterol, and the brain. *Neuropharmacology*, *55*(8), 1265–1273. https://doi.org/10.1016/J.NEUROPHARM.2008.02.019

Kramer, R. H., Mourot, A., & Adesnik, H. (2013). Optogenetic pharmacology for control of native neuronal signaling proteins. *Nature Neuroscience 2013 16:7*, *16*(7), 816–823. https://doi.org/10.1038/nn.3424

Lanzani, G. (2012). *The photophysics behind photovoltaics and photonics*. https://www.wiley.com/en-us/The+Photophysics+behind+Photovoltaics+and+Photonics-p-9783527645145

Lingwood, D., & Simons, K. (2010). Lipid rafts as a membrane-organizing principle. *Science (New York, N.Y.)*, *327*(5961), 46–50. https://doi.org/10.1126/SCIENCE.1174621

Marchesi, A., Gao, X., Adaixo, R., Rheinberger, J., Stahlberg, H., Nimigean, C., & Scheuring, S. (2018). An iris diaphragm mechanism to gate a cyclic nucleotide-gated ion channel. *Nature Communications*, *9*(1). https://doi.org/10.1038/S41467-018-06414-8

Marchesi, A., Umeda, K., Komekawa, T., Matsubara, T., Flechsig, H., Ando, T., Watanabe, S., Kodera, N., & Franz, C. M. (2021). An ultra-wide scanner for large-area high-speed atomic force microscopy with megapixel resolution. *Scientific Reports*, *11*(1). https://doi.org/10.1038/S41598-021-92365-Y

Martino, N., Feyen, P., Porro, M., Bossio, C., Zucchetti, E., Ghezzi, D., Benfenati, F., Lanzani, G., & Antognazza, M. R. (2015). Photothermal cellular stimulation in functional bio-polymer interfaces. *Scientific Reports*, *5*. https://doi.org/10.1038/SREP08911

Marturano, V., Ambrogi, V., Bandeira, N. A. G., Tylkowski, B., Giamberini, M., & Cerruti, P. (2019). Modeling of azobenzene-based compounds. *Physical Sciences Reviews*, *2*(11). https://doi.org/10.1515/PSR-2017-0138/ASSET/GRAPHIC/J_PSR-2017-0138_FIGURE7.JPG

Maya-Vetencourt, J. F., Ghezzi, D., Antognazza, M. R., Colombo, E., Mete, M., Feyen, P., Desii, A., Buschiazzo, A., Di Paolo, M., Di Marco, S., Ticconi, F., Emionite, L., Shmal, D., Marini, C., Donelli, I., Freddi, G., MacCarone, R., Bisti, S., Sambuceti, G., … Benfenati, F. (2017). A fully organic retinal prosthesis restores vision in a rat model of degenerative blindness. *Nature Materials*, *16*(6), 681–689. https://doi.org/10.1038/nmat4874

Maya-Vetencourt, J. F., Manfredi, G., Mete, M., Colombo, E., Bramini, M., Di Marco, S., Shmal, D., Mantero, G., Dipalo, M., Rocchi, A., DiFrancesco, M. L., Papaleo, E. D., Russo, A., Barsotti, J., Eleftheriou, C., Di Maria, F., Cossu, V., Piazza, F., Emionite, L., … Benfenati, F. (2020). Subretinally injected semiconducting polymer nanoparticles rescue vision in a rat model of retinal dystrophy. *Nature Nanotechnology 2020 15:8*, *15*(8), 698–708. https://doi.org/10.1038/s41565-020-0696-3

Mingeot-Leclercq, M. P., Deleu, M., Brasseur, R., & Dufrêne, Y. F. (2008). Atomic force microscopy of supported lipid bilayers. *Nature Protocols*, *3*(10), 1654–1659. https://doi.org/10.1038/NPROT.2008.149

Moschetta, M., Vurro, V., Sesti, V., Bertarelli, C., Paternò, G. M., & Lanzani, G. (2023). Modulation of Mechanosensitive Potassium Channels by a Membrane-targeted Nongenetic Photoswitch. *The Journal of Physical Chemistry. B*, *127*(41), 8869–8878. https://doi.org/10.1021/ACS.JPCB.3C04551

Mourot, A., Herold, C., Kienzler, M. A., & Kramer, R. H. (2018). Understanding and improving photo-control of ion channels in nociceptors with azobenzene photo-switches. *British Journal of Pharmacology*, *175*(12), 2296–2311. https://doi.org/10.1111/bph.13923

Mourot, A., Tochitsky, I., & Kramer, R. H. (2013). *Light at the end of the channel : optical manipulation of intrinsic neuronal excitability with chemical photoswitches*. *6*(March), 1–15. https://doi.org/10.3389/fnmol.2013.00005

N., A. N. & H. (1994). *Nystatin perforated patch recording and its applications to analyses of intracellular mechanisms.* Jpn. J. Physiol. https://doi.org/10.2170/jjphysiol.44.433

Nanou, E., & Catterall, W. A. (n.d.). *Review Calcium Channels, Synaptic Plasticity, and Neuropsychiatric Disease*. https://doi.org/10.1016/j.neuron.2018.03.017

Nicolson, G. L. (2014). The Fluid-Mosaic Model of Membrane Structure: still relevant to understanding the structure, function and dynamics of biological membranes after more than 40 years. *Biochimica et Biophysica Acta*, *1838*(6), 1451–1466. https://doi.org/10.1016/J.BBAMEM.2013.10.019

Nozik, A. J. (2001). Spectroscopy and hot electron relaxation dynamics in semiconductor quantum wells and quantum dots. *Annual Review of Physical Chemistry*, *52*, 193–231. https://doi.org/10.1146/ANNUREV.PHYSCHEM.52.1.193

Palanker, D., Le Mer, Y., Mohand-Said, S., Muqit, M., & Sahel, J. A. (2020). Photovoltaic Restoration of Central Vision in Atrophic Age-Related Macular Degeneration. *Ophthalmology*, *127*(8), 1097.

https://doi.org/10.1016/J.OPHTHA.2020.02.024

Puppulin, L., Kanayama, D., Terasaka, N., Sakai, K., Kodera, N., Umeda, K., Sumino, A., Marchesi, A., Weilin, W., Tanaka, H., Fukuma, T., Suga, H., Matsumoto, K., & Shibata, M. (2021). Macrocyclic Peptide-Conjugated Tip for Fast and Selective Molecular Recognition Imaging by High-Speed Atomic Force Microscopy. *ACS Applied Materials & Interfaces*, *13*(46), 54817–54829. https://doi.org/10.1021/ACSAMI.1C17708

Rae, J., Cooper, K., Gates, P., & Watsky, M. (1991). Low access resistance perforated patch recordings using amphotericin B. *Journal of Neuroscience Methods*, *37*(1), 15–26. https://doi.org/10.1016/0165-0270(91)90017-T

Rand, D., Jakešová, M., Lubin, G., Vėbraitė, I., David-Pur, M., Đerek, V., Cramer, T., Sariciftci, N. S., Hanein, Y., & Głowacki, E. D. (2018). Direct Electrical Neurostimulation with Organic Pigment Photocapacitors. *Advanced Materials (Deerfield Beach, Fla.)*, *30*(25). https://doi.org/10.1002/ADMA.201707292

Rau, H. (1973). Spectroscopic Properties of Organic Azo Compounds. *Angewandte Chemie International Edition in English*, *12*(3), 224–235. https://doi.org/10.1002/ANIE.197302241

Rosenmund, C., Clements, J. D., & Westbrook, G. L. (1993). Nonuniform Probability of Glutamate Release at a Hippocampal Synapse. *Science*, *262*(5134), 754–757. https://doi.org/10.1126/SCIENCE.7901909

Russew, M. M., & Hecht, S. (2010). Photoswitches: From Molecules to Materials. *Advanced Materials*, *22*(31), 3348–3360. https://doi.org/10.1002/ADMA.200904102

Sahel, J. A., Boulanger-Scemama, E., Pagot, C., Arleo, A., Galluppi, F., Martel, J. N., Esposti, S. D., Delaux, A., de Saint Aubert, J. B., de Montleau, C., Gutman, E., Audo, I., Duebel, J., Picaud, S., Dalkara, D., Blouin, L., Taiel, M., & Roska, B. (2021). Partial recovery of visual function in a blind patient after optogenetic therapy. *Nature Medicine 2021 27:7*, *27*(7), 1223–1229. https://doi.org/10.1038/s41591-021-01351-4

Schmidt, H., Brachtendorf, S., Arendt, O., Hallermann, S., Ishiyama, S., Bornschein, G., Gall, D., Schiffmann, S. N., Heckmann, M., & Eilers, J. (2013). Nanodomain coupling at an excitatory cortical synapse. *Current Biology : CB*, *23*(3), 244–249. https://doi.org/10.1016/J.CUB.2012.12.007

Schneggenburger, R., Meyer, A. C., & Neher, E. (1999). Released Fraction and Total Size of a Pool of Immediately Available Transmitter Quanta at a Calyx Synapse. *Neuron*, *23*(2), 399–409. https://doi.org/10.1016/S0896-6273(00)80789-8

Sebastião, A. M., Colino-Oliveira, M., Assaife-Lopes, N., Dias, R. B., & Ribeiro, J. A. (2013). Lipid rafts, synaptic transmission and plasticity: impact in age-related neurodegenerative diseases. *Neuropharmacology*, *64*, 97–107. https://doi.org/10.1016/J.NEUROPHARM.2012.06.053

Sheng, J., He, L., Zheng, H., Xue, L., Luo, F., Shin, W., Sun, T., Kuner, T., Yue, D. T., & Wu, L. G. (2012). Calcium-channel number critically influences synaptic strength and plasticity at the active zone. *Nature Neuroscience*, *15*(7), 998–1006. https://doi.org/10.1038/NN.3129

Stingl, K., Schippert, R., Bartz-Schmidt, K. U., Besch, D., Cottriall, C. L., Edwards, T. L., Gekeler, F., Greppmaier, U., Kiel, K., Koitschev, A., Kühlewein, L., MacLaren, R. E., Ramsden, J. D., Roider, J., Rothermel, A., Sachs, H., Schröder, G. S., Tode, J., Troelenberg, N., & Zrenner, E. (2017). Interim Results of a Multicenter Trial with the New Electronic Subretinal Implant Alpha AMS in 15 Patients Blind from Inherited Retinal Degenerations. *Frontiers in Neuroscience*, *11*(AUG), 445. https://doi.org/10.3389/FNINS.2017.00445

Takahashi, T., & Momiyama, A. (1993). Different types of calcium channels mediate central synaptic transmission. *Nature*, *366*(6451), 156–158. https://doi.org/10.1038/366156A0

Tamamaki, N., Yanagawa, Y., Tomioka, R., Miyazaki, J. I., Obata, K., & Kaneko, T. (2003). Green Fluorescent Protein Expression and Colocalization with Calretinin, Parvalbumin, and Somatostatin in the GAD67-GFP Knock-In Mouse. *Journal of Comparative Neurology*, *467*(1), 60–79. https://doi.org/10.1002/CNE.10905

Tochitsky, I., Kienzler, M. A., Isacoff, E., & Kramer, R. H. (2018). Restoring Vision to the Blind with Chemical Photoswitches. *Chemical Reviews*, *118*(21), 10748–10773. https://doi.org/10.1021/acs.chemrev.7b00723

Tochitsky, I., Trautman, J., Gallerani, N., Malis, J. G., & Kramer, R. H. (2017). Restoring visual function to the blind retina with a potent, safe and long-lasting photoswitch. *Scientific Reports*, *7*, 1–8. https://doi.org/10.1038/srep45487

Uchida, K. (2004). Photochromism. Molecules and Systems. Edited by Heinz Dürr and Henri Bouas-Laurent. *Angewandte Chemie International Edition*, *43*(26), 3362–3362. https://doi.org/10.1002/ANIE.200385129

Valente, P., Orlando, M., Raimondi, A., Benfenati, F., & Baldelli, P. (2015). *Fine Tuning of Synaptic Plasticity and Filtering by GABA Released from Hippocampal Autaptic Granule Cells*. https://doi.org/10.1093/cercor/bhu301

Vyleta, N. P., & Jonas, P. (2014). Loose coupling between Ca2+ channels and release sensors at a plastic hippocampal synapse. *Science (New York, N.Y.)*, *343*(6171), 665–670. https://doi.org/10.1126/SCIENCE.1244811

Wadel, K., Neher, E., & Sakaba, T. (2007). The coupling between synaptic vesicles and Ca2+ channels determines fast neurotransmitter release. *Neuron*, *53*(4), 563–575. https://doi.org/10.1016/J.NEURON.2007.01.021

Wang, G., & Galli, T. (2018). Reciprocal link between cell biomechanics and exocytosis. *Traffic (Copenhagen, Denmark)*, *19*(10), 741–749. https://doi.org/10.1111/TRA.12584

Wheeler, D. B., Randall, A., & Tsien, R. W. (1994). Roles of N-type and Q-type Ca2+ channels in supporting hippocampal synaptic transmission. *Science (New York, N.Y.)*, *264*(5155), 107–111. https://doi.org/10.1126/SCIENCE.7832825

Wirsching, H. G., Galanis, E., & Weller, M. (2016). Glioblastoma. *Handbook of Clinical Neurology*, *134*, 381–397. https://doi.org/10.1016/B978-0-12-802997-8.00023-2

Yang, X., McGlynn, E., Das, R., Paşca, S. P., Cui, B., & Heidari, H. (2021). Nanotechnology Enables Novel Modalities for Neuromodulation. *Advanced Materials (Deerfield Beach, Fla.)*, *33*(52). https://doi.org/10.1002/ADMA.202103208

Yonezawa, Y., Fujiwara, H., & Sato, T. (1992). Photoelectric response of black lipid membranes incorporating an amphiphilic azobenzene derivative. *Thin Solid Films*, *210–211*(PART 2), 736–738. https://doi.org/10.1016/0040-6090(92)90389-S

Zuttion, F., Redondo-Morata, L., Marchesi, A., & Casuso, I. (2018). High-Resolution and High-Speed Atomic Force Microscope Imaging. *Methods in Molecular Biology (Clifton, N.J.)*, *1814*, 181–200. https://doi.org/10.1007/978-1-4939-8591-3_11

7 Acknowledgements

I express my sincere appreciation to Fabio Benfenati for his valuable expertise and guidance during this research. His mentorship was instrumental in shaping the trajectory of this work. Special thanks are due to Mattia L Difrancesco, Pietro Baldelli, and Elisabetta Colombo, whose guidance and tutoring played a pivotal role in refining this work. Constructive feedback and insightful suggestions from them greatly contributed to its improvement.

I am thankful to the members of my lab and collaborators, especially Luca Beverina, Chiara Bertarelli, and their teams for their direct contributions, synthesizing and providing the essential photoswitches. Special thanks are extended to Guglielmo Lanzani and his team for conducting the necessary biophysical studies on the compounds. Luca Maragliano and his team deserve special mention for their dedication to the molecular simulations and Arin Marchesi for the atomic force microscopy results presented in this thesis. I express gratitude to Francesca Vacca, Tiziana Ravasenga, Simona Francia, Filippo Galluzzi, Arta Mehilli, Silvia Casagrande, and all others who directly contributed to this work. The administrative team of our lab also deserves thanks for their assistance during my time in the lab.

Appreciation extends to fellow PhD students and post-docs for sharing in this adventure and maintaining morale. I gratefully acknowledge the entire EnTRAIN Vision consortium, whose financial support was provided by the Marie Skłodowska-Curie Actions of the European Union, under the Horizon 2020 program and the grant agreement No 861423, and made this research possible. I particularly thank Aurélie Pachkoff-Singh, the project manager, for facilitating workshops, conferences, and summer schools.

Outside the lab, crucial support came from friends, near and far, my partner, and my family. Their invaluable cheering and kindness emphasized the significance of such support for personal growth. Navigating the challenges of a male-dominated academic environment remains no small feat, and interactions outside academia served as a reminder that sacrificing holidays, maintaining constant accessibility, or tolerating mistreatment rooted in hierarchical positioning should not be prerequisites for success. Moreover, engaging in activities beyond the laboratory not only bolstered my spirits during tough times but also reminded me of life's broader dimensions.

Reflecting on this journey, I am reminded of the collective effort and shared experiences that have shaped my academic growth and achievements. I am deeply grateful for the consistent support and encouragement received from mentors, colleagues, and loved ones.